Transitional Boiling Phenomena in Single Drop Impact and Spray Cooling

Vom Fachbereich Maschinenbau
der Technischen Universität Darmstadt
zur
Erlangung des Grades eines Doktor-Ingenieurs (Dr.-Ing.)
genehmigte

Dissertation

vorgelegt von

Johannes Benedikt Schmidt, M.Sc.

aus Darmstadt

Berichterstatter:	Apl. Prof. Dr. I.V. Roisman
1. Mitberichterstatter:	Prof. Dr.-Ing. J. Hussong
2. Mitberichterstatter:	DR CNRS Dr. G. Castanet
Tag der Einreichung:	24.10.2023
Tag der mündlichen Prüfung:	13.12.2023

Darmstadt 2023

D 17

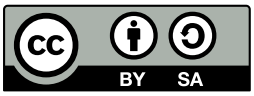

Erklärung

Hiermit erkläre ich, dass ich die vorliegende Arbeit, abgesehen von den in ihr ausdrücklich genannten Hilfen, selbständig verfasst habe.

Darmstadt, den 24.10.2023

J. Benedikt Schmidt

Abstract

Spray cooling is a technology that can be easily applied to the surfaces of various geometries and achieve high cooling rates under some conditions. It has numerous applications, such as medical laser treatments, metal quenching, cooling hot forging dies, and powerful electrical systems.

Predicting optimal spray cooling parameters is a challenging task. The cooling performance depends on interactions of various hydrodynamic and thermodynamic phenomena. Multiple factors influence this complex interplay, such as the size and velocity of the single drops, mass flux density, material properties, and substrate temperature. The best approach to model spray cooling is based on the results of single drop impacts on a hot substrate since this phenomenon is a fundamental part of spray wall interactions. This approach already resulted in reliable spray cooling models for nucleate and film boiling regimes. However, the transitional boiling regime is still not fully understood and lacks reliable models that account for the relevant physical phenomena.

The aim of this study is to expand the current knowledge of the *transitional boiling phenomena* that appears during spray cooling in the range of wall temperatures separating the nucleate boiling and film boiling regime in spray cooling. The main focus is the experimental and theoretical study of a single drop impact, drop interactions at the substrate, and, finally, the modeling of spray cooling. The experimental setup allows to observe the drop impacts and to measure the heat flux, characteristic times, and impact parameters of the impacting drops at various initial substrate temperatures.

The single drop impact is studied for the main outcome regimes associated with transitional boiling: drop dancing, wet drop rebound, and thermal atomization. The drop dancing regime is characterized by droplets hovering and "dancing" above the substrate after some characteristic time. The phenomenon is modeled on the assumption of percolating vapor bubbles in the liquid lamella, which, at some conditions, can form an infinite vapor cluster. The modeled percolation time is compared to the experimentally determined characteristic time with an excellent agreement. Further, the threshold temperature between the drop dancing regime and wet rebound regime is determined experimentally by the drop residence time. It is assumed that the percolation of vapor bubbles causes an impacting drop to rebound while wetting the surface. The threshold temperature is described by the instance when the percolation time is in the order of the natural drop oscillation time. This theoretically predicted threshold temperature, also called thermosuperrepellency temperature, agrees well with the experimentally determined threshold temperature between the drop dancing and wet rebound regime. Finally, the heat flux at the hot substrate is measured with a

high spatial and temporal resolution in the thermal atomization regime. The heat flux is modeled on the assumption of direct wetting and heat conduction at the liquid/solid interface. The experimental data and theoretical prediction are in the same order of magnitude.

When transferring single drop results to spray cooling, it is essential to understand also the interactions of impacting drops at the hot substrate. The interactions are investigated by the transient cooling of a hot substrate with an impacting drop train in the drop rebound regime. The impacting drops cause a temperature gradient in the substrate, which is measured during the experiments. The temperature decrease is modeled by the superposition of drop impacts and the heat removed by each impacting drop. The experimental and theoretical results agree well. Further, the theory is used to describe the formation of liquid patches during spray cooling. These patches appear by interacting drops at wall temperatures close to the thermosuperrepellency temperature.

The results from both the single drop impact and drop interactions are then combined to develop a model of spray cooling in the transitional boiling regime. The findings of vapor percolation in the drop dancing regime and drop interactions are used to model the heat flux. The theoretical predictions agree well with the experimental heat flux for sprays with low number flux, although no adjustable parameters are used in the modeling. Further, the so-called Leidenfrost temperature, associated with the minimum heat flux during transient spray cooling, is determined. It is shown that the Leidenfrost temperature for sprays correlates very well with the theoretically predicted thermosuperrepellency temperature. This result indicates that the minimum heat flux temperature is determined not by the onset of film boiling but by the appearance of thermosuperrepellency caused by the percolation of vapor channels at the liquid/substrate interface.

Kurzfassung

Sprühkühlung ist eine Technologie, die leicht auf verschiedenste Oberflächengeometrien angewendet werden kann und unter bestimmten Bedingungen hohe Kühlraten erzielt. Die Sprühkühlung hat zahlreiche Anwendungen, darunter medizinische Laserbehandlungen, das Abschrecken von Metallen, die Kühlung von Warmschmiedegesenken und leistungsstarken elektrischen Systemen.

Die Vorhersage optimaler Sprühkühlungsparameter ist eine anspruchsvolle Aufgabe. Die Kühlleistung hängt von den Wechselwirkungen verschiedener hydrodynamischer und thermodynamischer Phänomene ab. Mehrere Faktoren beeinflussen dieses komplexe Zusammenspiel, wie z. B. die Größe und Geschwindigkeit der einzelnen Tropfen, die Massenstromdichte, die Materialeigenschaften und die Substrattemperatur. Der beste Ansatz zur Modellierung der Sprühkühlung basiert auf den Ergebnissen des Auftreffens eines einzelnen Tropfens auf einem heißen Substrat, da dieses Phänomen ein grundlegender Bestandteil der Wechselwirkungen zwischen dem Spray und der Wand ist. Dieser Ansatz führte bereits zu zuverlässigen Modellen für den Blasensiedebereich und Filmsiedebereich bei der Sprühkühlung. Der Übergangssiedebereich ist jedoch noch nicht vollständig verstanden und es fehlen zuverlässige Modelle, die die wesentlichen physikalischen Phänomene berücksichtigen.

Das Ziel dieser Studie ist es, das derzeitige Wissen über die Phänomene des Übergangssiedens zu erweitern, die bei der Sprühkühlung im Temperaturbereich zwischen dem Blasensieden und Filmsieden auftreten. Der Schwerpunkt liegt dabei auf der experimentellen und theoretischen Untersuchung des Einzeltropfenaufpralls, der Wechselwirkungen zwischen den Tropfen auf dem Substrat und schließlich der Modellierung der Sprühkühlung. Der Versuchsaufbau ermöglicht, den Tropfenaufprall zu beobachten sowie die Messung der Wärmestromdichte, von charakteristischen Zeiten beim Tropfenaufprall und der Einzeltropfen Aufprallparameter bei verschiedenen initialen Substrattemperaturen.

Der Einzeltropfenaufprall wird für die wichtigsten Ergebnisbereiche untersucht, die mit dem Übergangssieden verbunden sind: „Drop Dancing“, „Wet Drop Rebound“ und „Thermal Atomization“. Das Regime Drop Dancing zeichnet sich dadurch aus, dass die Tropfen nach einer charakteristischen Zeit über dem Substrat schweben und „tanzen“. Dieses Phänomen wird unter der Annahme perkolierender Dampfblasen im Flüssigkeitsfilm modelliert, die unter bestimmten Bedingungen ein unendliches Dampfcluster bilden können. Die so modellierte Perkolationszeit wird mit der experimentell ermittelten charakteristischen Zeit verglichen. Beide Zeiten stimmen sehr gut überein. Weiterhin wird die Grenztemperatur zwischen dem Drop Dancing Bereich und Wet Drop Rebound Bereich experimentell anhand der Tropfenverweildauer bestimmt. Es wird

angenommen, dass die Perkolation von Dampfblasen dazu führt, dass ein auftreffender Tropfen abprallt, während er die Oberfläche benetzt. Die Grenztemperatur zwischen beiden Regimen wird basierend auf der Annahme modelliert, dass die Perkolationszeit in der Größenordnung der natürlichen Tropfenschwingungsdauer liegt. Diese theoretisch vorhergesagte Grenztemperatur, die auch als Thermosuperrepellency Temperatur genannt wird, stimmt gut mit der Grenztemperatur zwischen dem Drop Dancing Bereich und Wet Drop Rebound Bereich überein. Schließlich wird die Wärmestromdichte, die vom heißen Substrat abgeführt wird, mit hoher räumlicher und zeitlicher Auflösung im Thermal Atomization Bereich gemessen. Die Wärmestromdichte wird zweidimensional modelliert, unter der Annahme, dass die Oberfläche benetzt und von Wärmeleitung an der Flüssigkeit/Substrate Grenzfläche. Die experimentellen Daten und die theoretische Vorhersage liegen in der gleichen Größenordnung.

Bei der Übertragung von Ergebnissen des Einzeltropfens auf die Sprühkühlung ist es wichtig, auch die Wechselwirkungen der auftreffenden Tropfen auf dem heißen Substrat zu verstehen. Die Wechselwirkungen werden durch die instationäre Kühlung eines heißen Substrats mit einer Tropfenkette im Drop Rebound Bereich untersucht. Die aufprallenden Tropfen verursachen einen Temperaturgradienten im Substrat, der bei den Versuchen gemessen wird. Dieser Temperaturabfall wird modelliert, indem die aufkommenden Tropfen und die von jedem auftreffenden Tropfen abgeführten Wärme superpositioniert wird. Die experimentellen und theoretischen Ergebnisse stimmen gut überein. Weiterhin wird die entwickelte Theorie verwendet, um die Bildung von Flüssigkeitsansammlungen im Rahmen der Sprühkühlung zu beschreiben. Diese Ansammlungen entstehen durch interagierende Tropfen bei Wandtemperaturen nahe der Thermosuperrepellency Temperatur.

Die Ergebnisse des Einzeltropfenaufpralls und der Tropfenwechselwirkungen werden kombiniert, um ein Modell der Sprühkühlung im Übergangssiedegebiet zu entwickeln. Die Erkenntnisse über die Dampfblasenperkolation beim Drop Dancing und die Tropfenwechselwirkungen werden zur Modellierung der Wärmestromdichte verwendet. Die Ergebnisse der Modellierung stimmen gut mit der experimentellen Wärmestromdichte für Sprays mit niedriger Tropfendichte überein, obwohl bei der Modellierung keine empirischen Parameter verwendet werden. Ferner wird die sogenannte Leidenfrost-Temperatur bestimmt, die mit dem minimalen Wärmestrom während der instationären Sprühkühlung verbunden wird. Es wird gezeigt, dass die Leidenfrost-Temperatur für Sprays sehr gut mit der theoretisch vorhergesagten Thermosuperrepellency Temperatur korreliert. Dieses Ergebnis deutet darauf hin, dass die Temperatur der minimalen Wärmestromdichte nicht durch den Beginn des Filmsiedens bestimmt wird, sondern durch das Auftreten von Thermosuperrepellency, hervorgerufen durch die Perkolation von Dampfkanälen an der Flüssigkeit/Substrat Grenzfläche.

Acknowledgments

First of all, I would like to thank *Apl. Prof. Ilia V. Roisman*, for awakening my interest and enthusiasm for droplets and science. This work is only possible with his mathematical, analytical, and general support. I would also like to thank *Prof. i.R. Cameron Tropea* for his confidence in me to discover new findings about droplets and sprays. Further, I thank *Prof. Jeanette Hussong*, who not only accompanied my work with interest but also improved it with valuable hints and critical questions. I thank them for the opportunity and their support in writing this dissertation at the Institute for Fluid Dynamics and Aerodynamics (SLA) of the Technische Universität Darmstadt. Additionally, I would like to thank *DR CNRS G. Castanet* for reviewing this thesis.

Furthermore, I thank the Deutsche Forschungsgemeinschaft for financially enabling and supporting this thesis through the scientific exchange within the collaborative research cluster SFB-TRR 75.

I want to express special thanks to Corinna Neumann and Birgit Neuthe for the administrative support and, of course, to Ilona Kaufhold, Alex Beck, Tim Geelhaar, Joachim Heyl, Manolo Vaca-Schwinkendorf and Martin Weiß for the practical as well as private support.

Furthermore, I would like to thank Jan Breitenbach, who awakened my interest in starting a Ph.D. during my master's studies and has always been able to advise me in all situations. I would also like to thank him for his trust as a research assistant and for the excellent starting conditions. Further, I thank Fabian Tenzer for his collaboration. His excellent experimental data play an essential role in this thesis. I want to thank Andreas Bauer, Sebastian Brulin, and Johannes Feldmann, who, together with Jan Breitenbach and Fabian Tenzer, were role models for me as a rookie. Next, I would also like to thank Marija Gajevic Joksimovic for her support and emotion in challenging situations. I would also like to thank Ivan Joksimovic for his help through the jungle of numerics. I thank Niklas Apell for always being a safe source for all concerns. Philipp Brockmann and Maximilian Lausch were always joyful company and brought helpful input. I would like to thank Simon Burgis and Kilian Köbschall for accompanying the trip to zero-g and back. Further, I would like to thank "the icing guys", Louis Reitter and Mark Gloerfeld, for letting me enjoy "cool" droplets.

I would like to thank the proofreaders of my thesis, Niklas Appel, Jan Breitenbach, Philipp Brockmann, Maximilian Lausch, and Till Werner, for supporting my writing and their helpful suggestions.

Many students have supported my work over the past years. I want to thank the students Stephan Buczko, Christiane Helbrecht, Anton Sperling, Matthias Siegel, Till Werner, Julius Quell, Wilhelm Unkelbach, Jonko Paetzold, Lars Urban, and Rouven

Gerischer, who have supported me with their work and have kept my back free.

Big thanks to my family and friends. I am thankful to my parents, Renate and Rolf Georg Schmidt, who laid the foundation for this thesis with their education and values and for always supporting me. Further, I would like to thank my siblings Sebastian Schmidt and Petra Willand for their understanding when the little brother was not available again.

I would like to give special thanks to Lara, who always supported me and co-suffered with me. Thank you very much for your patience.

Thank you.

Benedikt

Contents

1 Introduction

The spray cooling technology and related research are motivated by different technical applications, as mentioned in Section 1.1. The most important research findings are summarized in Section 1.2. The section discusses isothermal and non-isothermal drop-wall interactions as a critical element of spray-wall interactions. Further, the most important findings regarding spray-wall interactions are presented. Finally, the objective and structure of this study are presented in Section 1.3.

Parts of this chapter, including text and some figures, are published in Schmidt et al. (2018, 2019, 2021a,b, 2022, 2023a,b).

1.1 Motivation

Spray cooling is a technique that is capable of achieving high cooling rates at solid surfaces, while it is rather simple to apply. This is why spray cooling is a promising cooling technology for a wide range of technical applications.

Spray cooling has several significant advantages compared to other cooling technologies and can be used for an extreme range of boundary conditions. Sprays can be applied to cool surfaces in a wide range of initial temperatures. They vary from very low temperatures during cryogenic cooling of human skin in medical laser treatments (Sehmbey et al., 1995; Nelson et al., 2000; Kao et al., 2004) up to very high temperatures of 1300 K Bolle & Moureau (1982) during quenching of metals (Deiters & Mudawar, 1989; Rodman et al., 2011; Ravikumar et al., 2023) and cooling of hot forging dies (Behrens et al., 2010; Pola et al., 2013). Spray cooling can achieve very high heat transfer coefficients compared to other heat removal technologies, as shown in Fig. 1.1.

The high cooling rate and ease of use make spray cooling essential to many applications. Spray cooling is used, for example, in daily life applications, such as firefighting. Water can be used more efficiently in comparison to jets, minimizing subsequent water damage (Grant et al., 2000). Spray cooling is also used in advanced applications, such as high-power lasers and electronic microchips (Sehmbey et al., 1995; Ji et al., 2023). The efficiency of solar panels is increased by the uniform and efficient cooling by sprays (Laseinde & Ramere, 2021; Yesildal et al., 2022), helping the green transformation to renewable energies. Spray cooling is also used in micro-gravity applications in aerospace engineering (Silk et al., 2008; Cheng et al., 2016; Wang et al., 2020a).

A typical setup for spray cooling is relatively simple compared to other high-power cooling technologies since sprays are easy to generate and apply on surfaces (Schiro et al., 2017). For example, sprays can be applied to flat surfaces in metal quenching or complex surface geometries, such as forging dies (Tenzer et al., 2019; Apostol et al.,

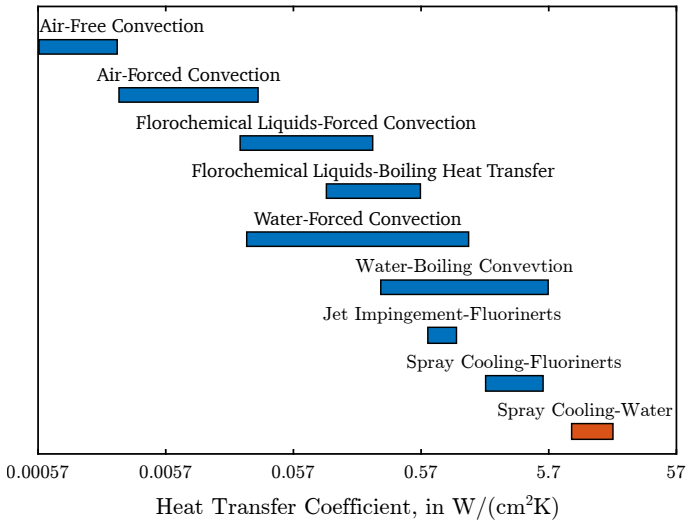

Figure 1.1: Heat transfer coefficient of multiple cooling technologies. Reprint (adapted) from Sienski et al. (1996), with permission from IEEE, ©1996 IEEE.

2022). Spray cooling is also suitable for achieving homogeneous cooling of a surface, which is particularly important in metallurgical applications (Rodman et al., 2011).

However, spray cooling is a technology that is complicated to use optimally. One challenging task is to define, measure, and control many influencing factors that determine the cooling performance of spray cooling. The fundamentals of spray cooling are the subject of many studies, which are introduced in the following section.

1.2 Fundamentals of Single Drop Impact and Spray Cooling

The cooling performance of spray cooling is determined by a large number of influencing factors. The material properties of the substrate, which has to be cooled, and the cooling liquid affect the heat transfer from the wall (Gajevic Joksimovic et al., 2023; Tenzer et al., 2019). The macroscopic and microscopic surface properties, as the surface morphology, influence the interaction of the impinging droplets with the wall (Sodtke & Stephan, 2007; Martínez-Galván et al., 2013). The wall and liquid temperature affect the boiling phenomena during the spray impact (Liang & Mudawar, 2017a). Moreover, the impact parameters of the individual drops influence their behavior on the surface (Breitenbach et al., 2018b).

Due to the large number of influencing parameters and the fact that sprays are usually polydisperse, the theoretical modeling and prediction of the heat flux in spray cooling is complex. Review papers reveal that most models are highly empirical, as

in Liang & Mudawar (2017a,b). A common approach to reducing the complexity of spray cooling is to break down spray-wall interactions into single drop-wall interactions as an essential element of spray cooling (Yarin et al., 2017). Studying single drop impacts on hot substrates allows for describing the fundamental phenomena in more detail. A single drop impact on a hot substrate is determined by hydrodynamics and thermodynamics effects. The hydrodynamic phenomena during the single drop impact can be described for an isothermal drop impact onto a dry substrate, as shown in Section 1.2.1. Heating the substrate above the liquid saturation temperature may lead to the appearance of thermodynamic effects such as boiling and Maranghoni flows to the drop impact dynamics. The interaction of thermodynamics and hydrodynamics results in different drop impact regimes, for example, *Drop Deposition* without boiling and accompanied by boiling, *Drop Dancing*, *Thermal Atomization*, and *Drop Rebound*. Physical models are found for some of these regimes, while others are described only as phenomenological, as shown in Section 1.2.2.

The findings of single drop impacts can be transferred to spray cooling by taking interaction effects during the impact of multiple drops into account (Moreira et al., 2010; Breitenbach et al., 2018b; Benther et al., 2021). The different boundary conditions and interactions between the occurring hydro- and thermodynamics of the single drops result in different spray cooling regimes, such as *Single-Phase Cooling*, *Nucleate Boiling*, *Transitional Boiling*, and *Film Boiling*. Fortunately, in recent years, physical models are developed to predict the heat flux in nucleate boiling by Tenzer et al. (2019) and film boiling by Breitenbach et al. (2017b). Nevertheless, the transitional boiling regime has yet to be discovered (Liang & Mudawar, 2017a), as shown in Section 1.2.3.

1.2.1 Isothermal Drop Impact

Various drop outcome regimes can be observed during an isothermal drop impact onto a solid dry surface. The dynamics and outcome of the drop impact depend on the impact parameters, liquid properties, surface properties, and ambient conditions. Comprehensive review articles on the dynamics and outcome of the isothermal drop impact can be found in Rioboo et al. (2001), Yarin (2006), Marengo et al. (2011), Roisman et al. (2015), Josserand & Thoroddsen (2016), Yarin et al. (2017), and Cheng et al. (2022). The dynamics of the drop impact and boundaries between outcome regimes are often quantified by the Reynolds number Re or Weber number We (Rioboo et al., 2001)

$$\mathrm{Re} = \frac{u_0\, d_0}{\nu}, \quad \mathrm{We} = \frac{\rho_l\, d_0\, u_0^2}{\sigma_l}, \tag{1.1}$$

with the drop diameter d_0, impact velocity u_0, kinematic viscosity ν_l, liquid density ρ_l, and surface tension σ_l. The drop impact dynamics and regime are sometimes also quantified by combinations of the Weber and Reynolds number, for example, the Ohnesorge number $\mathrm{Oh} = \mathrm{We}/\mathrm{Re}$ and capillary number $\mathrm{Ca} = \sqrt{\mathrm{We}}/\mathrm{Re}$ (Rein, 2002).

Drop Impact Dynamics

A drop impact onto a solid substrate first leads to the deformation of the drop. Depending on the impact parameters, the inertia or surface tension forces determine the drop spreading and receding. In the case of an inertia-dominated drop impact, the impact may lead under some impact parameters to the disintegration of the drop. Different regimes are introduced in the following.

Drop impacts with $\mathrm{We} \gg 10$ and $\mathrm{Re} \gg 10^2$ are inertia dominated (Roisman et al., 2009). The impact leads to a strong drop deformation after it touches a dry solid substrate. The inertia forces lead the liquid to flow radially outwards, forming a thin liquid lamella. The capillary forces lead the liquid to form a thick rim at the boundary of the lamella (Taylor, 1959; Roisman et al., 2009). The lamella and the rim form a typical pizza-like shape of the spreading drop.

The flow field in the spreading drop is given by Yarin & Weiss (1995) for the inertia-dominated, inviscid case. The flow field is provided as a remote asymptotic solution for times much larger than the time for flow initiation. The solution satisfies the mass and momentum balance equations.

Immediately after impact, a viscous boundary layer develops within the spreading lamella, beginning from the liquid-solid interface. A similarity solution of the viscous flow is given by Roisman (2009). The viscous boundary layer thickness grows with $\delta_\nu(t) \sim \sqrt{\nu t}$. The flow is strongly damped as soon as the liquid boundary layer reaches the free surface of the lamella. The expression for the residual lamella thickness is obtained by Roisman (2009) in the form

$$h_{\mathrm{res}} \approx 0.79\, d_0\, \mathrm{Re}^{-2/5}, \tag{1.2}$$

based on the remote asymptotic solution. The time $t = 0$ until the viscous boundary reaches the top of the liquid lamella $t = t_\nu$ is estimated in Roisman (2009) as

$$t_\nu = \frac{d_0\, \mathrm{Re}^{1/5}}{u_0}. \tag{1.3}$$

The lamella reaches its maximum spreading diameter d_{max} as soon as the liquid flow is damped in the lamella. The maximum spreading diameter can be obtained by a semiempirical relation from Roisman (2009) in the form

$$d_{\mathrm{max}} \approx 0.87\, \mathrm{Re}^{1/5} - 0.4\, \mathrm{Re}^{2/5}\, \mathrm{We}^{-1/2}. \tag{1.4}$$

After the maximum spreading diameter is reached, the lamella starts to retract, and the spreading diameter settles at a certain drop diameter depending on the wettability of the substrate (Roisman et al., 2002).

Drop impacts onto a dry substrate with high inertia forces result in splashing. The threshold for splashing is often characterized by the K-number

$$\mathrm{K} = \mathrm{Re}^{2/5}\mathrm{We}^{4/5}. \tag{1.5}$$

If the K-number is higher than a specific threshold value K_s, the drop leads to splash. The value of K_s depends on the relative film thickness on the wall. The exponents of equation (1.5) vary between different publications. Slightly different exponents are derived for the single drop onto a dry substrate (Stow & Hadfield, 1981). The exponents, given in equation 1.5, are derived for a single drop impact onto a thin liquid film by Cossali et al. (1997). Additionally, they are validated for the spray impact onto a thin liquid film in Mundo et al. (1997) and Mundo et al. (1998). In the case of drop impact onto a dry substrate the splashing threshold is not determined by the K-number. It is influenced by the surface morphology and even ambient pressure (Yarin et al., 2017).

A droplet splash results in liquid deposition on the substrate and secondary droplets. In a spray impact, liquid deposition produces a thin liquid film on the surface. The total amount of liquid is split into the mass rejected as secondary spray and the mass deposited at the surface. In Breitenbach et al. (2018b), it is shown that the rejected mass flux $\dot{m}_a$ is a function of the K-number in the form

$$\dot{m}_a/\dot{m}_b = 0.5 - 0.616\exp\left(-\mathrm{K}/750.9\right), \tag{1.6}$$

where $\dot{m}_b$ is the impacting mass flux.

At lower impact velocities, the capillary forces may dominate the liquid flow of a single drop impact. The threshold for the capillary dominated impact is $P = \mathrm{We}\,\mathrm{Re}^{-4/5} < 1$ (Clanet et al., 2004; Roisman, 2009; Marengo et al., 2011). In this case, the spreading lamella reaches its maximum diameter before the viscous boundary layer reaches the free surface. The flow in the lamella is not damped, and the viscous forces do not determine the maximum spreading diameter. Multiple correlations based on the Weber number can be found for the maximum spreading diameter. The best agreement with experimental data shows the scale from Clanet et al. (2004)

$$d_{\max} = d_0\,\mathrm{We}^{1/4}, \tag{1.7}$$

as reported in Marengo et al. (2011).

A drop impact on a superhydrophobic substrate leads to a drop rebound in the capillary forces dominated regime. The drop spreads, recedes, and finally rebounds from the substrate. The contact time of the drop at the substrate is consistent with the natural oscillation time of drops t_σ (Wachters & Westerling, 1966; Richard et al., 2002) obtained from Rayleigh (1879)

$$t_\sigma \sim \sqrt{\frac{\rho_l d_0^3}{\sigma}}. \tag{1.8}$$

1.2.2 Drop Impact onto Hot Substrates

The drop impact onto a hot substrate is determined by hydrodynamic and thermodynamic effects. Different drop outcome regimes can be observed for the drop impact onto a hot substrate compared to an isothermal drop impact (Breitenbach et al., 2018b).

An early but comprehensive description of the regimes is given by Worthington (1877) and Worthington & Cole (1897).

A drop impact at a surface with an initial wall temperature $T_{w,0}$ below the saturation temperature T_{sat} leads to drop deposition with single phase cooling (Breitenbach et al., 2018b). At temperatures above saturation temperature, the drop deposition is accompanied by nucleate boiling with small bubbles in the liquid film (Breitenbach et al., 2017a). With a further increasing surface temperature, the liquid of the drop starts to rebound from the substrate partially. The observation of the drop impact is reminiscent of a dancing drop. Hence, the regime is called drop dancing (Roisman et al., 2018). The bubbles at the substrate start to merge, which is why the regime can be labeled as a transitional boiling regime. Drop impact at high surface temperatures results in thermal atomization of the drop or a drop rebound. Thermal atomization occurs at high impact velocities when viscous forces dominate the lamella flow. A strong nucleate boiling characterizes the beginning of the lamella spreading. Beginning from the rim, a vapor layer separates the lamella from the substrate. The regime is determined by nucleate boiling and film boiling. Therefore, the regime belongs to the transitional boiling regime (Roisman et al., 2018). At lower impact velocities, the drop rebounds. Capillary forces determine the liquid flow, so the drop impact results in a drop rebound (Castanet et al., 2015). The drop rebound regime can be accompanied by surface wetting or without surface wetting (Lee et al., 2020).

The outcome regimes are shown in Figure 1.2. Representative observations of each regime are shown on the left side of the figure. Schematics of the outcome in the middle line of the figure illustrate the macroscopic processes. The schematics on the right represent the microscopic processes and boiling regimes at the solid-liquid interface.

The dependence of the regimes on the surface temperature and impact parameters is shown in Fig. 1.3. In the map are shown the dependencies for the impact of water drops on polished aluminum. Comprehensive reviews of the single drop impacts on hot substrates can be found in Moreira et al. (2010); Mudawar (2013); Breitenbach et al. (2018b). The following sections describe the fundamentals of these regimes based on these reviews and further literature.

Drop Deposition Without Nucleate Boiling

A drop impact onto a hot surface results in a drop deposition without nucleate boiling, as long as the surface temperature $T_{w,0}$ is below the liquid boiling temperature (Pasandideh-Fard et al., 2001). As soon as the substrate is wetted, heat transfers from the substrate to the drop. The heat transfer inside the substrate is determined by heat conduction, while the heat transfer inside the liquid is dominated by convection. The impact of a single drop and the simultaneous impact of two drops onto a hot substrate in the drop deposition without nucleate boiling is studied in Roisman (2010) and Batzdorf et al. (2017). The theoretical models from these studies for the temperature distribution in the wall and heat flux at the liquid-solid interface are based on the analysis of a thermal boundary layer in the solid substrate.

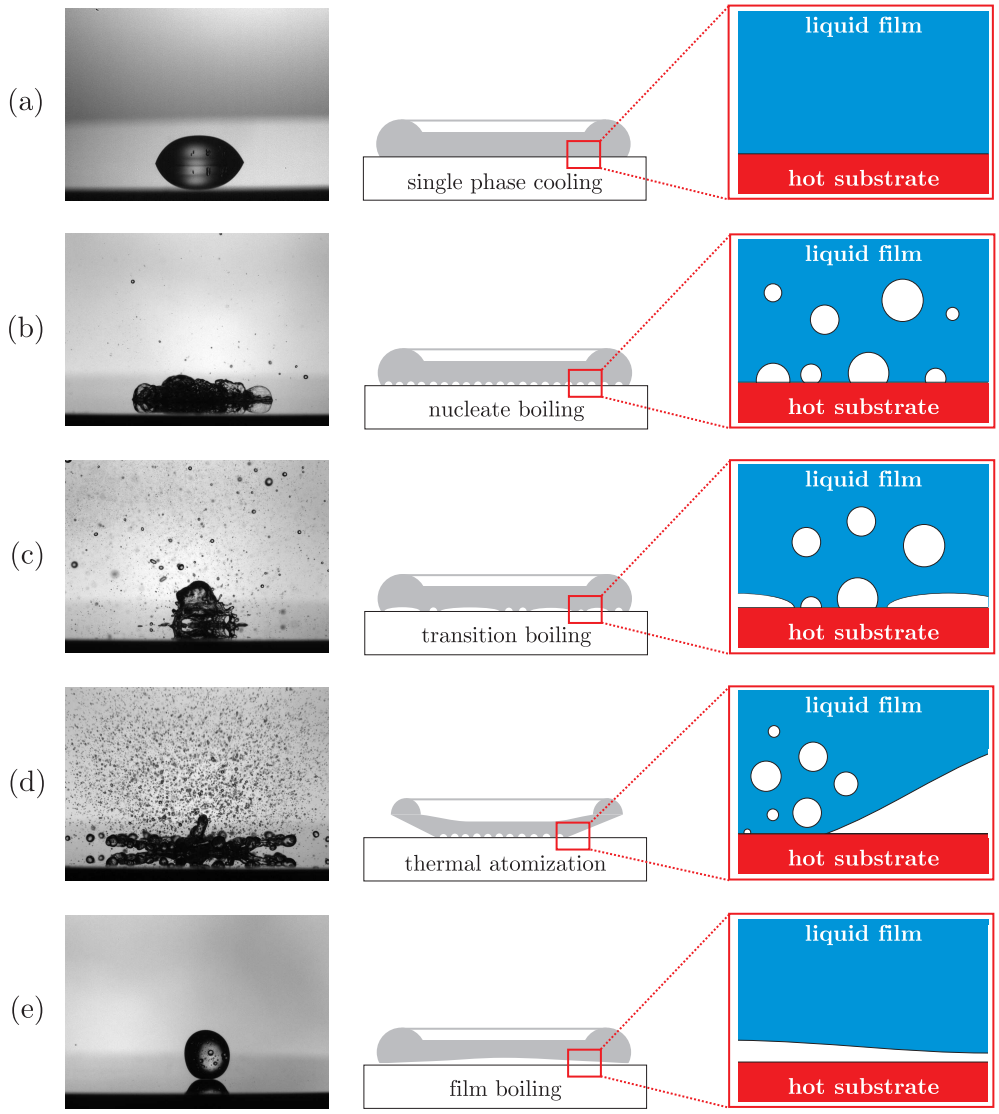

Figure 1.2: Images, schematic and microscopic thermodynamic boiling phenomena of the drop impact regimes: (a) drop deposition with single phase cooling, (b) drop deposition with nucleate boiling, (c) drop dancing, (d) thermal atomization, (e) drop rebound. Reprint from Breitenbach (2018), licensed under CC BY-NC-ND 4.0., ©2019 Jan Breitenbach.

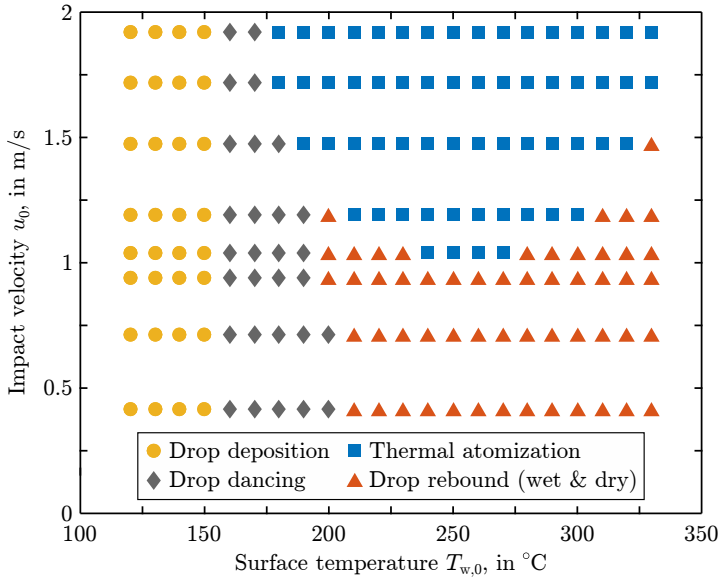

Figure 1.3: Regime map of the outcome of single drop impacts onto a hot polished aluminum surface. The drop diameter is $d_0 = 2.2\,\mathrm{mm}$. Reprint (adapted) from Breitenbach et al. (2018b), with permission from Springer Nature, © 2018 Springer-Verlag GmbH Germany, part of Springer Nature.

The thermal boundary layer develops inside the substrate as soon as the substrate is wetted. The heat conduction inside the substrate is described by the equation of heat

$$\frac{\partial T_\mathrm{w}}{\partial t} - \alpha_\mathrm{w} \Delta T_\mathrm{w} = 0, \tag{1.9}$$

with α_w being the thermal diffusivity of the wall. The thickness $\delta_{\mathrm{t,w}}$ of the layer grows with the time $\delta_{\mathrm{t,w}}(t) \sim \sqrt{\alpha_\mathrm{w} t}$. The characteristic thermal boundary layer thickness of a drop impact $\delta_{\mathrm{t,w}} \sim \sqrt{\alpha_\mathrm{w} d_0 / u_0}$ is smaller compared to the wetted area, which is in the order of the drop diameter d_0. For this reason, a one-dimensional solution of equation (1.9) can be applied to the heat transfer associated with the drop impact (Batzdorf et al., 2017). A self-similar solution of the temperature distribution inside the substrate is given by Roisman (2010) for the case when the problem is not influenced by phase change

$$T_\mathrm{w}(t,z) = T_{\mathrm{w},0} + \frac{e_\mathrm{l}(T_{\mathrm{l},0} - T_{\mathrm{w},0})}{e_\mathrm{l} + e_\mathrm{w} \mathscr{I}(\mathrm{Pr_l})} \operatorname{erfc}\left[\frac{z}{2\sqrt{\alpha_\mathrm{w}(t - t_0)}}\right], \tag{1.10}$$

with the distance z orthogonal to the surface, the initial liquid temperature $T_{\mathrm{l},0}$, the thermal effusivities e of the wall and liquid, the time instance t_0 when the substrate surface is wetted and the dimensionless function $\mathscr{I}(\mathrm{Pr})$ of the liquid Prandtl number $\mathrm{Pr_l}$. The thermal effusivity $e = \sqrt{\lambda \rho c_\mathrm{p}}$ describes the material's ability to exchange heat

with its surroundings, with λ being the thermal conductivity and c_p being the heat capacity. The Prandtl number $\mathrm{Pr} = \nu/\alpha$ describes the diffusivity ratio by convection versus conduction within a fluid. The function $\mathscr{I}(\mathrm{Pr})$, shown in Fig. 1.4, is described in Roisman (2010). In the case of very high Prandtl numbers, the function approaches one. In this case, the influence of the flow is neglectable, and the heat flux is equal to the heat conduction between two infinite solid bodies. For very low Prandtl numbers $\mathrm{Pr} \ll 1$, the numerical solution approaches an asymptotic solution, provided by Roisman (2010).

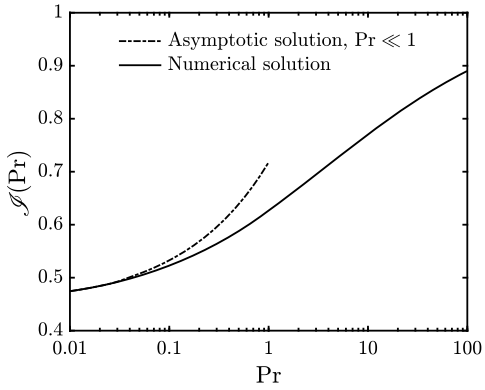

Figure 1.4: The function $\mathscr{I}(\mathrm{Pr})$ for the liquid as a function of the liquid Prandtl number. The function is given as a numerical solution, computed in Roisman (2010) and asymptotic solution for $Pr \ll 1$, as provided in Roisman (2010). Reprint (adapted) from Roisman (2010), with permission of Cambridge University Press, ©2010 Cambridge University Press.

Based on the temperature distribution in the substrate and the equation of heat Roisman (2010) derived the heat flux during the drop impact

$$\dot{q}_\mathrm{w}(t,z) = -\lambda_\mathrm{w}\frac{\partial T_\mathrm{w}}{\partial z} = \frac{e_\mathrm{l}e_\mathrm{w}(T_{\mathrm{w},0} - T_{l,0})}{[e_\mathrm{l} + e_\mathrm{w}\mathscr{I}(\mathrm{Pr_l})]\sqrt{\pi(t-t_0)}}\exp\left[\frac{z^2}{4\alpha_\mathrm{w}\,(t-t_0)}\right], \qquad (1.11)$$

which is verified in Batzdorf et al. (2017).

Further, the total heat during the spreading of the drop and receding are modeled in Batzdorf et al. (2017). The wetting of the spreading droplet initiates the growth of the thermal boundary layer. Therefore, the time of initiation t_0 is a function of the spreading radius $r_\mathrm{s}(t)$. The heat $Q(t)$, removed during the spreading of the drop, can be obtained by the integral of the heat flux over the spreading radius $r_\mathrm{s}(t)$ and depth inside the substrate z as described in Batzdorf et al. (2017).

Their theoretical predictions of the removed heat agree well with numerical simulations for a single drop impact and simultaneous impact of two drops, as shown in Batzdorf et al. (2017). The models do not take the evaporation into account. For this reason, the models provide more reliable values when evaporation is less significant and convection is more important in heat transfer. A higher ratio of convection is the case for high Peclet numbers $\mathrm{Pe} = \mathrm{Re}\,\mathrm{Pr}$ and, thereby, Prandtl numbers.

Drop Deposition with Nucleate Boiling

With increasing surface temperature, the influence of evaporation on the heat transfer during the drop impact increases. The temperature distribution at the liquid-solid interface is not uniform. It is influenced by the appearance and growth of the bubbles, initiated by heterogeneous nucleation at the substrate surface. The temperature at the contact line of each bubble is equal to the saturation temperature. The bubble contact lines move on the substrate since the bubble diameter changes in time: periodically increasing due to evaporation until the bubble detaches (Carey, 1992). The wall superheat $\Delta T = T_\mathrm{w} - T_\mathrm{sat}$ required for nucleation is in the order of 10 K. Therefore, it is possible to approximate the interface temperature by the saturation temperature, T_sat for $T_{\mathrm{w},0} - T_\mathrm{sat} \gg 10\,\mathrm{K}$ to estimate the heat flux roughly. A comprehensive study of the drop deposition regime accompanied by nucleate boiling is given in Breitenbach et al. (2017a). The theoretical approaches are summarized in the following.

As for the single drop impact without nucleate boiling, a thermal boundary develops inside the substrate when the drop wets the substrate. The heat conduction in the substrate can be approximated as one-dimensional since the drop diameter is larger than the thermal boundary layer. The heat conduction inside the substrate is described by the equation of heat, given in equation (1.9). The similarity solution of (1.9) with the boundary conditions of the present regime is known in the form (Baehr & Stephan, 2013)

$$T_\mathrm{w}(z,t) = T_\mathrm{sat} + (T_{\mathrm{w},0} - T_\mathrm{sat})\,\mathrm{erf}\left(\frac{z}{2\sqrt{\alpha_\mathrm{w} t}}\right). \tag{1.12}$$

The heat flux density at the liquid-solid interface can be expressed with the help of (1.12) as

$$\dot{q}(t) \equiv \lambda_\mathrm{w} \left.\frac{\partial T_\mathrm{w}}{\partial z}\right|_{z=0} = \frac{e_\mathrm{w} \Delta T_\mathrm{w}}{\sqrt{\pi\, t}}. \tag{1.13}$$

In Breitenbach et al. (2017a), the overall energy balance of the drop impact is applied for the estimation of the residence time of the drop at the substrate t_r, defined as the total time of drop evaporation at the substrate. The residence time is given in Breitenbach et al. (2017a) as

$$t_\mathrm{nb} = \pi \left[\frac{\rho_\mathrm{l} L^* d_0}{12 k_\mathrm{w} e_\mathrm{w} \Delta T_\mathrm{w}}\right]^2, \tag{1.14}$$

where $L^* = L + \Delta H_0$ is the sum of the latent heat of evaporation L and the enthalpy difference of the liquid at the initial liquid temperature and saturation temperature ΔH_0. The coefficient k_w is determined primarily by the surface structure and wettability. The coefficient k_w also accounts for the effective drop growth due to bubble expansion. This coefficient is in the order of unity and can be determined from the experiments.

The residence times from Breitenbach et al. (2017a) and those found in literature from Abu-Zaid (2004), Buchmüller (2014), Itaru & Kunihide (1978) and Tartarini et al.

(1999) agree well with (1.14), when the adjustable coefficient is set to $k_w = 1.6$. This parameter is equal for all studies since their substrate wettability properties are similar.

Drop Dancing

As the surface temperature increases, nucleate boiling becomes more intense. The typical drop oscillations, normal to the wall, become apparent. These motions are similar to drop dancing. The heat flux is reduced compared to the drop deposition regime with nucleate boiling. Drop dancing is classified as a transitional boiling regime and is poorly understood. A characterization of the regime can be found in Roisman et al. (2018), Breitenbach et al. (2018b), Breitenbach (2018), and Lee et al. (2020).

At high initial surface temperatures, the waiting time t_w until bubbles appear is short (Carey, 1992). In Roisman et al. (2018), a waiting time $t_w < 100\,\mu s$ is estimated for a drop impact in the drop dancing regime onto a smooth aluminum surface. The waiting time is shorter than the spreading time of the drop. Consequently, the bubbles appear already during the spreading of the liquid lamella. Bursting bubbles at the liquid-gas interface lead to many secondary droplets. The ejected mass by secondary droplets increases with the substrate temperature. The phenomenon leads to the reduction of the total drop mass and, thus, to the reduction of the residence time.

Further, some volume of the liquid separates and forms a spherical droplet, hovering continuously above the liquid film. The droplet is connected to the substrate through small liquid bridges to the remaining film at the substrate. The phenomenon is reminiscent of a dancing drop on the substrate. The separated liquid sometimes reunites with the liquid film, and the observed phenomenon is repeated several times (Roisman et al., 2018). This happens especially at relatively low temperatures in the drop dancing regime.

The remaining liquid film is getting less at higher temperatures, and the drop behavior is changing more and more to a drop rebound. The velocity of the ascending drop is low. Accordingly, the height of the droplet is less than the drop radius (Lee et al., 2020).

Descriptions of this phenomenon can be found in Roisman et al. (2018), Breitenbach et al. (2018b), and Breitenbach (2018).

Thermal Atomization

The thermal atomization regime is an outcome regime that can be observed at high surface temperatures and high impact velocities, as shown in Fig. 1.3. The thermal atomization regime is reported in several publications (Senda et al., 1988; Manzello & Yang, 2002; Cossali et al., 2008; Fujimoto et al., 2010; Tran et al., 2012; Shirota et al., 2016; Lee et al., 2020; Castanet et al., 2020), even though different terminologies are used for the same regime. The most promising theoretical approaches to describe the physics of thermal atomization are given by Roisman et al. (2018) and Breitenbach et al. (2018a). The key findings are summarized in the following.

When the drop impacts at the substrate, the liquid spreads at the substrate with a thin liquid lamella (Tran et al., 2012; Breitenbach et al., 2018a). The flow within the lamella is damped as soon as the viscous boundary layer δ_ν reaches the same order of magnitude as the lamella thickness. The resulting lamella thickness h_{res} is given by equation (1.2), as described in section (1.2.1) (Roisman et al., 2018).

The heat transfer from the substrate to the liquid results in a temperature increase and a growing thermal boundary layer within the liquid. At the same time, a strong nucleate boiling can be observed in the liquid lamella. A fine secondary spray is generated by the collapsing bubbles of the nucleate boiling (Cossali et al., 2005). The thickness of the thermal boundary layer is given by $\delta_{\mathrm{t,l}} \approx k_{\mathrm{tb}}\sqrt{\alpha_{\mathrm{l}} t}$, where k_{tb} is an adjustable factor in the order of unity. When the thermal boundary layer reaches the lamella thickness $\delta_{\mathrm{t,w}} \sim h_{\mathrm{res}}$, the liquid is heated fast to the saturation temperature of the liquid (Chaze et al., 2017; Roisman et al., 2018). From this instance on, the heat transferred to the liquid leads to stronger evaporation at the liquid-solid interface. The lamella begins to detach at the lamella rim from the substrate and float. The time until the lamella levitates is modeled by (Roisman et al., 2018) as

$$t_{\mathrm{r}} = \frac{0.6 d_0^2}{k_{\mathrm{tb}}^2 \alpha_{\mathrm{l}} \mathrm{Re}^{4/5}} \frac{\nu^{4/5}}{\nu_0^{4/5}}, \tag{1.15}$$

where ν_0 describes the viscosity at the initial liquid temperature, while ν describes the viscosity of the heated liquid. The theoretical model agrees well with experimental data in Roisman et al. (2018) for $k_{\mathrm{tb}} = 1.0$. Lee et al. (2020) reported that expression (1.15) does not agree with the time in which the liquid is wetting the substrate but with the time until the droplet lifts off, which is equal to the definition of the contact time in Roisman et al. (2018).

The dimensionless dewetting radius is given by Roisman et al. (2018) in the form of

$$\bar{R}_{\mathrm{wet}} \approx 0.65(\bar{t} + 0.25)\sqrt{\ln\left[\frac{\sqrt{\bar{t}_{\mathrm{r}}}(\bar{t}_{\mathrm{r}} + 0.25)^2}{\sqrt{\bar{t}}(\bar{t} + 0.25)^2}\right]}. \tag{1.16}$$

The time is scaled by the impact velocity and initial drop diameter $\bar{t} = (t\, u_0)/d_0$, while the radius r is scaled by the initial drop diameter $\bar{R} = r/d_0$.

Further, the liquid lamella and rim disintegrate into large secondary droplets. At some point, several holes in the lamella appear and expand mainly due to capillary forces (Taylor, 1959) until the entire lamella disintegrates into ligaments and, finally, secondary droplets (Roisman et al., 2018).

The theoretical models have shown that the atomization/break-up mechanisms of the thermal atomization regime are not inertia-dominated but thermally induced. An approach to determine the thresholds of the thermal atomization regime is given in Roisman et al. (2018). More details about the fine spray are given in Breitenbach et al. (2018a).

Drop Rebound

Drop impacts onto very hot substrates lead to drop rebounds. In some publications, the drop rebound regime is further split into wet and dry rebound (Bertola, 2015; Breitenbach et al., 2018b). The wet rebound regime is characterized by substrate wetting and several secondary droplets. No substrate wetting and secondary droplets can be observed in the dry drop rebound regime. Both regimes seem determined by different underlying physics, so they are presented separately.

Wet Drop Rebound

A wet drop rebound is characterized by the spreading and receding of the lamella at the substrate and, finally, the rebound of the liquid. The lamella spreads and recurs on an unstable vapor layer (Bertola, 2015). The vapor layer lowers the shear stresses during the spreading and receding in the liquid lamella (Castanet et al., 2015). After the lamella has contracted, the lower shear stresses allow the droplet to bounce back. Similar behavior can be observed for the isothermal drop impact onto a superhydrophobic surface (Quéré, 2013).

Breitenbach et al. (2018b), Bertola (2015) and Fujimoto et al. (2010) observed several secondary droplets and bubbles in the rebounding drop. They assumed that an ongoing nucleate boiling causes the bubbles and secondary drop. Total-internal-reflection (TIR) measurements from Lee et al. (2020) approved that the vapor layer between the liquid and substrate is unstable, and the liquid wets the substrate. The TIR measurements also showed that the liquid dewets the substrate before the droplet bounces off. Additional X-ray measurements by Lee et al. (2020) verified bubbles in the liquid lamella.

The residence time of the wet drop rebound is in the order of the natural oscillation time t_σ, given in equation (1.8). Lee et al. (2020) describes the residence time by $t_\mathrm{r} \approx \sqrt{\pi}/4\, t_\sigma$. Other investigations have the same scale but other pre-factors instead of $\pi/4$, for example, 0.937 by Biance et al. (2006) or 1.12 by Chen et al. (2007).

The wet drop rebound occurs in a similar temperature range as the thermal atomization regime but at lower Weber or rather Reynolds numbers, as described in Roisman et al. (2018). Wet droplet rebound is classified as an advanced phase of transition boiling due to the unstable vapor layer and partial wetting of the substrate (Breitenbach et al., 2018b).

Dry Drop Rebound

The dry drop rebound is characterized by a fully developed vapor layer separating the liquid lamella of the spreading and receding drop from the substrate, no bubbles inside the rebounding drop, and no ejected secondary drops. X-ray measurements from Lee et al. (2020) visualized the vapor layer and showed no bubbles inside the lamella. The vapor layer remains stable during the drop impact and prevents substrate wetting, as demonstrated by TIR measurements from Lee et al. (2020). The effect of a fully

developed vapor layer between liquid and a very hot substrate is described first by Leidenfrost (1756), which is why it is called the Leidenfrost effect (Leidenfrost, 1966). The phenomenon is labeled as a dynamic Leidenfrost effect in case of an impacting drop.

The Leidenfrost point or Leidenfrost temperature is the onset of the dry drop rebound. Many descriptions of the Leidenfrost temperature can be found in literature. Cai et al. (2020) introduced a theory of the Leidenfrost temperature of a sessile droplet. Wang et al. (2020b), Tran et al. (2012) and Tran et al. (2013) described the influence of the Weber number on the dynamic Leidenfrost temperature.

Many theories on the Leidenfrost temperature are based on the idea that the Leidenfrost point correlates with the liquid superheat limit or homogeneous nucleation temperature. The superheat limit can be either calculated by the spinodal temperature from an equation of state or by the classical nucleation theory (Aursand et al., 2018).

Based on the homogeneous nucleation temperature, a theoretical model of the Leidenfrost temperature is given by Wang et al. (2020b) in the form of

$$\Delta T_\mathrm{L} = \frac{T_\mathrm{hn} - T_\mathrm{l}}{\exp(t_\mathrm{max}/t_\mathrm{th})\mathrm{erfc}\left(\sqrt{\mathrm{t_{max}/t_{th}}}\right)}, \tag{1.17}$$

where T_hn is the homogeneous nucleation temperature following Blander & Katz (1975), $t_\mathrm{th} = \lambda_\mathrm{w}\rho_\mathrm{w}c_\mathrm{p,w}h^2$ is a thermal time scale, $h \approx 8\,\lambda_\mathrm{v}/h_\mathrm{v}$ is a heat transfer coefficient between the drop and heated wall, h_v is the vapor layer thickness, λ_v is the thermal conductivity of the vapor, and $c_\mathrm{p,w}$ is the specific heat of the wall.

Another theory of the Leidenfrost temperature, based on the spinodal temperature T_spin, is given by Castanet et al. (2020) in the form

$$T_\mathrm{L} = T_\mathrm{spin} + f(\mathrm{We},\mathrm{Re})\frac{e_\mathrm{l}}{e_\mathrm{w}}\left(T_\mathrm{spin} - T_\mathrm{l}\right). \tag{1.18}$$

where $f = \sqrt{5}$, derived for a non-viscous flow, for large Weber and Reynolds numbers (e.g., We > 10 and Re > 100) (Castanet et al., 2020).

As observed for the wet rebound regime, the fully developed vapor layer leads to lower frictional forces. The fluid dynamics and residence times are in the same order as in the wet rebound regime. The flow inside the substrate is described in Castanet et al. (2015). According to Castanet et al. (2015) the maximum spreading diameter scales with

$$\frac{d_\mathrm{max}}{d_0} = 1 + 0.23\mathrm{We}^{1/2}. \tag{1.19}$$

for low viscous fluids, for example, water and ethanol. For more viscous fluids, the spreading diameter scales not only by the Weber number but also by the Reynolds number in the way (Castanet et al., 2015)

$$\frac{d_\mathrm{max}}{d_0} = 1 + 7.7\mathrm{x}10^{-2}\mathrm{Re}^{1/5}\mathrm{We}^{1/2}. \tag{1.20}$$

The heat transferred in the drop rebound regime for the particular condition of the isolating vapor layer is addressed by Breitenbach et al. (2017b). The total heat removed by a single drop Q is derived by solving the heat transfer from the substrate through the vapor layer into the evaporation of liquid and sensible heating. Together with the residence time of the drop and an approximation of the wetted area Breitenbach et al. (2017b) expresses the total heat removed by a single drop by

$$Q_{\mathrm{fb}} = \frac{4.63 d_0^{5/2} G\, e_{\mathrm{w}} \left(T_{\mathrm{w},0} - T_{\mathrm{sat}}\right)}{\sqrt{u_0}\left(K_{\mathrm{fb}} + 2G\right)}, \tag{1.21}$$

where K_{fb} is a dimensionless constant

$$K_{\mathrm{fb}} = \sqrt{(B-G)^2 + \frac{4G}{\sqrt{\pi}}} - B - G, \tag{1.22}$$

as well as G and B, given by

$$G = \frac{\sqrt{\pi}\lambda_{\mathrm{v}}\rho_{\mathrm{l}} L}{2\left(T_{\mathrm{w},0} - T_{\mathrm{sat}}\right) e_{\mathrm{w}}^2}; \quad B = \frac{\sqrt{5}\left(T_{\mathrm{sat}} - T_{d,0}\right) e_{\mathrm{l}}}{\sqrt{\pi}\left(T_{\mathrm{w},0} - T_{\mathrm{sat}}\right) e_{\mathrm{w}}}. \tag{1.23}$$

Further, essential publications regarding the drop rebound can be found by Wachters & Westerling (1966), Quéré (2013), Castanet et al. (2015), Breitenbach et al. (2017b), and Castanet et al. (2020).

Understanding the dynamics and heat transfer during single drop impact is also critical to model spray cooling. Models for spray cooling are based on studies and findings regarding the single drop impact onto a hot substrate. In Section 1.2.3, the heat flux during spray cooling in the film boiling regime is modeled. The model is based on the theoretical description of the heat removed by a single drop in equation (1.21).

1.2.3 Spray Cooling

The spray impact on a hot surface is determined by the interactions of the individual impacting droplets with the hot surface. The regime of the spray impact is primarily controlled by the hydrodynamic and thermodynamic interactions (e.g., wetting, nucleate boiling, film boiling) of the single droplet impact. The heat flux density during spray cooling also depends strongly on the thermodynamic effects and the heat flux density of the associated single drop impact regime. Nevertheless, the results from the single drop impact regimes cannot be superpositioned to describe the spray impact. The drop-drop interactions within the spray and during the impact at the substrate surface are essential and significantly influence the outcome of the spray impact (Tenzer, 2020).

The heat flux during spray cooling varies with the surface temperature, single drop impact regimes, and thermodynamic regimes. The dependence of the heat flux on the surface temperature is often shown in the form of a characteristic boiling curve (Tenzer, 2020), well-known from Nukiyama (1966). An illustrative boiling curve is shown in Fig. 1.5. The boiling curve typically determines the regimes of spray cooling and

characteristic temperatures of the regime boundaries. The regimes and characteristic temperatures of the boiling curve are introduced in the following paragraphs.

From high-speed videos from Tenzer (2020), it is known that the individual drops from the spray rebound or splash at high surface temperatures. An isolating vapor layer dominates the drop impact and heat flux. The regime is called film boiling due to the isolating vapor film. The heat flux of the corresponding regime is low and decreases with decreasing surface temperatures (Tenzer, 2020). The heat flux reaches its minimum at the so-called Leidenfrost temperature (Liang & Mudawar, 2017b). For lower surface temperatures, liquid patches appear at the substrate. The heat flux rapidly increases with decreasing temperature until a maximum heat flux is reached. The regime is called the transitional boiling regime and is poorly described in the literature. The temperature at the highest heat flux is the critical heat flux temperature T_{CHF}. For lower surface temperatures, the nucleate boiling regime occurs. The liquid's evaporation rate is relatively low, and the spray accumulates at the substrate, leading to a continuous thin liquid film. The fluid within the film is boiling for temperatures above the saturation temperature (Tenzer, 2020).

Many publications focus on the influencing parameters of the heat flux in the individual regimes and the characteristic temperatures. Ciofalo et al. (2007), Karwa et al. (2007), Cheng et al. (2010), and Gajevic Joksimovic et al. (2023) investigate the influence of the liquid and spray properties on the cooling. The sprays are typically

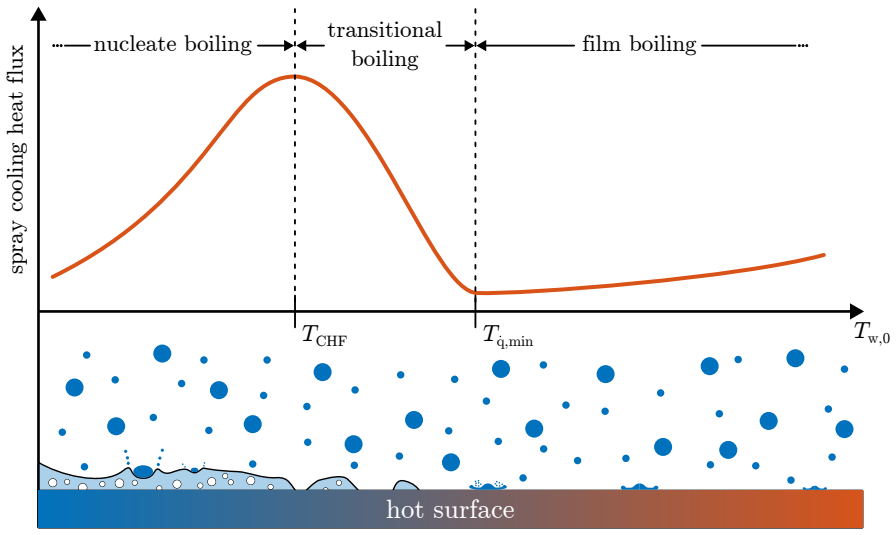

Figure 1.5: Schematic boiling curve and illustration of the spray-wall interactions of different regimes. In the upper part of the Figure is shown a schematic boiling curve, with the characteristic temperatures $T_{\dot{q},\mathrm{min}}$, also called Leidenfrost temperature and T_{CHF} together with the boiling regimes nucleate boiling, transitional boiling, and film boiling. Below is the spray impact in the corresponding regimes illustrated. Reprint (adapted) from Hofmann (2019), with permission from Julian Hofmann, ©2019 Julian Hofmann.

quantified by drop diameter, impact velocity, and mass flux $\dot{m}$, or volume flux $\dot{V} = \dot{m}/\rho_\mathrm{l}$. Sprays are typically polydisperse. Therefore, the drop diameter is quantified by the equivalent drop diameter Sauter-Mean-Diameter (SMD) d_{32}, or average diameter d_{10} (Liang & Mudawar, 2017a). The velocity is quantified by the average drop velocity u_{10} (Liang & Mudawar, 2017a).

The SMD is an equivalent diameter describing a drop diameter with the same ratio of the liquid volume by surface as the entire spray $d_{32} = \sum_i n_\mathrm{i} d_\mathrm{i}^3/(n_\mathrm{i} d_\mathrm{i}^2)$. The SMD is often used when the surface area over mass is essential, as in spray drying or combustion processes. The average diameter d_{10} and drop velocity u_{10} are arithmetic values (Liang & Mudawar, 2017a).

The Reynolds and Weber numbers are also defined differently according to the different equivalent sizes. The Weber number is either defined on the SMD and volume flux or mass flux (Liang & Mudawar, 2017b)

$$\mathrm{We}_{\mathrm{s},32} = \frac{\dot{V}^2 d_{32}}{\rho_\mathrm{l}\sigma_\mathrm{l}}, \tag{1.24}$$

or on the average diameter in the form (Tenzer, 2020)

$$\mathrm{We}_{\mathrm{s},10} = \frac{\dot{m}^2 d_{10}}{\rho_\mathrm{l}\sigma_\mathrm{l}}. \tag{1.25}$$

The Reynolds number is correspondingly defined as

$$\mathrm{Re}_{\mathrm{s},32} = \frac{\dot{m}\, d_{32}}{\nu\rho_\mathrm{l}}, \tag{1.26}$$

or

$$\mathrm{Re}_{\mathrm{s},10} = \frac{\dot{m}\, d_{10}}{\nu\rho_\mathrm{l}}. \tag{1.27}$$

In some cases, the mass flux or volume flux is replaced by the average impact velocity (Liang & Mudawar, 2017b).

In addition to the spray and liquid properties, the influence of the temperature of the liquid and substrate, the solid substrate material (as analyzed by Cebo-Rudnicka et al. (2016) and Tenzer (2020)), and the surface structure (as studied by Sodtke & Stephan (2007); Salman et al. (2019) and Benther et al. (2021)) are studied.

A short introduction of the corresponding spray cooling regimes with boundaries is given in the following. Comprehensive reviews about spray cooling are given by Kim (2007), Cheng et al. (2016), Liang & Mudawar (2017a,b), Breitenbach et al. (2018b) and Wang et al. (2020a). The following introduction is given based on these reviews and further studies.

Spray Cooling in the Film Boiling Regime

The spray cooling in the film boiling regime is characterized by rebounding drops and a low heat flux removed from the substrate. The surface seems repellent to the liquid,

as for the single drop impact regime. The drop may rebound as a single drop or break up into multiple rebounding droplets, depending on the inertia of the spray (Tenzer et al., 2019). No wetting or remaining liquid at the substrate can be observed from macroscopic observation, as described in Tenzer (2020). The residence time of the drops at the surface is short. A review of heat flux correlations is given in Liang & Mudawar (2017b) and Breitenbach et al. (2018b). A direct measurement of the heat flux in the film boiling regime is shown in Labergue et al. (2017) and Tenzer et al. (2019). Breitenbach et al. (2017b) introduces a promising heat flux model, which is further validated by Tenzer et al. (2019).

The interactions between impacting drops are low for sparse spray in the film boiling regime since the residence time of each drop is short and the affected area of each drop is small. Thus, the heat flux can be computed as the superposition of the heat removed by the individual drops. However, the probability of drops interacting with one another must be considered at higher mass fluxes of drops. Drop-drop interactions appear as soon as the spreading of one drop interacts with the spreading of a neighbor drop (in time and space). Breitenbach et al. (2017b) outlined that drop-drop interactions decrease the overall heat flux and must be accounted for in the modeling. Doing this and using previous results for the spreading diameter and time of single drops given in Tran et al. (2012), the heat flux for dense sprays can be obtained in the form

$$\dot{q} = S\, e_{\mathrm{w}}(T_{\mathrm{w},0} - T_{\mathrm{sat}})\eta_{\mathrm{wet}} \tag{1.28}$$

with

$$S = 8.85\,\chi\,\frac{\dot{m}G}{\rho_{\mathrm{l}}\Delta T\,(K_{\mathrm{fb}} + 2G)\,d_{10}^{1/2}u_{10}^{1/2}}, \tag{1.29}$$

where K_{fb} and G are the same dimensionless constants as given in (1.22) and (1.23), η_{wet} is the correction factor for the relative wetted area, and χ accounts for the heat flux during the later stages of drop spreading. The diameter d_0 and speed u_0 in (1.22) and (1.23) are replaced by the average spray diameter d_{10} and speed u_{10}.

The factor η_{wet} is estimated on the assumption of randomly distributed drop impacts on the substrates in space and time, described by the Poisson distribution. The cumulative wetted area on the surface

$$\gamma = \frac{2.1\dot{m}}{\rho_{\mathrm{l}}\,u_{10}}\left(1 + 0.36\,\mathrm{We}_{\mathrm{s},10}^{0.48}\right)^2, \tag{1.30}$$

is expressed, accounting for the superposition of all the drops impacting a unit area per unit of time. Therefore, the correction factor that accounts for the drop interactions at the substrate is

$$\eta_{\mathrm{wet}} = \frac{1 - e^{-\gamma}}{\gamma}. \tag{1.31}$$

The dimensionless constant χ accounts for the heat flux during the later stages of drop spreading, which is not considered in the present analysis. Since the heat flux

density sharply reduces at large times, the value of χ should be approximately unity. The coefficient χ can be estimated by fitting to the experimental data (Tenzer et al., 2019). In Breitenbach et al. (2017b) and Tenzer et al. (2019), this expression predicts very well the heat transfer coefficient for dense sprays impacting substrates in the film boiling regime.

Temperature of Minimum Heat Flux

As shown in equation (1.28), the heat flux decreases with decreasing surface temperature. At a specific temperature, it reaches its minimum. In some publications, the minimum heat flux temperature is declared as the threshold temperature of the film boiling regime. It is assumed to be the lowest temperature, at which a fully developed isolating vapor layer separates the impacting drops from the hot substrate. For this reason, the temperature is often labeled Leidenfrost temperature during spray cooling (Liang & Mudawar, 2017b; Tenzer et al., 2019).

Although the threshold temperature is called the Leidenfrost temperature, the phenomenon of a fully formed vapor layer is not yet directly observed in spray cooling. The so-called Leidenfrost temperature is further described by the temperature of minimum heat flux $T_{\dot{q},\mathrm{min}}$.

The studies from Hoogendoorn & den Hond (1974), Gottfried et al. (1966), Sozbir et al. (2003) and Al-Ahmadi & Yao (2008) reported an influence of the volumetric flux, respectively, the local spray flux on the so-called Leidenfrost temperature. A correlation for high mass flux densities by Yao & Cox (2002)

$$T_{\dot{q},\mathrm{min}} = 14000\,\mathrm{We}_{\mathrm{s}}^{0.013} \tag{1.32}$$

showed a good agreement in Liang & Mudawar (2017b) for multiple data from the literature (Hoogendoorn & den Hond, 1974; Shoji et al., 1984; Choi & Yao, 1987; Yao & Choit, 1987; Ito et al., 1991; Cox & Yao, 1999). Sozbir et al. (2003), Al-Ahmadi & Yao (2008), and Tenzer (2020) reported a weak influence of the drop size and velocity on the temperature of minimum heat flux. These observations contrast the correlation from Yao & Cox (2002), which is based on the Weber number. Al-Ahmadi & Yao (2008) introduced a correlation with the mass flux density

$$T_{\dot{q},\mathrm{min}} = 536.8\,\dot{m}^{0.116}, \tag{1.33}$$

for $\dot{m} = 1.5 - 3.0\,\mathrm{kg\,s^{-1}m^{-2}}$.

Tenzer (2020) reports no influence of the mass flux density or spray parameters on the temperature of minimum heat flux. Instead, a strong effect of the substrate material is described on the temperature of minimum heat flux. Further, Tenzer (2020) describes that the temperature of previous studies tends to scatter around a constant value.

The correlations given are empirical. The underlying effect of the minimum heat flux still needs to be fully understood since the findings are contradictory. This indicates that the physics still needs to be fully understood (Tenzer, 2020).

Spray Cooling in the Transitional Boiling Regime

The spray cooling regime is considered transitional boiling at temperatures below the minimum heat flux. Some drops deposit at the substrate, while others still rebound from the substrate (Tenzer et al., 2019). Deposited drops' residence time is significantly longer than those from rebounding drops. Longer residence times increase the possibility of drop interactions by impacts onto wetted areas. As a result, liquid patches grow by drop impacts onto wetted areas. With decreasing surface temperature, the fluid patches grow quickly at the substrate. The surface is partially covered by a thin liquid film (Tenzer et al., 2019). Changing boundary conditions lead to the name of the regime transitional boiling. The transitional boiling regime is rather complex due to the changing boundary conditions of the drop impacts and increasing interactions between droplets.

The heat flux in the transition boiling regime strongly increases with decreasing substrate temperature. At a specific temperature, the heat flux reaches its maximum. The maximum heat flux temperature is labeled critical heat flux temperature T_{CHF}. Close to the maximum heat flux, the substrate is nearly totally wetted. The heat from the substrate is transferred to liquid heating (sensible heat) and evaporation (latent heat) (Tenzer et al., 2019)). Tenzer (2020) shows the influence of the substrate material, mass flux density, and impact velocity on the heat flux.

A correlation of the heat flux in the transition boiling regime is given by Mudawar & Valentine (1989) in the form

$$\log_{10}\left(\frac{\dot{q}_{\mathrm{TB}}}{\dot{q}_{\mathrm{CHF}}}\right) = 4.78\mathrm{x}10^{5}\left(\frac{u_{10}}{\dot{V}}\right)^{-1.255}\left[\log_{10}\left(\frac{\Delta T_{\mathrm{l}}}{\Delta T_{\mathrm{CHF}}}\right)\right]^{3}\ldots \\ \ldots - 1.90\mathrm{x}10^{4}\left(\frac{u_{10}}{\dot{V}}\right)^{-0.903}\left[\log_{10}\left(\frac{\Delta T_{\mathrm{l}}}{\Delta T_{\mathrm{CHF}}}\right)\right]^{2} \quad (1.34)$$

with the heat flux at the temperature of maximum heat flux $\dot{q}_{\mathrm{CHF}}$, given in (Mudawar & Valentine, 1989), the temperature difference between the wall and the liquid $\Delta T_{\mathrm{l}} = T_{\mathrm{w}} - T_{\mathrm{l}}$, and the temperature difference between the wall temperature at the point of critical heat flux and liquid temperature $\Delta T_{\mathrm{CHF}} = T_{\mathrm{CHF}} - T_{\mathrm{l}}$. A similar correlation is given by Dou et al. (2015).

The correlation considers the influence of the mass flux density and spray impact velocity, as Tenzer (2020) described. The influence of the substrate material and the liquid properties are not considered. Nevertheless, both correlations are purely empirical and are not based on the ongoing physics during transitional boiling. The transitional boiling regime is currently the least studied spray cooling regime (Liang & Mudawar, 2017b).

Temperature of Critical Heat Flux

The critical heat flux and its corresponding temperature are characteristic points in the boiling curve of a spray cooling process. Multiple influencing parameters and models

are reported for the heat flux, such as impact velocity, drop diameter, volumetric flow, and substrate material. The findings on some of the parameters are contradictory: For example, the influence of volumetric flow (Tilton et al., 1989; Chen et al., 2002) and droplet diameter (Tilton et al., 1989; Estes & Mudawar, 1995) on the heat flux. The contradictory results reveal that the mechanism of the critical heat flux still needs to be fully revealed. Multiple heat flux correlations are presented in Liang & Mudawar (2017a).

Most studies focus on describing the heat flux but less on the temperature at which the critical heat flux occurs. A theoretical model of the temperature is defined by Mudawar & Valentine (1989) in the form

$$\Delta T_{\mathrm{CHF}} = 18 \left[\rho_{\mathrm{v}} L \dot{V} \left(\frac{\sigma_{\mathrm{l}}}{\rho_{\mathrm{l}} \dot{V}^2 d_{32}} \right)^{0.198} \right]^{1/5.55}, \tag{1.35}$$

where ρ_{v} is the density of the vapor layer.

In Tenzer (2020), it is presented that the substrate material impacts both the heat flux and the temperature, which is not considered in equation (1.35). However, the mechanisms behind the critical heat flux are still not fully understood, and more research is needed to develop accurate models and gain a better understanding of this phenomenon.

Spray Cooling in the Nucleate Boiling Regime

The nucleate boiling regime starts below the critical heat flux temperature. Grissom & Wierum (1981) and Tenzer (2020) described optical observations of the nucleate boiling regime. The nucleate boiling regime is characterized by droplets wetting the substrate. Grissom & Wierum (1981) describes a partially wetted state in which the impacting mass flux is low so that the entire liquid can evaporate. At higher mass flux densities, a liquid film is generated at the substrate. The spray no longer impacts the dry substrate but onto a thin liquid film.

The heat transfer in the nucleate boiling regime is determined by heat conduction into the liquid film and evaporation. The fast evaporation of the liquid leads to bubbles and ongoing nucleate boiling (Tenzer et al., 2019). The bubbles are growing at the liquid-solid interface and collapse quickly. The phase transition at the three-phase contact line leads to a high heat flux, as Horacek et al. (2005) and Sodtke & Stephan (2007) reported. The surface structure may enhance the heat flux by enlarging the wetted areas and three-phase contact lines for a partially dry substrate (Hsieh & Yao, 2006), but not in the case of a continuous liquid film (Hsieh & Yao, 2006; Tenzer, 2020). Since the heat flux is determined by heat conduction, the substrate material plays a significant role, according to Hsieh & Yao (2006) and Tenzer (2020).

Higher initial liquid temperatures lead to a decreasing heat flux, which can be explained by the lower conductive heat transfer (Tenzer, 2020). According to Tenzer (2020), no influence of the spray impact velocity could be determined.

A heat flux model for the nucleate boiling regime is introduced in Tenzer et al. (2019). The model is valid when the cooling passes quickly through the transitional boiling, which is typically the case. A remote asymptotic solution of the heat flux simplifies it. For this reason, the model is only valid for a fully developed nucleate boiling regime, which means only for times later than the instance of the Leidenfrost $t \gg t_{\mathrm{L}}$. The heat flux is described by (Tenzer et al., 2019)

$$\dot{q} \approx \frac{e_{\mathrm{w}}}{\sqrt{\pi}} \frac{(T_{\mathrm{w},0} - T_{\mathrm{sat}})}{\sqrt{(t - t_{\mathrm{L}})}}. \tag{1.36}$$

The index L denotes the Leidenfrost point or, more precisely, the minimum heat flux point. The model assumes saturation temperature at the solid-liquid interface, even though some liquid superheats can be estimated. This assumption is valid for quickly growing and collapsing bubbles. Breitenbach et al. (2017a) estimated a characteristic time of 1 ms for the bubble formation (Tenzer et al., 2019). The fast cooling and reheating at the solid/liquid interface can only be detected within the resulting thermal boundary layer of the bubbles. At higher distances, the temperature is averaged due to the time dependence of the thermal boundary layer (Tenzer et al., 2019).

1.3 Aim and Outline of the Thesis

Currently, the best approaches to model spray cooling are based on the results of single drop impacts on a hot substrate since this phenomenon is a fundamental part of spray wall interactions. Many findings related to drop deposition with and without nucleate boiling and film boiling are reported in the literature. Based on these findings, reliable heat flux models in the nucleate and film boiling regimes are developed, as shown in Section 1.2. However, single drop impacts and spray/wall interactions related to transitional boiling are not yet comprehended and lack reliable models that account for the relevant physical phenomena.

This study aims to enhance the understanding of spray cooling related to transitional boiling by investigating the single drop impact and transferring the single drop results to spray cooling by considering the drop interactions at the surface. In the case of the single drop impacts, the focus of the present study is on regimes with impact parameters between the drop deposition accompanied by nucleate boiling and dry drop rebound regime. These regimes are associated with transitional boiling, as they are not solely dependent on the steady nucleate boiling within the liquid lamella or a stable vapor film separating the liquid from the substrate. Furthermore, it is necessary to address the drop-drop interactions at the substrate to transfer the findings from single drop impact to spray cooling and develop reliable models. Finally, the findings of the single drop impact regimes need to be transferred to the spray impact to improve the understanding of spray cooling.

This dissertation consists the following chapters:

The experimental methods, including the experimental setup, post-processing of the

experimental data, and data reliability, are introduced in Chapter 2. The experimental methods comprise the setup to observe the drop impacts and measure the heat flux during the drop impact and characteristic times, such as the drop residence time. Further, the capabilities of the setup and post-processing are explained, including the possible error sources.

The single drop impact for the main outcome regimes associated with transitional boiling: drop dancing, wet drop rebound, and thermal atomization are studied in Chapter 3. In the drop dancing regime, the characteristic time from which the drops start to hover above the substrate is measured. This characteristic time, termed percolation time, is modeled based on the assumption of percolating vapor bubbles forming infinite vapor clusters. The threshold temperature between the drop dancing and wet drop rebound is determined by the drop residence time. The threshold temperature, also called thermosuperrepellency temperature, is theoretically described by the instance when the percolation time is in the order of the natural drop oscillation time, that drops can rebound without delay in the wet rebound regime. It is shown that the experimental and theoretical threshold temperatures agree well. Finally, the heat flux, removed from the hot substrate, is measured with a high spatial and temporal resolution in the thermal atomization regime. The heat flux is modeled two-dimensional on the assumption of direct wetting and heat conduction at the liquid/solid interface. The experimental data and theoretical prediction are in the same order of magnitude.

In Chapter 4, the interactions between drops are considered, which is essential when transferring single drop results to spray cooling. The focus of the study is on drop trains impacting in the drop rebound regime to understand better how short-lasting drop impacts interact. During the cooling, the impacting drops cause a temperature gradient within the substrate, which is measured. The temperature decrease is modeled by the superposition of the heat, removed by each impacting drop. The experimental and theoretical results are in good agreement. Additionally, the theory is utilized to describe the formation of liquid patches during spray cooling. These patches are formed due to the interaction of drops at wall temperatures close to the thermosuperrepellency temperature.

In Chapter 5, the results obtained from the drop dancing regime and drop interactions are used to model the heat flux during spray cooling in the transitional boiling regime. The theoretical predictions of the model agree well with the experimental heat flux obtained from Tenzer (2020) for sprays with low number flux. Moreover, the so-called Leidenfrost temperature, associated with the minimum heat flux during transient spray cooling, is determined. It is shown that the Leidenfrost temperature for sprays correlates very well with the theoretically predicted thermosuperrepellency temperature. This finding indicates that the minimum heat flux temperature is not determined by the onset of film boiling but by the appearance of thermosuperrepellency caused by the percolation of vapor channels at the liquid/substrate interface.

In Chapter 6, the findings and theories of the present thesis are concluded, together with an outlook on future research topics.

2 Experimental Methods

The experimental methods to investigate single drop phenomena are described in the present chapter. In Section 2.1 is given an overview of the different setup configurations used to observe the single drop impact and investigate the temperature distribution at the contact interface of the hot substrate and liquid. The postprocessing of the experimental data is presented in Section 2.2. The single drop setup is a modification of the system first designed in Breitenbach (2018). The design is partly revised and adapted.

Parts of this chapter, including text and some figures, are published in Schmidt et al. (2018, 2019, 2021a,b, 2022, 2023a,b).

2.1 Experimental Setups to Study Single Drop Impacts

Two configurations of the experimental setup for single drop impacts are used in this work. One is used to study the outcome of drop impacts onto metal targets, shown in Fig. 2.1 (a), and the other is used to visualize the surface temperature and estimate the heat flux during the impact of a drop, shown in Fig. 2.1 (b).

A custom drop generator generates single drops and drop trains. The drops are accelerated by gravity towards the heated substrate. The impact is recorded from the side using a shadowgraphy setup. The metal impact substrate is equipped with an array of thermocouples to measure the temperature evolution. The second setup uses a high-speed thermographic camera to record the temperature at the substrate interface exposed to the collision of a drop. The main components of the design are presented in more detail in this section. The entire setup is placed into an air-conditioned housing to control the ambient conditions and reduce contamination by dust.

Drop Generator

Single drops and drop trains of water with a diameter of $d_0 = 2.3\,\mathrm{mm}$ are generated by dripping from a needle. An *Aladin Al-1010* syringe pump feeds a hydrophobic G27 blunt needle *(Braun Sterican)*. The drops are released when the gravitational force exceeds the force due to the surface tension of the liquid. This principle leads to constant drop diameters. Single drops are generated by applying the critical volume so that the drop drips off. A train of drops is generated by applying a continuous liquid flow rate. The number flux $\dot{N}$ of the drop train is set between $0.9\,\mathrm{Hz}$ and $5.7\,\mathrm{Hz}$ within this study.

To maintain the liquid properties, the liquid and drop generator must be cooled.

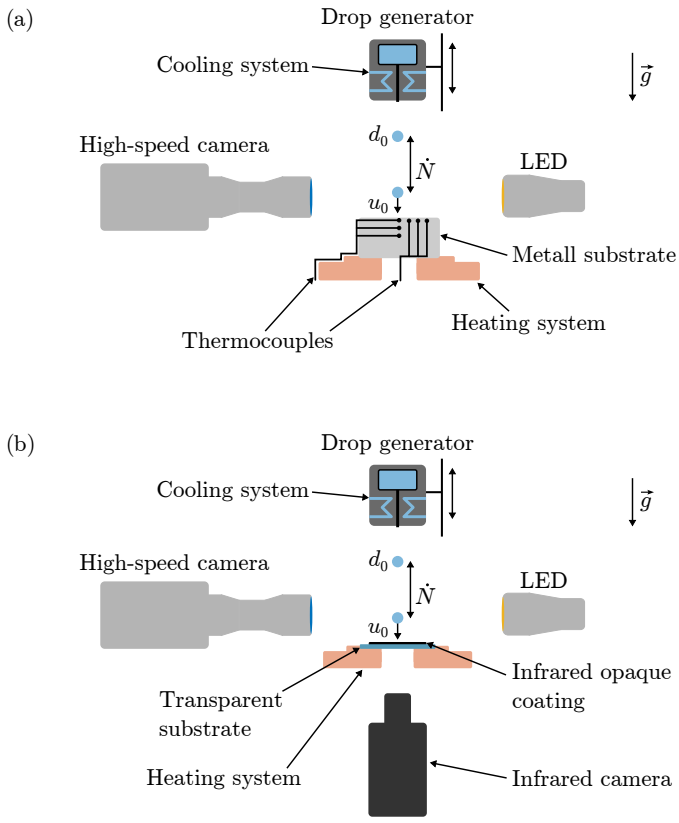

Figure 2.1: Sketches of the experimental setups to investigate the single drop experiments. (a) The design includes an adjustable drop generation unit, a heated metal impact target, and a high-speed observation system. (b) The impact target is replaced for infrared measurements during the drop impact. The heater provides bottom-view optical access for a high-speed infrared camera.

Otherwise, the liquid would heat up since the drops are generated above the heated substrate. A *Lauda RC 20CS* temperature bath is connected to the drop generator to maintain the drop generator and liquid temperature $T_{\mathrm{d},0}$ constant at 20 °C. A thermocouple type K (*class 1*) is used to monitor the needle temperature close to the end of the needle.

The height of the drop generator above the hot substrate can be set with a linear traverse. By changing the height of the needle, the impact velocity can be changed in the range of $u_0 = 0.4\,\mathrm{m\,s^{-1}}$ to $2.0\,\mathrm{m\,s^{-1}}$.

The liquid in the experiments is double-distilled water. The liquid properties of water are taken from VDI e.V. (2013). The properties are given in Table 2.1.

Property	Symbol	Unit	Value
Density	ρ_l	$\mathrm{kg\,m^{-3}}$	998.21
Heat capacity	$c_{\mathrm{p,l}}$	$\mathrm{J\,kg^{-1}\,K^{-1}}$	4185
Thermal conductivity	λ_l	$\mathrm{W\,m^{-1}\,K^{-1}}$	0.598
Surface tension	σ_l	$\mathrm{N\,m^{-1}}$	72.74×10^{-3}
Kinematic viscosity	ν_l	$\mathrm{m^2\,s^{-1}}$	1.003×10^{-6}

Table 2.1: Fluid properties of water at a liquid temperature $T_{\mathrm{d},0} = 20\,°\mathrm{C}$, taken from VDI e.V. (2013)

Shadowgraphy Imaging

A shadowgraphy imaging setup is used to observe the drop impact phenomena. Further, it is used to measure the drop diameter, impact velocity, and residence time of the drops. The high-speed CMOS camera *Vision Research Phantom V12.1* records the drop impacts. Drop impacts in the film boiling regime rebound shortly after the impact. Due to the short residence time, the framerate is set to 6200 fps. The optical resolution is set to 1280 x 800 px. Drop impacts in the drop deposition regime last longer. The framerate is reduced to 3000 fps to reduce the required storage. The camera is equipped with a telecentric lens and a telecentric backlight light LED for measurement purposes, and a 60 mm endocentric lens in combination with a diffusive backlight for optical observations.

The telecentric lens *Opto Engineering TC016M036* has a magnification of 1 resulting in a spatial resolution of $20\,\mathrm{\mu m\,px^{-1}}$. The telecentric backlight (*Opto Engineering LTCLHP036-G*) has a wavelength of 525 nm. The setup ensures measurements with a good resolution and low image distortion. Only parallel light rays are recorded with the telecentric configuration. This results in an almost perfect two-dimensional projection of the scene. Further, an object's image size does not change with its distance from the optics. The parallel light lowers reflections at the liquid-air interface. At the same time, it makes observations inside the droplet almost impossible.

A 60 mm micro lens (*Nikon AF NIKKOR 1:2.8 D*) is used for a good visibility

of bubbles and boiling effects inside the drops. Spacer rings (Nikon PK) are used between the camera and lens to increase the magnification. The micro lens has a spatial resolution of 12.6 µm px^{-1}. In the case of the micro lens, the high-power LED *Veritas Constellation Constellation 120E* is used as backlight illumination. The LED is placed behind a Light Shaping Diffusor from *Luminit* with a circular diffraction angle of 80°. The backlight, in combination with the diffuser, ensures a bright, homogeneous backlight illumination. The optical setup with the 60 mm micro lens is further analyzed in Breitenbach (2018).

Metal Impact Substrates

Various target materials are used to identify their influence on the drop impact outcome: Aluminum (EN AW 7075), copper (CW004A), and stainless steel (1.4841). The surface of all impact targets is smooth mirror polished.

The surface of the stainless steel substrate is polished using a *Struers* polishing machine in multiple steps. The final step contains polishing with a 0.25 µm diamond suspension. The surface roughness is about $S_a = 10.8$ nm. The substrate has a diameter of 50 mm and a height of 25 mm. At the top is a flange. The substrate is mounted to a custom heating structure in an insulating housing. The target temperature at the surface $T_{w,0}$ can be controlled from room temperature up to 550 °C.

A thermal boundary layer develops inside the substrate when a drop impacts at the surface. The temperature evolution inside the substrate is measured with an array of thermocouples in axial and radial directions. The evolution, orthogonal to the impact surface, is measured with seven thermocouples, beginning 1 mm below the surface. Between the thermocouples is a distance of 3.5 mm. The radial evolution is measured 0.5 mm below the surface, with a radial distance of 3.5 mm between the thermocouples. All thermocouples are calibrated type J thermocouples (class 1), shielded, but with an open tip. The diameter of the thermocouples is 0.5 mm. The holes of the thermocouples are processed with spark erosion and have a diameter of 0.6 mm. The thermal conductive ceramic adhesive *Aremco Ceramabond 569 VFG* ensures good thermal conductivity between the thermocouples and the substrate. The temperature signals are recorded with 95 Hz using two data acquisition modules (*NI 9212*) from *National Instruments*. A sketch of the impact substrate is shown in Fig. 2.2 (a).

The custom substrate heater consists of a two-parted copper structure. Inside is a flexible tubular heater with a thermal power of 400 W. The copper structure is designed to provide an equal temperature distribution at the interface to the impact substrate. The copper is nickel-plated to avoid oxidizing. The heater's temperature is controlled with a *c448* controller from *hotset*. The entire heater and impact surface are placed into an isolating housing of *Kelutherm 800M* with low thermal conductivity. To improve thermal isolation, all free spaces inside the housing are filled with low-conductive mineral wool. The top of the structure is covered with a thin metal sheet to protect the assembly against water. A sketch of the assembly is shown in Fig. 2.2 (b).

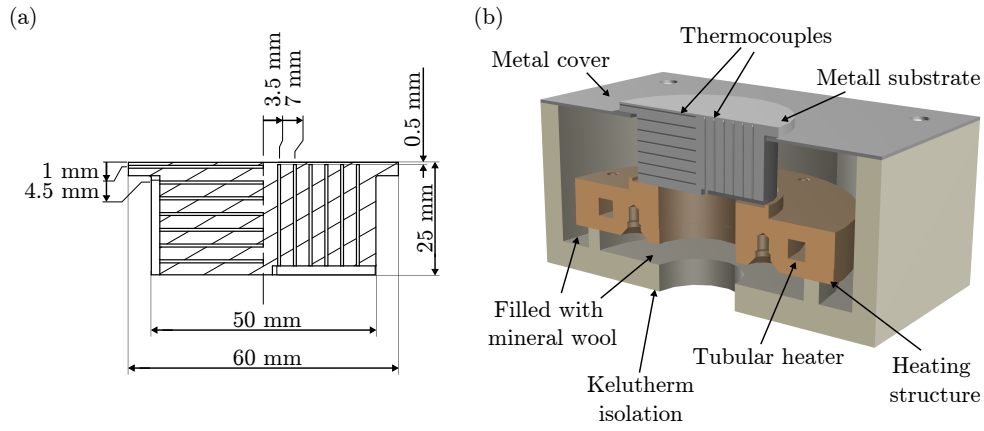

Figure 2.2: Sketches of the stainless steel impact substrate and heating structure to heat the metal substrate. (a) Drawing of the stainless steel impact target, including the holes at which the thermocouples are placed. (b) Sectional view of the heating structure, including the isolation and impact substrate.

Material	Density $\mathrm{kg\,m^{-3}}$	Heat capacity $\mathrm{J\,kg^{-1}\,K^{-1}}$	Thermal conductivity $\mathrm{W\,m^{-1}\,K^{-1}}$
Stainless steel (1.4841)	7900	542	16
Aluminum (AW 7075)	2700	984	236
Copper (CW004A)	8930	386	394

Table 2.2: Material properties of the metal substrates used in the single drop experiments.

The drop impact experiments onto aluminum and copper substrates are performed in the framework of Breitenbach (2018). Each substrate has a thickness of 20 mm and a diameter of 50.8 mm. The surfaces are mirror polished with an approximate roughness of $S_\mathrm{a} = 50\,\mathrm{nm}$. The temperature of the samples is measured with a thermocouple 1 mm below the surface. The thermocouple is a calibrated, type J (class 1) thermocouple. It is shielded, with a diameter of 1 mm. The impact substrates are heated up to 450 °C by a custom heater. The heater has a total heating power of 250 W. Further details about the heater can be found in Breitenbach (2018).

The material properties of all metal substrates used in the single drop experiments are given in Table 2.2.

Infrared Transparent Impact Substrate

In the case of the infrared measurements, the drop impacts onto an IR transparent sapphire substrate. The sapphire substrate is placed onto the same custom heater as the stainless steel substrate. A smaller ceramic isolation replaces the surrounding isolation, shown in Fig. 2.3 (a), to achieve better optical accessibility. The ceramic

isolation has an opening in the center, which allows recording of the infrared radiation from below. In addition, the ceramic isolation compensates for the lower height of the sapphire substrate compared to the metal substrates when recording from the side. The optical path for the infrared rays is symbolized with a red arrow. The optical path for the side view observation is indicated with a blue arrow. The ceramic isolation is made of *C130*. All free spaces inside the ceramic are filled with low-conductive mineral wool to improve thermal isolation.

The sapphire substrate is shown in Fig. 2.3 (b). The substrate has a thickness of 3 mm and diameter of 50 mm. The sapphire substrate is transparent to wavelengths up to 5 µm. At the same time, it is resistant to temperature shocks. The upper surface of the substrate is coated with highly infrared emissive CrN coating. The coating has a thickness of approximately 600 nm. It is applied by phase vapor deposition PVD by the Center for Structural Materials of the TU Darmstadt.

A high-speed mid-wave infrared (MWIR) camera (*FLIR X6901 SC*) is placed below the heater. The camera captures infrared radiation with wavelengths from 3 µm to 5 µm. The maximum optical resolution of the camera is 640 x 512 px, with a maximum fullframe framerate of 1004 fps. The optical resolution is lowered to 640 x 332 px, to achieve a framerate of 1500 fps in the present study. The camera is equipped with an IR lens, with a focal length of 50 mm. A 1 inch spacer is used to increase the magnification to a spatial resolution of 29.35 µm px^{-1}. The camera saves the captured infrared radiation as digital counts with a theoretical 14-bit dynamic range (0 to 16 383). A calibration is necessary to convert the digital counts to a temperature. The calibration takes into account the coating emissivity, substrate transmissivity, and general ambient conditions along the optical path. The calibration has to be done for each integration time of the camera. The integration time is similar to the exposure time of a regular camera.

Experimental Procedure

All impact substrates are cleaned at the beginning of each day with isopropyl alcohol. After cleaning, the surface is wiped with double distilled water. The water receding during the wiping is observed to ensure uniform water distribution on the substrate. If the water is not receding equally, the surface is cleaned again. If the cleaning procedure is insufficient, the metal substrates are polished with a 0.25 µm diamond suspension. The surface is dried using an air blower when the water recedes equally.

The impact surface is heated to the desired surface temperature before each single drop experiment. The drop is released after the surface temperature is steady. A laser light barrier triggers the recording of the impact. The infrared camera is triggered at the same time and is synchronized with the high-speed camera. The video data and initial surface temperature are stored for further processing.

The measurement procedure for drop train experiments differs slightly. The substrate is initially heated to a surface temperature of $T_{\mathrm{w},0} = 550\,^{\circ}\mathrm{C}$. After the system is in

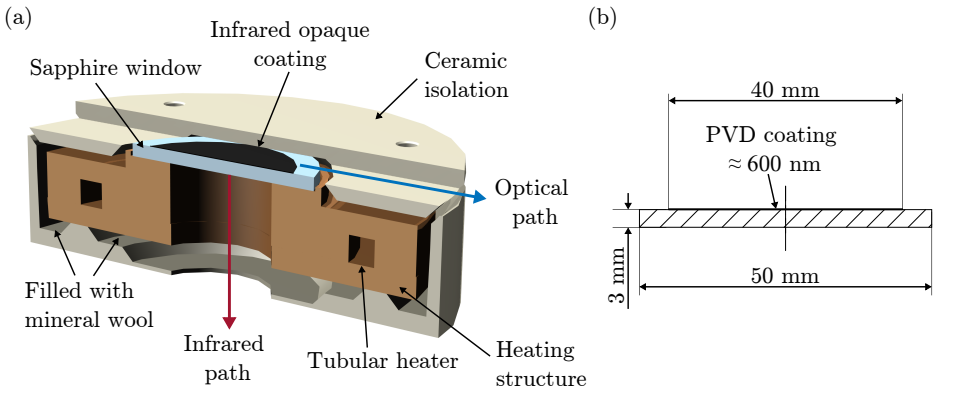

Figure 2.3: Sketches of the heater and impact substrate, used to measure the infrared radiation during single drop experiments. (a) Sectional view of the heating structure, including the isolation and impact substrate. The blue arrow symbolizes the optical path of the side-view observations, while the red arrow symbolizes the optical path of the infrared camera. (b) Drawing of the sapphire substrate with a CrNcoating on top. The CrN has a high infrared emissivity. The coating has a thickness of approximately 600 nm

steady state, the heating system is switched off, and a constant drop train is applied to cool down the impact target. The first drop impacts are recorded from the side to check the drop number flux, diameter, and impact velocity. Further drop impacts are recorded during the experimental run at certain temperatures of interest. The temperature evolution T_w is recorded during the cooling. The drop train is applied until the target cools down to a surface temperature of $T_w \approx 140\,°C$. The experiments are repeated three times for each parameter setting. The experimental data are averaged over these three repetitions.

2.2 Processing and Analysis of Experimental Data

The experimental data are processed after the recording to obtain the variables of interest, such as droplet diameter, impact velocity, droplet residence time, contact temperature, and heat flux density. The optical setup and infrared camera are calibrated to obtain reliable data from the recorded experiments. Finally, the generated measured values are validated for their accuracy or repeatability to assess the degree to which theoretical models can be compared with the measurements. These proceedings are summarized in the present section.

2.2.1 Characterization of the Shadowgraphy Imaging

The optics and settings of the recording determine the capabilities of the shadowgraphy imaging system. The recordings to measure the drop diameter, impact velocity, and residence time are performed with the telecentric setup. For this reason, the capabilities

of the telecentric setup are presented in the following.

Spatial Resolution

The spatial resolution x_{res} is determined by the lens's magnification, the camera's pixel size, and the optics' resolving capacity. The lens in the present setup has a magnification of 1. This means an object is displayed at the camera sensor in its original size. The sensor pixel size x_{px} determines the spatial resolution $x_{\mathrm{res}} = x_{\mathrm{px}} = 20\,\mu\mathrm{m\,px}^{-1}$.

The spatial resolution has to match the resolving capacity of the lens. The resolving capacity is the lens's physical resolution limit, determined by light diffraction at the lens aperture. It describes the minimum distance between two dots, which still can be resolved. Smaller distances lead to overlapping diffraction patterns. As a consequence, both points can not be separated from each other. A smaller pixel size than the resolving capacity would not result in a higher spatial resolution. The image would get blurred by the intersecting diffraction patterns. The diffraction limit is determined by the Rayleigh criteria (Pedrotti et al., 2005)

$$\Delta x_{\mathrm{min}} \approx 1.22\,\frac{\lambda_{\mathrm{ray}}\,f}{d_{\mathrm{ap}}} = 1.22\,\lambda_{\mathrm{ray}}\,A_{\mathrm{N}}, \tag{2.1}$$

with the resolving capacity Δx_{min}, the wavelength of the light λ_{ray}, working aperture $A_{\mathrm{N}} = f/d_{\mathrm{ap}}$, the focal length f, and aperture diameter d_{ap}. The wavelength in the present study is $\lambda_{\mathrm{ray}} = 525\,\mathrm{nm}$, and working aperture $A_{\mathrm{N}} = 16$. The resolving capacity of the telecentric lens is $\Delta x_{\mathrm{min}} \approx 10.25\,\mu\mathrm{m}$. The resolving capacity is lower than the pixel size of the camera resolution. This allows the recording of sharp images without diffraction blur.

The resolving capacity of the lens does not limit the spatial resolution. Hence, the spatial resolution is determined by the camera pixel size and magnification of the lens. The shadowgraphy setup can not detect structures or events smaller than $20\,\mu\mathrm{m}$. Each interface is captured with a maximum error $20\,\mu\mathrm{m}$.

The image quality is further determined by the depth of field (DOF). The depth of field describes when a point is imaged blurred since it is out of focus. Every point in the focal plane of the lens is brought into focus on the imaging plane or camera sensor. A Point out of the focus plane is displayed as a larger spot at the imaging plane. The DOF describes the distance from the focus plane, at which a point is still imaged cleared. The DOF of an endocentric lens depends on the aperture, focal length, and f-number. A telecentric lens has an infinite focal length. Therefore, the DOF is theoretically infinite, too. In practice, the DOF is limited. The DOF is measured in the present study using DOF calibration target *DOF 5-15* from *Edmund optics*. The measurements resulted in a DOF of 8 mm.

Temporal Resolution

The system's temporal resolution depends on the camera's framerate and exposure time. The framerate of 6200 fps leads to a temporal resolution of $t_{\mathrm{res}} = 0.16\,\mathrm{ms}$. The

framerate of 3000 fps reduces the temporal resolution to $t_{\mathrm{res}} = 0.33\,\mathrm{ms}$. The temporal resolution limits the phenomena that can be captured. No event, happening within 0.16 ms, respectively 0.33 ms can be detected with the shadowgraphy setup. Further, each event is captured with a maximum error 0.16 ms, respectively 0.33 ms.

The exposure time determines the image's brightness and if motion blur affects the recording. The exposure needs to be long enough to guarantee bright images. At the same time, the exposure time must be short enough to avoid overexposure and motion blur. Motion blur occurs when the imaged interface moves more than the spatial resolution within the exposure time. Consequently, the interface would be captured by two or more pixels. The image would be blurry in the direction of the moving interface. The maximum value of the exposure time t_{ex} can be calculated by the fastest speed u_{max}, which has to be recorded, and the pixel size Δx_{px}

$$t_{\mathrm{ex}} = \frac{x_{\mathrm{res}}}{u_{\mathrm{max}}}. \tag{2.2}$$

The fastest phenomenon, which is measured, is the highest impact velocity $u_{\mathrm{max}} = u_0 = 2.0\,\mathrm{m\,s^{-1}}$. The spatial resolution is $x_{\mathrm{res}} = 20\,\mu\mathrm{m}$. The minimum exposure time is $t_{\mathrm{ex}} = 10.00\,\mu\mathrm{s}$. The exposure time in the present experiments is a bit further decreased to 8.00 µs.

Image processing

The side-view recordings of each measurement are processed manually to determine the residence time t_{r}.

As a first step, each video is reviewed manually to select the first image, at which the impacting drop contacts the substrate. This image represents the time t_0. Secondly, the first image is selected, at which no liquid from the initial drop impact remains at the substrate. The duration between both images represents the residence time of the drop t_{r}.

The drop diameter d_0 and impact velocity u_0 are measured with a custom script based on established image processing functions from *MathWorks Matlab*, including the Matlab Image Processing Toolbox and functions from Vision Research. The high-speed videos are loaded directly into the Matlab workspace. Each image from the recording and the camera settings can be directly accessed in Matlab without any information loss. An exemplary original image is shown in Fig. 2.4 (a).

As a first step, the grayscale images are binarized. A global threshold for the conversion is computed following the method from Otsu (1979). The threshold is calculated for a single image and used for the entire video. Particles and dirt on the optics are detected and removed from the image. The particles are typically very small in the order of a few pixels. Therefore, all areas smaller than a threshold of a few pixels are removed from the image. The binarized image is shown in Fig. 2.4 (b).

The script automatically detects the drop edge and drop cross-sectional area in the binarized image. Based on the cross-sectional area A, an equivalent diameter is

computed by the equation $d_\mathrm{i} = \sqrt{4A/\pi}$. Further, the centroid position of the area is computed.

The movement of the drop is tracked by the positions of the area centroid over time. The drop velocity is calculated by the change of the centroid position $\Delta x_{\mathrm{centroid,i}}$ and the time between two images t_res: $u_\mathrm{i} = \Delta x_{\mathrm{centroid,i}}/t_\mathrm{res}$. The detected drop edge and centroid are shown in Fig. 2.4 (c).

The equivalent diameter d_i and impact velocity u_i are averaged over a few images n before the drop impact to get the drop diameter $d_0 = (\sum_{i=1}^{n} d_i)/n$ and impact velocity $u_0 = (\sum_{i=1}^{n} u_i)/n$.

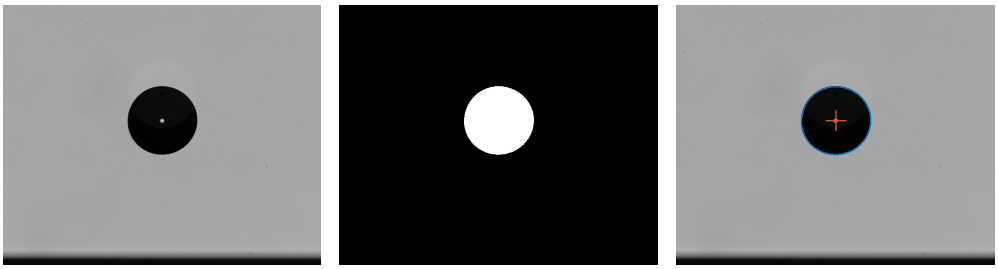

(a) Original image (b) Binerized image (c) Detected drop

Figure 2.4: Steps to measure the drop diameter and impact velocity of an impact drop. In (a) is shown a raw grayscale image. The images get binarized during the processing to detect the drop shape and cross-sectional area. The binarized image is shown in (b). The detected drop edge and centroid of the cross-sectional area are shown in (c).

Uncertainty During Single Drop Impacts

The measurement of the drop diameter, drop impact velocity, and residence time are affected by multiple error sources. First of all, the measurements are limited by the spatial and temporal resolution of the measurements. Moreover, the time measurements, e.g., the residence time, are affected by stochastic phenomena, depending on the drop impact regime. As a result, the drop residence time t_r scatters. It scatters partly due to the nucleation and repelled mass by secondary droplets (Breitenbach, 2018). The scatter depends on the drop impact regime since different phenomena determine each regime.

In Fig. 2.5 the cumulative average residence time is shown as a function of the number of measurement repetitions for the drop deposition and drop rebound regime. The cumulative average residence time of a drop impact in the drop deposition regime, accompanied by nucleate boiling, is shown in Fig. 2.5 (a). The residence times are measured for drop impacts onto a hot stainless steel substrate with a surface temperature of $T_{\mathrm{w},0} = 220\,^\circ\mathrm{C}$. This is the highest temperature clearly belonging to the drop deposition accompanied by nucleate boiling regime. The nucleation fluctuates strongly between measurements, as well as the number and size of secondary drops ejected from

the liquid lamella. The number and size of secondary droplets determine the rejected and remaining liquid mass. This significantly influences the evaporation time and leads to large scatter of the residence time. This is considered for measurements related to a strong ongoing nucleate boiling.

The cumulative average residence time in the drop rebound regime is shown in Fig. 2.5 (b), as a function of measurement repetitions. The residence times are measured for drop impacts onto a hot stainless steel substrate with a surface temperature of $T_{w,0} = 430\,°C$. The drop rebound regime is characterized by a vapor-dominant layer separating the drop from the substrate. The regime is not significantly influenced by an ongoing nucleation. For this reason, the residence time scatters less. Fewer repetitions are required to achieve reliable measurements.

The lowest residence time of a drop impact in the drop deposition regime is in the order of 240 ms, as shown in Fig. 2.5 (a). The error in measuring the residence time is determined by detecting the drop impact and the last frame before the drop is fully evaporated. The maximum error for each time is 0.33 ms and in total 0.66 ms. The resulting measurement error due to the temporal resolution is less than 1 %.

The residence time of a drop impact in the film boiling regime is in the order of 20 ms, as shown in Fig. 2.5 (b). The error to measure the residence time is determined by detecting the drop impact and the last frame before the drop is rebounded. The maximum error for each time is 0.16 ms and in total 0.33 ms. The resulting measurement error due to the temporal resolution is less than 2 %.

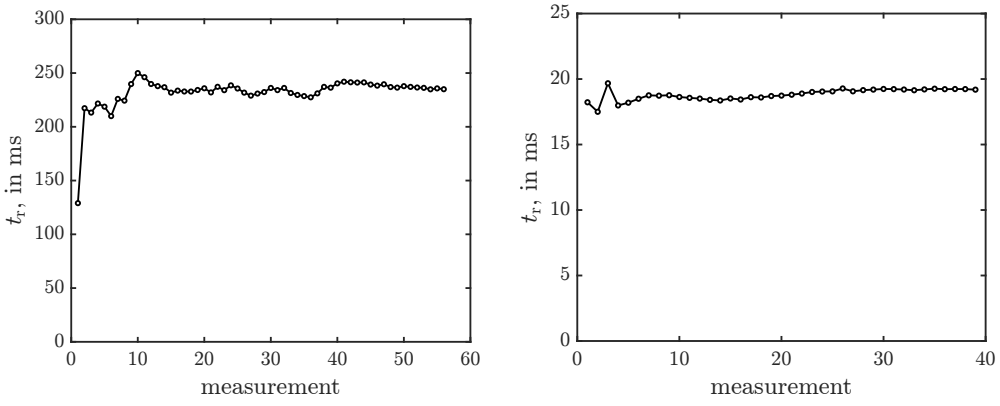

(a) Drop deposition

(b) Drop rebound

Figure 2.5: Cumulative average residence time of drop impacts in different drop impact regimes. In (a) is shown the cumulative residence time of drop impacts in the drop deposition regimes, accompanied by nucleate boiling. The substrate in the present case is a stainless steel substrate, and the surface temperature is $T_{w,0} = 220\,°C$. The cumulative residence time of drop impacts in the drop rebound regime is shown in (b). The drops impact onto a 430 °C hot stainless steel substrate. The residence times scatter less.

2.2.2 Thermal Measurements During Drop Impact

Two temperature measurement techniques are used in the present study. The first temperature measurement technique is thermocouples embedded in the metal substrates. The second technique is the thermal imaging using a high-speed infrared camera. In the following, both techniques and the processing of the experimental data are further specified.

Temperature Measurements using Thermocouples

The initial wall temperature $T_{\mathrm{w},0}$ during the single drop experiments is steady state, right before the drop impact. The temperature is measured by a thermocouple 1 mm below the substrate surface. The thermocouple is of the type J, with the tolerance class 1. The maximum deviation is 1.5 °C, respectively $0.004 \cdot T$ according to the international norm EN 60584-2.

A large set of thermocouples is used to measure the evolution of the thermal boundary layer during the impact of a drop train onto a stainless steel target. The thermocouples are of type J and tolerance class 1. The maximum deviation is 1.5 °C, respectively $0.004 \cdot T$ according to the international norm EN 60584-2. The diameter of the thermocouples is 0.5 mm and the tip of the thermocouple shield is open to reduce the time response. The response time represents the time until 63.2 % of an instantaneous temperature change is measured with the thermocouple. The response time of the present thermocouples is in the order of 0.1 s.

The drop train experiments last significantly longer than the single drop experiments. For this reason, convectional losses have to be considered. The convectional losses are measured by cooling the substrate without a drop train. The substrate is initially heated to a surface temperature of $T_{\mathrm{w},0} = 550\,^{\circ}\mathrm{C}$, like in the drop train experiments. After the system is in steady state, the heating system is switched off, but no drop train is applied to cool down the impact target. The substrate cools down only by convectional losses. The temperature evolution $T_{\mathrm{w,cal}}$ during the cooling is recorded. The convectional cooling measurement is repeated three times. The cooling by the drop train and pure convection are synchronized during the post-processing. The temperature drop by the drop train is determined by subtracting the drop train temperature evolution T_{w} from the temperature evolution without drop train $T_{\mathrm{w,cal}}$.

Thermal Imaging of Single Drop Impacts

The thermal imaging setup allows recording the contact temperature during the drop impact with a high temporal and spatial resolution. To achieve reliable temperature measurements, several influencing factors must be considered.

A highly infrared emissive coating is needed at the interface between the drop and the transparent solid substrate. The emitted radiation's intensity and infrared measurement's signal-to-noise ratio increase with the emissivity of the coating. The coating has to be opaque to block any radiation from above. A highly IR emissive and,

at the same time, a thin PVD coating, made of CrN, is provided by the Center for Structural Materials of the TU Darmstadt. The coating is well established and tested (Fischer, 2015; Gholijani et al., 2022). The emissivity of the coating is unknown and has to be measured after it is applied to the substrate.

The used substrate has to be highly transparent so as not to affect the transmission of the coating's IR radiation. The material transmissivity depends on its reflectivity and absorptivity, respectively emissivity. All quantities depend on the radiation wavelength and surface temperature. The camera used in the present study works in the range from 3 to 5 µm.

The absorption of infrared radiation by the sapphire window increases with increasing wavelength and temperature. The absorption can be computed by the extinction coefficient, as described for sapphire by Dobrovinskaya et al. (2009), and the Beer–Lambert law. The absorption drops from almost zero at 3 µm and 500 K, down to 26 % at 5 µm and 500 K.

The reflectivity increases with the temperature but decreases with the wavelength. The reflectivity can be computed by the refraction index at the sapphire-air interface, following Pedrotti et al. (2005). The reflectivity of sapphire at 500 K is in the order of 7 % at $\lambda_{\mathrm{ray}} = 3\,\mu\mathrm{m}$ and $\lambda_{\mathrm{ray}} = 5\,\%$ at 5 µm.

The absorptivity and reflectivity of sapphire affect its transmissivity and, thereby, the accuracy of the temperature measurement. At the same time, the substrate has to withstand a substantial temperature drop due to the cooling by the drop and thermal boundary layer inside the substrate. No other tested material, such as CaF_2 and MgF_2, can withstand such a substantial temperature drop. Sapphire offers the best combination of thermal shock resistance and transmissivity.

Calibration of the Thermal Imaging System

The influence of the transmittance and the unknown emissivity makes the system's calibration mandatory. An in-situ calibration is chosen in the present study. The in-situ calibration allows consideration of the substrate's transmissivity and the coating's emissivity.

The calibration setup is shown in Fig. 2.6. A heated copper block is placed at the coated surface of the substrate for calibration. A type J thermocouple (tolerance class 1) is placed inside the copper block, 0.5 mm away from the copper-sapphire interface. The copper block is thermally isolated to achieve a low temperature gradient inside the copper block.

The copper block and heater of the sapphire window are heated to a certain temperature for the calibration. The thermocouple measures the temperature close to the coating of the sapphire window while the IR camera records the emitted radiation simultaneously. It is assumed that the temperature, measured by the thermocouple, is equal to the temperature of the coating. By this measurement, the recorded infrared radiation can be linked to the temperature of the coating of the substrate. These measurements are repeated in steps of 10 °C in the range of 130 °C to 340 °C.

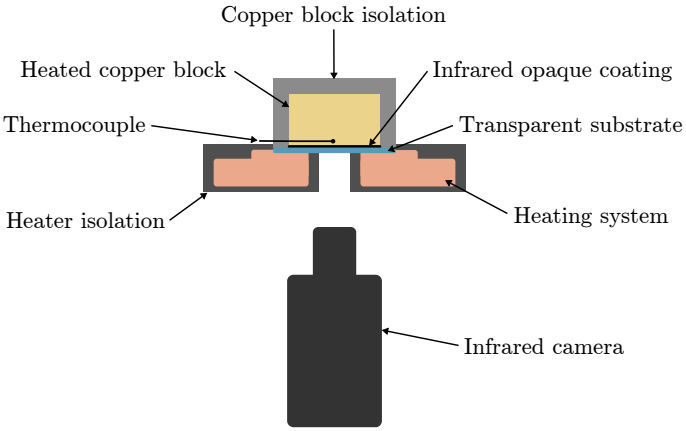

Figure 2.6: Schematic of the setup to calibrate the thermal imaging system. The calibration setup contains the heating system, infrared transparent impact substrate with the infrared opaque coating, and infrared camera. On top of the infrared opaque coating is a heated copper block placed with a thermocouple 0.5 mm above the interface to the coating. All heated parts are isolated.

The calibration shows a good correlation between the recorded radiation and the contact temperature as described by the Stefan-Boltzmann law $M = \sigma_B T^4$. Here, M is the excitance, σ_B is the Stefan-Boltzman constant, and T is the temperature in Kelvin. The calibration is used to compute the two-dimensional temperature distribution of the surface during the experiments.

Heat Flux Estimation

The surface temperature decreases as soon as the drop impacts the substrate. The flow in the spreading drop leads to an intensive heat transfer At the liquid-solid interface. In the drop region, heat is transferred by latent heat, convection, and conduction. In the solid substrate region, it is transferred only by conduction. The temperature evolution is described by the heat equation $\partial T/\partial t = \alpha_w \nabla^2 T$, as given in equation (1.9). The heat equation is solved numerically within a segment of the substrate. The solution allows computations of the temperature gradient and obtains the local heat flux between the impacting drop and the hot surface.

The computational fluid dynamic solver *OpenFOAM* is used for this computation, as described in Fischer et al. (2015). The substrate is discretized as shown in Fig. 2.7. The mesh consists of three regions of different mesh refinements. Close to the liquid-solid interface, the temperature gradient is very steep. Thus, the mesh is refined in this area. The lower parts of the mesh are coarse to increase the computation speed. The boundary condition for the temperature at the upper plane is determined by the measured local temperature at each time step. The lower and side-wall boundaries are assumed to be adiabatic since they are at a large distance from the upper boundary

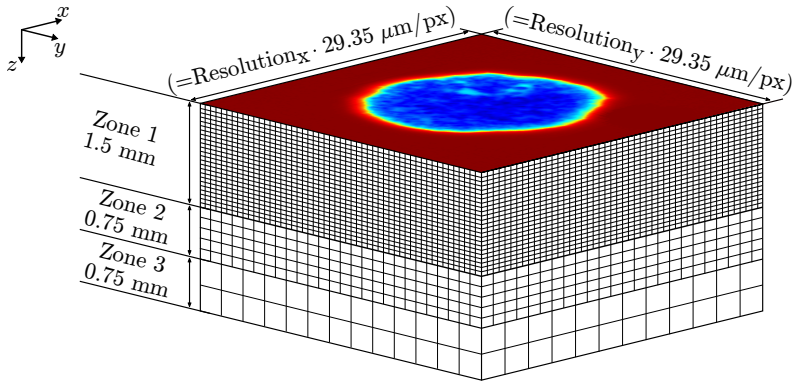

Figure 2.7: Schematic of the computational mesh for the heat flux computation. The mesh is refined towards the upper boundary to account for the steep temperature gradient by the drop impact. The temperature, measured with the infrared camera, is used as a boundary condition at the upper boundary. The side walls and lower boundary are assumed to be adiabatic. Reprint (adapted) from Schmidt et al. (2019), licensed under CC BY 4.0, © 2022 Schmidt et al..

and since the thickness of the substrate is much larger than the thickness of the thermal boundary layer.

3 Transitional Boiling Phenomena during Single Drop Impacts

This chapter focuses on three single drop impact regimes which are determined by transitional boiling effects: Drop dancing in Section 3.1, wet drop rebound in Section 3.2, and thermal atomization in Section 3.3. Parts of the chapter, including text and some figures, are published in Schmidt et al. (2018, 2019, 2021b, 2022, 2023b). Parts of the experimental study are described in the thesis from Hofmann (2019).

Typical phenomena of drop impact onto a substrate at various initial temperatures are illustrated in Fig. 3.1. At low surface temperatures, the drop impacts, deposits at the substrate, and evaporate. The drop deposition and its evaporation may or may not be accompanied by nucleate boiling, depending on the surface temperature. For higher surface temperatures, the nucleate boiling enhances, influencing the liquid flow. The drop starts to hover above the substrate. The observation is reminiscent of a dancing drop or a sticking drop rebound. From a certain threshold temperature on, the drops start to rebound without sticking in the wet rebound regime. Small secondary droplets appear during the wet rebound and small vapor bubbles can be observed after the drop rebounded. At higher impact velocities, the drop impact may lead to thermal atomization. The thermal atomization regime is characterized by many secondary droplets ejected from the spreading lamella. Further, Maranghoni effects and the liquid evaporation close to the rim lead the lamella to levitate. Under some conditions, the rim disintegrated into large secondary drops. Finally, at high surface temperatures, the drop rebounds in the dry rebound regime. No secondary drops or bubbles can be observed anymore. The impacting drop is separated from the substrate by an isolating vapor layer. The regimes drop dancing, wet rebound, and thermal atomization belong to the transitional boiling regime since they are not solely dependent on the steady nucleate boiling within the liquid lamella or stable vapor film, separating the liquid from the substrate.

The temporal evolution of the drop deposition, drop dancing, and wet rebound regime, captured using a high-speed video system, is shown in Fig. 3.2 (a) - (c). All shown drops have a diameter of $d_0 = 2.22\,\mathrm{mm}$ and are impacting with an impact velocity of $u_0 = 0.44\,\mathrm{m\,s^{-1}}$ onto a stainless steel substrate. Three primary outcomes of drop impact accompanied by boiling are shown Fig. 3.2, including drop deposition with complete evaporation (shown in Fig. 3.2 (a)), partial rebound after a certain delay due to a short period of sticking to the substrate, termed drop dancing (shown in Fig. 3.2 (b)), and non-sticking rebound (shown in Fig. 3.2 (c)). The outcome regimes in these examples depend only on the wall superheat $\Delta T_{\mathrm{w},0} = T_{\mathrm{w},0} - T_{\mathrm{sat}}$. Side-view

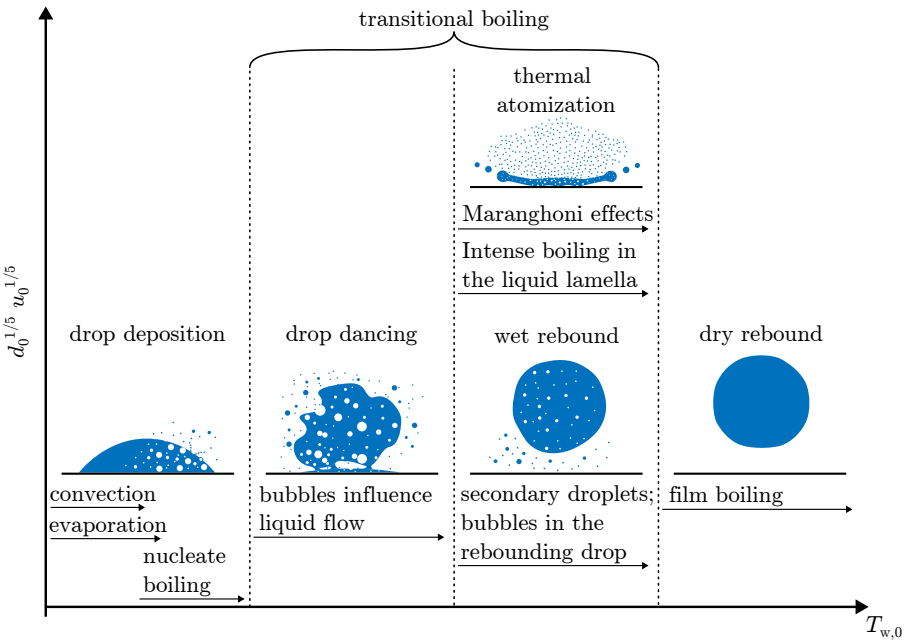

Figure 3.1: Illustration of the drop rebound regimes: drop deposition without and with nucleate boiling, drop rebound caused by film boiling as well as typical regimes associated with the transitional boiling. "drop dancing", wet rebound, and thermal atomization. Reprint (adapted) from Schmidt et al. (2023b), with permission of Elsevier Ltd., © 2023 Elsevier Ltd..

observations of the drop impact outcome allow determining the apparent hydrodynamic regime but cannot always unequivocally indicate a specific microscopic thermodynamic phenomenon at the substrate, for example, nucleate, transitional, or film boiling. Nevertheless, the observations agree with the TIR measurements from Lee et al. (2020). The TIR measurements verified that drops in the drop rebound regime may wet the substrate. X-ray measurements from Lee et al. (2020) showed the appearance of bubbles inside the liquid lamella, which can be observed during later stages in Fig. 3.2 (c).

How long a drop remains at a hot surface depends on multiple factors, such as the drop impact regime and the wall superheat. The residence time t_r of an impacting drop is determined either by the instant of drop rebound or by the duration of complete evaporation of a deposited drop. In Fig. 3.3, the residence times of drop impacts onto an aluminum surface are shown. The residence time t_r of the deposited drops for $\Delta T_{\mathrm{w},0} < 70\,^{\circ}\mathrm{C}$ agrees well with the theoretical predictions of the residence time in the nucleate boiling regime t_{nb}, given in (1.14) from Breitenbach et al. (2017a). In the range of highest wall temperatures ($\Delta T_{\mathrm{w},0} > 110\,^{\circ}\mathrm{C}$) the residence time is very close to the drop capillary time t_σ, given in (1.8), due to the non-sticking drop rebound. In this temperature range, the drop is still in contact with the substrate, as shown in the literature (Lee et al., 2020). However, in the intermediate range of the temperatures ($70\,^{\circ}\mathrm{C} < \Delta T_{\mathrm{w},0} < 110\,^{\circ}\mathrm{C}$), the residence time t_r deviates significantly from both t_{nb} and t_σ. The delay of the drop rebound in this regime is caused by the bonding of the drop at residual wetted spots of the target, as shown for the exemplary drop impacts onto stainless steel at 23.06 ms, 25.23 ms, and 31.13 ms in Fig. 3.2 (b).

The measurements of t_{r} on a stainless steel target are compared to the theoretically predicted times t_{nb} and t_σ in Fig. 3.4. In Fig. 3.4 (a), the single residence times for a specific set of impact parameters are shown. In Fig. 3.4 (b), the residence times of three different impact parameters are shown. The values of t_{r} are averaged for substrate temperature classes for better readability. The residence time agrees well with t_{nb} in the range $\Delta T_{\mathrm{w},0} < 100\,^{\circ}\mathrm{C}$, which is significantly wider than the range observed for aluminum targets (see Fig. 3.3). The residence time is significantly influenced by the thermal properties of the substrate, its initial temperature as well as by the impact parameters. The drop outcome regime in the intermediate temperature range is the drop dancing regime. The drop dancing regime is characterized by the formation of vapor clusters during the spreading and receding of an impacting single drop.

3.1 Drop Dancing by Thermosuperrepellency

In Fig. 3.5, three drop impacts in the drop dancing regime at different surface temperatures are shown. The initial surface temperature increases from the figure's left to the right column. The impacting droplets spread and recede after impact, accompanied by nucleate boiling. The bubbles from the ongoing boiling process begin accumulating, resulting in a larger vapor cluster separating a large volume of liquid from a remaining thin liquid film. The time at which the vapor cluster can be observed for the first

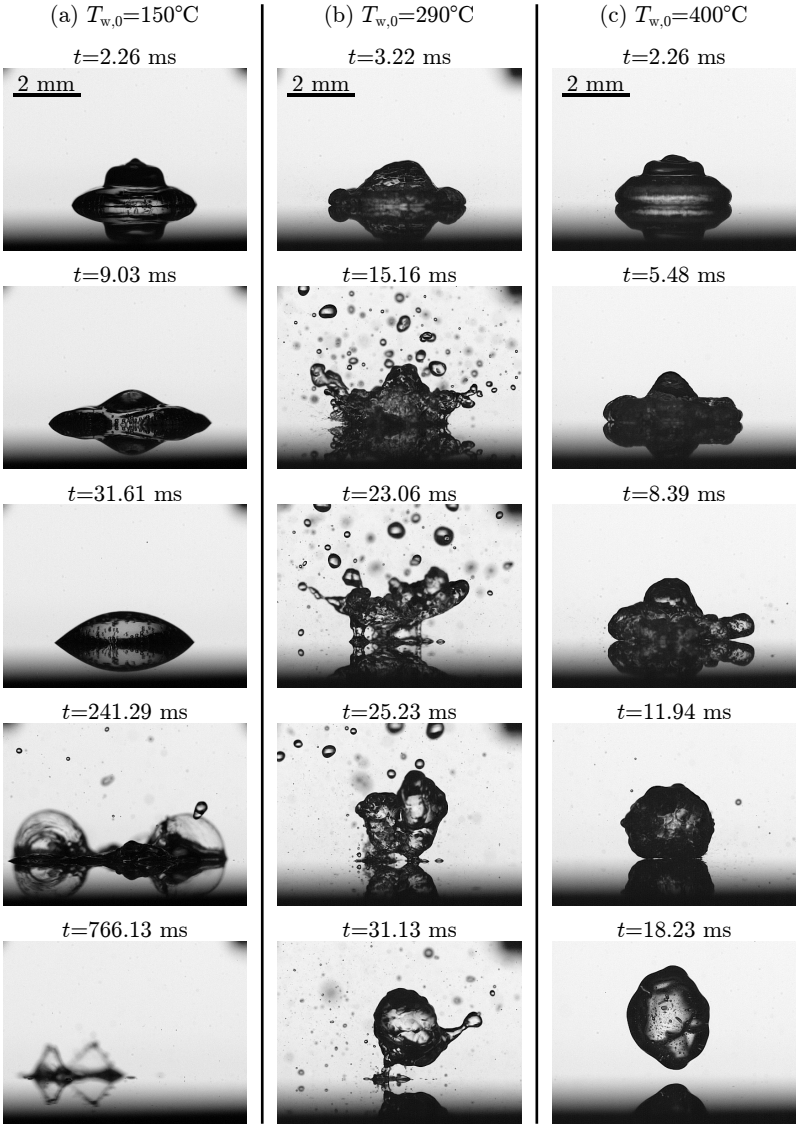

Figure 3.2: Typical stages and primary outcomes of water drop impact onto a hot solid substrate at various initial wall temperatures $T_{w,0}$. The drops have a diameter of $d_0 = 2.22\,\mathrm{mm}$ and are impacting onto a stainless steel substrate with the velocity $u_0 = 0.44\,\mathrm{m\,s^{-1}}$. (a) $T_{w,0} = 150\,^{\circ}\mathrm{C}$: The impacting drop spreads, recedes, and deposits in the nucleate boiling regime. The residence time is determined by complete drop evaporation; (b) $T_{w,0} = 290\,^{\circ}\mathrm{C}$: An intensive nucleate boiling leads to a drop rebound delayed by a short sticking period. The residence time is determined by the evaporation of the liquid residual at the substrate; (c) $T_{w,0} = 400\,^{\circ}\mathrm{C}$: Non-sticking drop rebound. The residence time is determined by the rebound of the drop. The bar in the upper left corner of each column represents a scale of 2 mm. Reprint (adapted) from Schmidt et al. (2023b), with permission of Elsevier Ltd., © 2023 Elsevier Ltd..

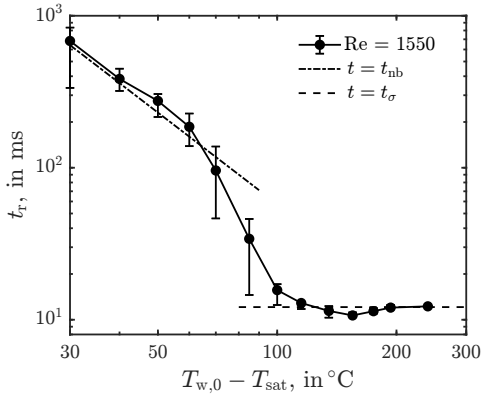

Figure 3.3: Dependence of the average residence time t_r on the wall superheat temperature $T_{w,0} - T_{sat}$ in comparison with the theoretical estimations for the total evaporation time of a deposited drop t_{nb} and the drop natural oscillation time t_σ. The water drops have a diameter of $d_0 = 2.4\,\text{mm}$ and are impacting onto a aluminum substrate with the velocity $u_0 = 0.65\,\text{m}\,\text{s}^{-1}$. Each point is the average value for experimental determined residence times in the corresponding temperature class. The error bars show the minimum and maximum observed residence times during experiments. The experiments have been conducted in the framework of the thesis Breitenbach (2018) and processed in the framework of the present thesis.

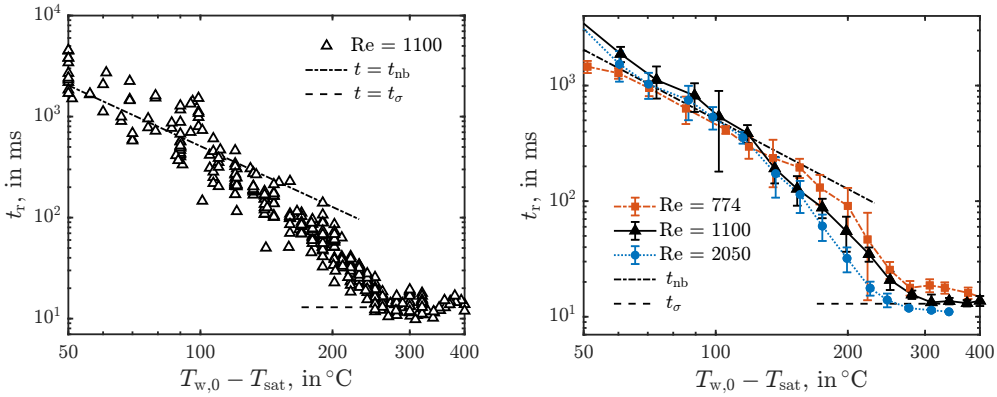

Figure 3.4: Parametric study of the residence time of an impacting water drop on a hot steel target. (a) Experimental results on the residence time t_r of impacting drops with a Reynolds number Re = 1100. Each symbol corresponds to a single drop impact onto a steel target with various initial temperatures. The impact parameters are $d_0 = 2.3\,\text{mm}$ and $u_0 = 0.48\,\text{m}\,\text{s}^{-1}$. The experimental data are compared to theoretical estimations of the total evaporation time of a deposited drop t_{nb} and natural oscillation time t_σ. (b) Residence time t_r averaged over a target temperature class for different impact velocities. Each experimental point is the average value of at least five experiments for the corresponding temperature class. The error bars represent one standard deviation $\pm s$. The experimental residence time is compared to the theoretical models t_{nb} and t_σ.

time is described by the characteristic time t_ϵ. The images in which the cluster is first observed are marked by a black frame in Fig. 3.5. The time t_ϵ decreases with increasing initial surface temperature.

After t_ϵ, the separated volume hovers above the liquid film connected by small liquid bridges and may merge with the remaining liquid film, especially at lower surface temperatures. The observation is reminiscent of a dancing drop, which is why the regime is called drop dancing. The time t_ϵ is not equal to the residence time t_r of the liquid on the substrate. The residence time t_r describes the time when the substrate is completely dry after the initial drop impact. In the last image of each column in Fig. 3.5 is shown the drop at the time instance t_r.

3.1.1 Percolation of Vapor Bubbles

To better understand the mechanisms of the drop dancing regime, it is essential to consider the formation of vapor clusters at the substrate surface. The formation of vapor clusters and subsequent details of the developing vapor phase in the advanced nucleate boiling regime are shown in Fig. 3.6. The images show the temporal evolution of the spreading liquid lamella on a smooth aluminum surface with the temperature of $T_{\mathrm{w},0} = 170\,^\circ\mathrm{C}$. Drop impacts onto a $T_{\mathrm{w},0} = 170\,^\circ\mathrm{C}$ hot aluminum surface lead to delayed drop rebound, as shown in Fig. 3.3. Small perturbations of the spreading lamella by the ongoing nucleate boiling are visible at the first instance of the drop impact in Fig. 3.6. Only a few larger individual bubbles are visible at these stages. The bubbles grow with time, become visible, and intersect, as shown at $t = 2.53\,\mathrm{ms}$. The bubbles further grow during the spreading and receding.

A sticking drop rebound on a sapphire target with a highly emissive IR coating is shown in Fig. 3.7. The images show the spatial distribution of the heat flux at the surface during the impact. The heat flux distribution at $t = 2\,\mathrm{ms}$ shows a high heat flux in the wet areas. Vapor bubbles isolate the liquid from the substrate, lowering heat flux. The small green spots indicate vapor bubbles of the ongoing nucleate boiling. Some of the vapor bubbles intersect, as shown by the arrows. A slightly more extensive cluster of intersecting bubbles is shown on the bottom, marked with an arrow. The heat flux decreases due to the growing thermal boundary layer $\dot{q} \sim 1/\sqrt{\pi t}$. The number and size of the vapor clusters increase with time, as shown at $t = 4\,\mathrm{ms}$. At $t = 6.67\,\mathrm{ms}$, only a small area remains wet. The vapor bubbles in the remaining wet areas lead to a locally higher heat flux at the three-phase contact line. The regions of low heat flux indicate the percolated vapor bubbles, similar to those observed during the spreading and receding in Fig. 3.6. The intersecting vapor bubbles result in larger clusters until only small areas remain wet.

The irregular nucleation of bubbles in the lamella is approximated by randomly distributed disks on a plane. An exemplary illustration of randomly distributed discs on a plane is given in Fig. 3.8. The spatial distribution of disks is characterized by the cumulative relative area λ of the disks, scaled by the total domain area, also

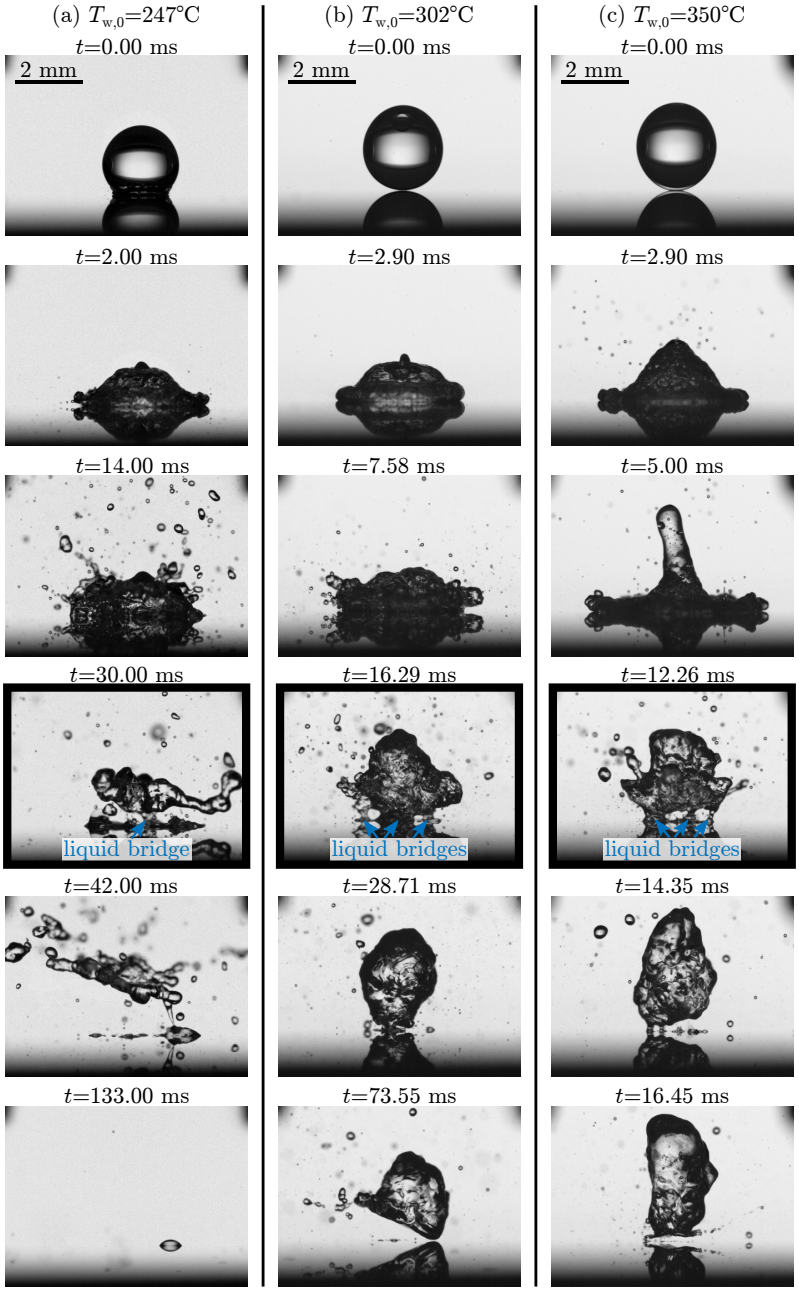

Figure 3.5: Exemplary water drop impacts in the drop dancing regime at initial surface temperatures $T_{w,0}$ from 247 °C (left column) to 350 °C (right column). The time t_ϵ, from which the most liquid levitates, is marked by a black frame. The last image of each column shows the residence time t_r, after which the initial drop impact no longer wets the substrate. The bar in the upper left corner of each column represents a scale of 2 mm. Reprint (adapted) from Schmidt et al. (2023b), with permission of Elsevier Ltd., © 2023 Elsevier Ltd..

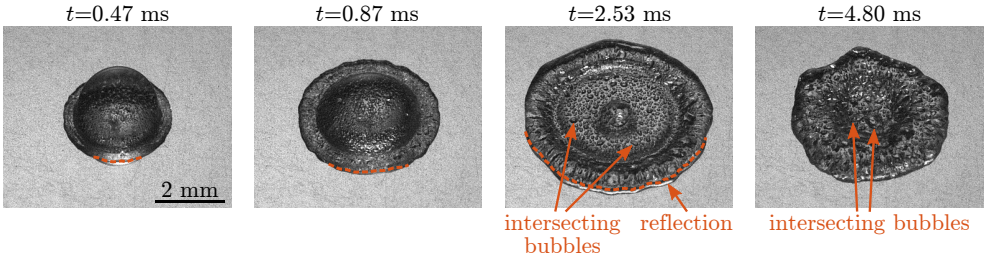

Figure 3.6: Top-view observations of a spreading and receding drop on a polished aluminum substrate. Drop impacts at an initial substrate temperature $T_{w,0} = 170\,^{\circ}\mathrm{C}$ in the sticking rebound regime, captured by the high-speed video system from the top. Bubbles are the result of the heterogeneous nucleation at the substrate. The bubbles start to intersect during the receding phase of the drop. The dashed line separates the direct view of the drop and the reflection of the drop. The bar in the left image shows a scale of 2 mm. The experiments have been conducted in the framework of the thesis Breitenbach (2018).

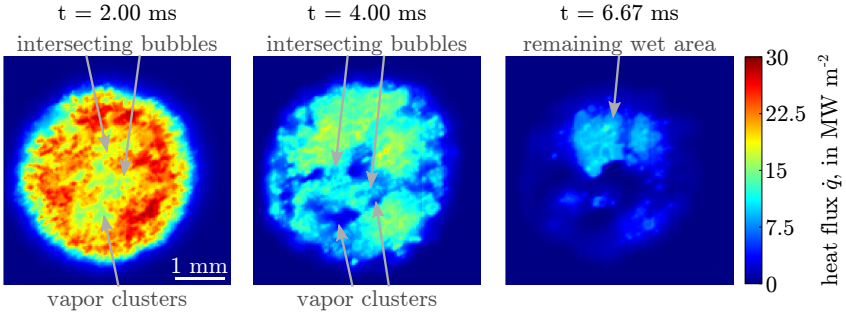

Figure 3.7: Heat flux maps, computed by the temperature distributions captured with the high-speed IR camera during a drop impact onto a sapphire target at $T_{w,0} = 291\,^{\circ}\mathrm{C}$. The drop impact belongs to the drop dancing regime. The regions with a high heat flux correspond to the wet areas, while the low heat flux areas show vapor bubbles and clusters. The distributions show intersecting vapor bubbles leading to larger vapor clusters until only a small area remains wet. The bar in the left image shows a scale of 1 mm.

called filling factor. Some of the disks intersect and thus form clusters of discs. The distribution of the cluster sizes is studied in the framework of the percolation theory. The percolation threshold in this two-dimensional problem is $\lambda_c = 1.128$ (Mertens & Moore, 2012). At this point, an infinite cluster of the intersecting disks appears first, as shown in Fig. 3.8 (c). The formation of the wrapping cluster of the disks at the percolation threshold can explain the percolation of vapor bubbles and the formation of vapor clusters, as shown in Fig. 3.7. At the percolation threshold, the liquid wets the substrate only at isolated spots. This situation is analogous to the Cassie-Baxter wetting of heterogeneous substrates, associated with superhydrophobicity and super repellency (Quéré, 2005) in conventional isothermal cases. This is why the effect is referred to as thermosuperrepellency.

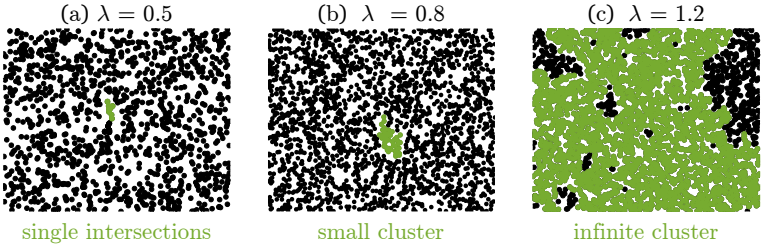

Figure 3.8: Visualization of intersecting discs with different ratios λ of cumulative disc areas, scaled by the total area of the domain. With increasing cumulative area, the intersection probability increases. Each disk represents a simplified nucleation bubble. Above the percolation threshold $\lambda_c = 1.128$, the bubbles wrap to large clusters.

The computed value $\lambda_c = 1.128$ is a rough approximation for the percolation threshold for the vapor bubbles since the percolation theory does not consider bubble coalescence or shear driven motion of the bubbles in the liquid flow. The relative wetted surface area (not belonging to the surface covered by the bubbles) is ϵ. The value of ϵ is derived using the Poisson distribution for the expected number of bubbles covering a given point of the surface (Feller, 1971), assuming a random spatial distribution of bubble centers. At the percolation threshold, it yields

$$\epsilon_c = \exp(-\lambda_c) \approx 0.32, \tag{3.1}$$

describing the critical wetted area from which on vapor bubbles intersect, leading to infinite vapor clusters.

3.1.2 Heat Transfer in the Drop Dancing Regime

The heat transfer between the the solid and liquid is determined by a strong nucleate boiling in the early stages of the drop impact. The liquid flow in the drop changes entirely as soon as vapor clusters appear, and the relative volume of the liquid phase drops below the critical value $\epsilon < \epsilon_c$. From then on, the liquid contacts the substrate only at isolated wetted spots, which cannot prevent drop rebound or drop dancing.

The heat flux $\dot{q}$ at the liquid-solid interface is governed by the heat conduction in the solid $\dot{q} = (e_\mathrm{w}\Delta T_{\mathrm{w},0})/(\sqrt{\pi t})$, as given in equation (1.13). The heat transfer from the substrate to the liquid lamella $\dot{q}$ results in the evaporation of the liquid phase. It can be estimated from the one-dimensional energy balance accounting for the creation of the vapor phase, expressed as

$$\rho_\mathrm{l} h_\mathrm{res} L^* \epsilon'(t) = -\dot{q}, \tag{3.2}$$

where ϵ is the relative wetted area of the liquid phase in the lamella, and h_res is the resulting lamella thickness. The lamella thickness of the spreading drop can be considered by $h_\mathrm{res} \approx 0.79\, d_0\, \mathrm{Re}^{-2/5}$, as described in equation (1.2) by Roisman (2009).

Expression (1.13) allows to predict the heat flux during spray cooling in the nucleate boiling regime in a wide range of spray parameters and wall temperatures (Tenzer et al., 2019). Therefore, the presence of bubbles does not influence the value of $\dot{q}$ significantly. In a steady heat conduction in the wall, bubbles lead to local disturbances of the temperature field. Nevertheless, the total heat flux at the interface remains the same due to the energy balance. The heat flux can only be changed if transient effects associated with bubble growth are significant (Staszel & Yarin, 2018). The wall region's size, disturbed by a bubble's presence, is comparable with the bubble radius. Therefore, the contribution of the bubbles presence at the substrate surface is negligible if the bubble size is much smaller than the thickness of the thermal boundary layer in the wall. This condition is satisfied in the present experiments.

The solution of the ordinary differential equation in equation (3.2), together with the expression of the heat flux in the solid (1.13), is

$$\epsilon(t) = 1 - \frac{1.43 e_\mathrm{w} \Delta T_{\mathrm{w},0} \mathrm{Re}^{2/5} t^{1/2}}{\rho d_0 L^*}. \tag{3.3}$$

The duration until a large amount of liquid rebounds due to the percolation of vapor bubbles can be expressed with the help of equation (3.1) in the form

$$t_\epsilon = \frac{1}{k_\epsilon} \left[\frac{(1-\epsilon_\mathrm{c})\rho_\mathrm{l} d_0 L^*}{e_\mathrm{w} \Delta T_{\mathrm{w},0} \mathrm{Re}^{2/5}} \right]^2, \tag{3.4}$$

with k_ϵ being an empirical factor in the order of unity. The time of percolation t_ϵ describes the beginning of the drop dancing, as most of the liquid is only connected to a thin layer of liquid on the substrate by small separated wetted areas or liquid bridges.

The experimentally determined times of t_ϵ are compared with the theoretically predicted times in Fig. 3.9. Each triangle in (a) represents an experimentally determined value from a drop impact onto a smooth stainless steel substrate with a Reynolds number of approximately 1200. The experimental values are in good agreement with the theoretical predictions. The factor k_ϵ in equation (3.4) is set to 1.3 by fitting to the experimental data. This is close to the theoretical factor 1.43 from equation (3.3). The scatter in the experimental data is caused by the spatially and temporally chaotic

appearance and coalescence of bubbles in the liquid film, leading to percolation. From a certain threshold temperature ΔT^* onward, the times remain constant and scale with $(\pi/4)\, t_\sigma$ as Castanet et al. (2015) described.

The percolation time t_ϵ for different Reynolds numbers is shown in Fig. 3.9 (b). While symbols of different colors mark the experimental data, the dashed lines show the corresponding theoretical predictions of equation (3.4). The factor k_ϵ is again 1.3 for all shown data sets. The experimental data of all three Reynolds numbers 791, 1157, and 2032 agree well with the theoretical predictions until ΔT^* is reached. At higher wall superheat, the experimentally determined rebound times are about $(\pi/4)\, t_\sigma$ (Castanet et al., 2015).

The experimental percolation time t_ϵ settles between 30 ms and 40 ms for lower wall superheat than those shown in Fig. 3.9 (b). In addition, the observed large vapor cluster becomes more challenging to identify because the impact is accompanied by intense nucleate boiling with large bubbles.

The heat Q_{dd} removed by a drop in the drop dancing regime can be determined from the heat flux $\dot{q}$ during a drop impact, the wetted area $A_{\mathrm{wet}} = \pi r_{\mathrm{s}}^2$, and the contact time. The contact time can be assumed to be t_ϵ since most liquid detaches or hovers

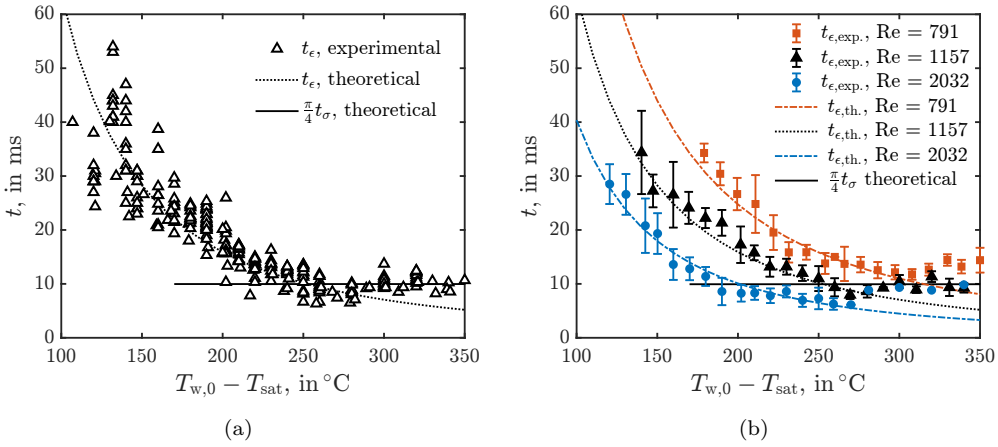

Figure 3.9: Comparison of experimental data with the theoretical prediction of expression (3.4). The factor k_ϵ in equation (3.4) is set to 1.3, which is close to the theoretical 1.43. (a) The experimental data are shown as triangles. The average Reynolds number of the experiments shown is 1157. At temperatures above 250 °C, the rebound time follows the time of natural drop oscillations as described in Castanet et al. (2015). (b) Comparison of the theoretical model given in equation (3.4) and experimental data for different Reynolds numbers. The colored symbols represent the mean values of the experimental data sets. The bars on the symbols show the standard deviation of the measured values of t_ϵ. The average Reynolds numbers of the experimental data sets are 791, 1157, and 2032. The corresponding theoretical predictions are given by the dashed line in the same color as the symbol. Reprint (adapted) from Schmidt et al. (2023b), with permission of Elsevier Ltd., .

above the surface after t_ϵ and does not participate in the evaporation process at the wetted surface. The heat Q_{dd} can be determined in the form

$$Q_{\mathrm{dd}} = \int_0^{t_\epsilon} \dot{q}(t)\pi r_{\mathrm{s}}(t)^2 \,\mathrm{d}t. \tag{3.5}$$

Inserting the heat flux, given in equation (1.13), leads to

$$Q_{\mathrm{dd}} = \int_0^{t_\epsilon} \frac{e_{\mathrm{w}}\Delta T_{\mathrm{w},0}}{\sqrt{\pi t}}\pi r_{\mathrm{s}}(t)^2 \,\mathrm{d}t \tag{3.6}$$

for the heat removed by a single drop. The expression allows to predict the heat removed by a single drop. The prediction is also particularly useful for predicting the heat flux in spray cooling. In this case, the density of the spray and, thus, the probability of droplet interaction must be considered.

3.2 Wet Drop Rebound by Thermosuperrepellency

The sticking drop rebound, shown in the previous section, appears at temperatures below the threshold temperature ΔT^*. Drop impacts at temperatures above the threshold temperature ΔT^* result in a non-sticking drop rebound. Side-view observations of a sticking drop rebound are shown in Fig. 3.2 (b) and of a non-sticking drop rebound in Fig. 3.2 (c).

3.2.1 Wetting Phenomena during Drop Rebound

Top-view observations of a non-sticking drop rebound are shown in Fig. 3.10. In the figure is shown a drop impact onto a 200 °C smooth aluminum surface. In the images, lighter and darker areas are visible inside the liquid, as already observed for the sticking drop rebound in Fig. 3.6. The darker areas represent wetted areas. In comparison, brighter areas indicate vapor bubbles or clusters. The vapor clusters appear already during the spreading of the drop, as shown at $t = 1.33\,\mathrm{ms}$. A dashed line marks the difference between the liquid lamella and its reflection. The reflection of the lamella rim is only visible at high contact angles between the liquid and the substrate. High contact angles typically appear during spreading and close to the maximum spreading diameter on polished aluminum substrates. The receding contact angle in the drop deposition and drop dancing regime is low and suppresses the reflections from the lamella rim, as shown in Fig. 3.6. The reflections in the present case are also visible during later stages, as shown at $t = 4.67\,\mathrm{ms}$. This indicates a high contact angle and low wettability during the drop receding.

A non-sticking drop rebound on a sapphire target with a highly emissive IR coating is shown in Fig. 3.11. The images show the spatial distribution of the heat flux at the liquid-solid interface during the impact. The heat flux distribution at $t = 2\,\mathrm{ms}$ shows a high heat flux and a mainly wet substrate, indicated by the red areas. Large vapor

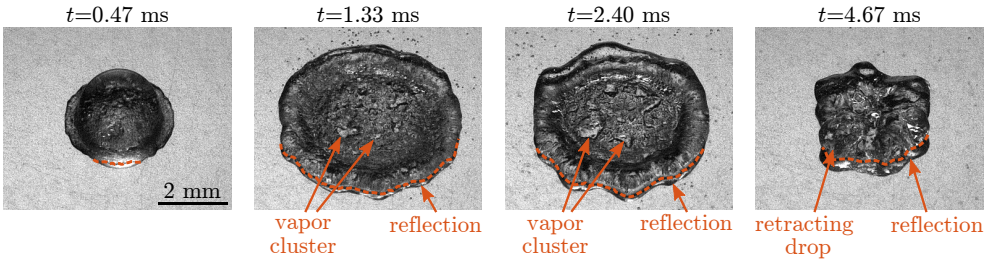

Figure 3.10: Top-view observations of a spreading and receding drop on a polished aluminum substrate. Drop impacts at an initial substrate temperature $T_{w,0} = 200\,°C$ in the non-sticking rebound regime, captured by the high-speed video system from the top. Bubbles in the lamella intersect during the spreading phase, leading to vapor clusters and, finally, the non-sticking drop rebound. The dashed line separates the direct view of the drop and the reflection of the drop. The bar in the left image shows a scale of 2 mm. The experiments have been conducted in the framework of the thesis Breitenbach (2018).

clusters can already be observed at $t = 4.00\,ms$, indicated by the blue areas with a low heat flux. Subsequently, only small areas remain wet while the remaining lamella levitates above the hot surface. The vapor layer isolates the liquid from the substrate, lowering the heat flux significantly. The fluid fully detaches from the substrate before the drop rebounds.

The top-view observations and heat flux evolution reveal that the drops are in contact with the substrate during the spreading and receding. Moreover, the observations reveal that the identical mechanism of vapor percolation is present for sticking and non-sticking drop rebounds. Both drop impact regimes are determined by the wetting of the substrate and, subsequently, percolation of the vapor bubbles in the liquid film.

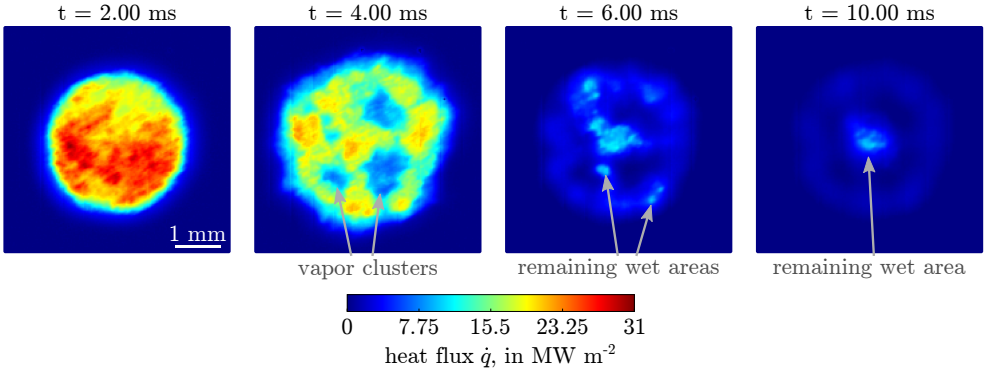

Figure 3.11: Heat flux maps, computed by the temperature distributions captured with the high-speed IR camera during drop impact onto a sapphire target with $T_{w,0} = 362\,°C$. The drop rebounds while wetting the substrate. The regions with a high heat flux correspond to the wet areas, while the low heat flux areas show vapor bubbles and clusters. After the initial wetting, vapor clusters appear. The clusters grow until finally, only a small area remains wet. The liquid detaches before the drop rebound time t_σ is reached.

3.2.2 Thermosuperrepellency Temperature

The heat transfer in the wet rebound regime can be estimated from the one-dimensional energy balance $\dot{q} = -\rho_\mathrm{l} h_\mathrm{res} L^* \epsilon'(t)$, as introduced in equation (3.2). The solution of the ordinary differential equation leads to the time t_ϵ, given in equation (3.4), from which the bubble percolation causes infinite vapor clusters.

The percolation of vapor bubbles leads to infinite vapor clusters for the already receded liquid lamella in the drop dancing regime. In the case of the non-sticking drop rebound or wet drop rebound, infinite clusters appear during the spreading and receding of the drop. In Fig. 3.4, it is already shown that the residence time t_r of the drops stay constant in the order of the natural drop oscillation time $t_\sigma = \sqrt{\rho_\mathrm{l} d_0^3/\sigma}$ for temperatures above the threshold temperature ΔT^*. This is valid for surface tension dominated drop impacts when $\mathrm{We} \ll 2.5\,\mathrm{Re}^{2/5}$. The factor 2.5 is empirical, determined from numerous experiments. The agreement is good, considering that the substrate materials, impact velocities, drop diameters, and liquids vary widely. For very high Weber numbers, the duration of drop spreading is scaled by the viscous time scale $t_\nu = d_0 \mathrm{Re}^{1/5}/u_0$, as given in equation (1.3) by Roisman (2009). The time t_ν describes the time at which the lamella thickness and the thickness of the viscous boundary layer are equal. The viscous spreading regime is essential for fast-impacting, small drops, as in spray cooling.

The single drop impacts of the present work are in the surface tension dominated regime. The drops rebound without sticking if $t_\epsilon < t_\sigma$, which yields the expression for the threshold overheat

$$\Delta T = b\,\Delta T_\sigma, \quad \Delta T_\sigma = \frac{d_0^{1/4} L^* \rho^{3/4} \sigma^{1/4}}{e_\mathrm{w} \mathrm{Re}^{2/5}}, \tag{3.7}$$

where $b = 0.848$ and ΔT_σ is a typical scale for the superheat threshold in the surface tension dominated drop impact regime. Coefficient b includes the coefficient k_ϵ and is determined by fitting the experimental data with the theory.

It should be noted that the coefficient b can be influenced by the reduction of the wetted area of the drop due to the appearance of dry spots, the liquid flow in the lamella, drop atomization, and other factors. Therefore, the solution equation (3.7) is not exact. However, it is essential that the factor b in equation (3.7) has to be comparable with unity if the significant physical factors are taken into account correctly.

In the estimation of heat transfer, given in equation (3.2), the relative wetted surface area ϵ is approximated by the liquid fraction, and the residual thickness h_res is assumed to be constant. This assumption cannot be very precise if the height of the vapor bubbles/channels changes in time, for example, due to the evaporation of the drop lamella. The analysis is valid for the cases when $t_\sigma \ll t_{\epsilon,\mathrm{drop}}$. This condition is satisfied for drop impacts at the threshold temperature. The recent direct observations of the relative liquid contact area in Lee et al. (2020) can potentially help to determine the relation to the volume fraction. These data could be a topic of interesting future investigations.

In Fig. 3.12, the theoretically predicted scales for the threshold temperature ΔT_σ of expression (3.7) are compared with experimentally determined threshold temperatures ΔT^*. The drop impact experiments of the present study represent different impact substrates (stainless steel, aluminum, and copper) and drop impact velocities. The data from the literature are given in Table 3.1. The data are taken from regime maps provided by Wang et al. (2020b), and Bertola (2015), and the evaporation time dependence on the surface temperature in Chandra & Avedisian (1991). The data from the regime maps represent the threshold temperature, from which on drop rebounds with secondary atomization are observed. All experimental data in Fig. 3.12 represent low speed impacts with $\mathrm{We} \ll 2.5\,\mathrm{Re}^{2/5}$, governed by surface tension.

The results demonstrate that the transition to the film boiling regime is initiated at the threshold point for vapor percolation. Subsequent drop evaporation is governed by vapor rivulets and is characterized by the disappearance of isolated wet spots. The film boiling regime corresponds to a complete vanishing of the wet spots.

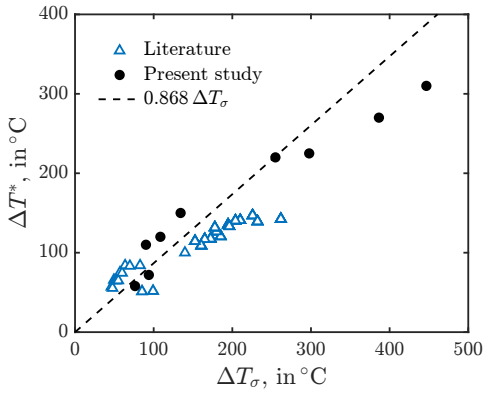

Figure 3.12: Comparison of the experimental determined threshold overheat temperatures ΔT^*, with the theoretically predicted scale of the threshold overheat ΔT_σ. Experimentally determined results of the present study and data from literature are compared to the theory, given in expression (3.7). Each experimental threshold temperature of the present study is determined by a series of single drop experiments with constant impact parameters. The experimental threshold overheat $\Delta T^* = T^* - T_{\mathrm{sat}}$ is the threshold temperature above which the residence time t_r is constant and single drops rebound. The experiments are performed on different substrate materials and impact velocities. The experimental results from the literature are taken from Chandra & Avedisian (1991), Wang et al. (2020b), and Bertola (2015), including data for different liquids, substrate materials, and impact parameters. The data are also given in Table 3.1.

3.3 Wetting in the Thermal Atomization Regime

Drop impacts above the threshold temperature ΔT^* and high impact velocities lead to an atomization of the drop instead of a rebound. The atomization is characterized by

Study	Substrate material	Liquid	Re	ΔT^*, in °C
Present study	Stainless steel	Water	779	310
Present study	Stainless steel	Water	1090	270
Present study	Stainless steel	Water	2068	225
Present study	Stainless steel	Water	3081	220
Present study	Aluminum	Water	946	150
Present study	Aluminum	Water	1576	120
Present study	Aluminum	Water	2516	110
Present study	Copper	Water	872	72
Present study	Copper	Water	1482	58
Chandra & Avedisian (1991)	Stainless steel	Heptane	2300	200
Wang et al. (2020b)	FeCrAl	Water	6078	239
Wang et al. (2020b)	FeCrAl	Water	9248	233
Wang et al. (2020b)	FeCrAl	Water	11 829	231
Wang et al. (2020b)	FeCrAl	Water	12 765	218
Wang et al. (2020b)	FeCrAl	Water	14 271	217
Wang et al. (2020b)	FeCrAl	Water	15 273	209
Wang et al. (2020b)	FeCrAl	Water	17 337	214
Wang et al. (2020b)	SiC	Water	6464	152
Wang et al. (2020b)	SiC	Water	9454	151
Wang et al. (2020b)	Zr4	Water	6599	242
Wang et al. (2020b)	Zr4	Water	9548	247
Wang et al. (2020b)	Zr4	Water	11 430	241
Wang et al. (2020b)	Zr4	Water	12 305	240
Wang et al. (2020b)	Zr4	Water	13 845	235
Wang et al. (2020b)	Zr4	Water	15 664	221
Wang et al. (2020b)	Zr4	Water	16 855	227
Bertola (2015)	Aluminum	Water	3287	184
Bertola (2015)	Aluminum	Water	5032	183
Bertola (2015)	Aluminum	Water	6315	184
Bertola (2015)	Aluminum	Water	7382	175
Bertola (2015)	Aluminum	Water	8270	175
Bertola (2015)	Aluminum	Water	9108	165
Bertola (2015)	Aluminum	Water	9946	165
Bertola (2015)	Aluminum	Water	10 587	165
Bertola (2015)	Aluminum	Water	11 269	165
Bertola (2015)	Aluminum	Water	13 062	166
Bertola (2015)	Aluminum	Water	14 102	155
Bertola (2015)	Aluminum	Water	15 097	157

Table 3.1: Overview of the reference, substrate material, liquid, Reynolds number, and rebound temperature, as used in Fig. 3.12.

a fine secondary spray ejected from the spreading lamella. The atomization is most likely driven by the wetting of the substrate during the early stages of the drop impact, as described in Sec. 1.2.2. A two dimensional heat flux model is introduced in the following section.

3.3.1 Phenomenology of the Thermal Atomization

Side-view observations of a drop impact in the thermal atomization regime are shown in Fig. 3.13. The drop impacts onto a smooth sapphire window coated with CrN. The initial wall temperature is $T_{w,0} = 345\,°C$, the drop diameter is $d_0 = 2.21\,mm$, and the impact velocity is $u_0 = 1.15\,m\,s^{-1}$. As soon as the drop impacts, a thin lamella develops. An intensive nucleate boiling appears within the spreading lamella. Strong ongoing nucleate boiling leads to a fine secondary spray, ejected from the liquid lamella beginning from $t = 0.78\,ms$. The lamella levitates from $t = 3.45\,ms$ on, beginning from the rim. No secondary droplets are ejected anymore from the levitating lamella. The side-view observations cannot reveal the contact radius of the lamella with the surface. The optical resolution limits the ability to observe vapor gaps smaller than $20\,\mu m$, as described in Chapter 2. Moreover, the lamella rim may cover the levitation of the lamella slightly. At $t = 4.78\,ms$, almost the entire lamella levitates. In the figure, it can be seen that instabilities develop in the lamella rim at $t = 3.45\,ms$. The instabilities finally lead to the disintegration of the rim into large secondary droplets, as shown at $t = 4.78\,ms$. The time until the drop disintegrates is short compared to other drop impact regimes. The lamella and entire drop disintegrate before the spreading of the lamella stops.

The corresponding temperature distributions during the drop impact are shown in Fig. 3.14. The initial wetting powerfully cools the wall. The temperature distributions show a substantial temperature drop in the area of the lamella. The temperature drop is slightly lower at the center and at the edge. The cooled area increases radially until $t = 1.37\,ms$ due to the drop spreading at the substrate. Between $t = 1.37\,ms$ and $t = 2.04\,ms$, the cooled area no longer significantly increases. This apparently seems not to match the observations made in Fig. 3.13. While the lamella spreads further, the cooled area stays more or less constant. But, the constant area is caused by the levitation of the lamella, beginning from the rim. The vapor layer between the levitated lamella and substrate isolates and reduces the cooling. A few small areas are slightly cooled down outside the strongly cooled area. These areas are marked in Fig. 3.14 with white arrows. The cooling of these areas is caused by the liquid accumulations due to the rim instabilities and beginning fingering. The liquid accumulations reduce the local vapor layer, slightly enhancing the local heat transfer. The wall temperature increases again from $t = 1.37\,ms$, and the cooled area decreases.

The computed local heat flux at different times instances is shown in Fig. 3.15. The highest heat flux appears during the initial wetting of the substrate at $t = 0.05\,ms$ and $t = 0.71\,ms$. The wetting results in a sudden temperature drop at the liquid-solid

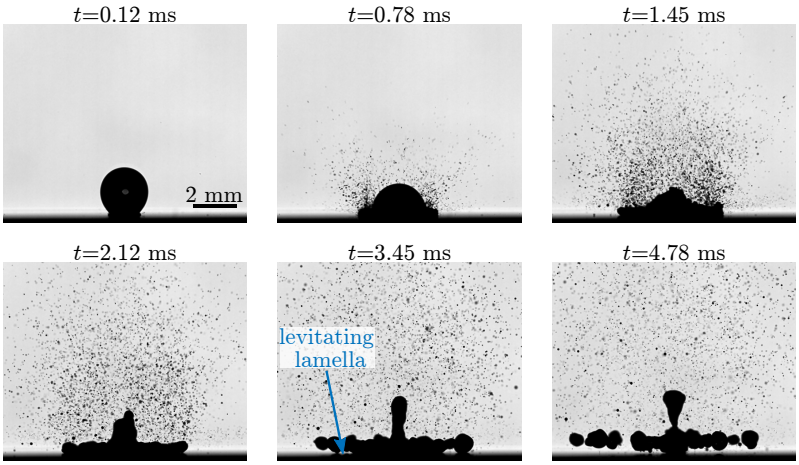

Figure 3.13: Side-view observations of a drop impact in the thermal atomization regime. The lamella spreading, generation of fine secondary spray, and lamella levitation are shown within the time series of images. The boundary conditions are smooth sapphire window as impact target, initial wall temperature $T_{w,0} = 345\,°C$, drop diameter $d_0 = 2.21\,mm$, and impact velocity $u_0 = 1.15\,m\,s^{-1}$. The black bar in the upper left image represents the scale of 2 mm.

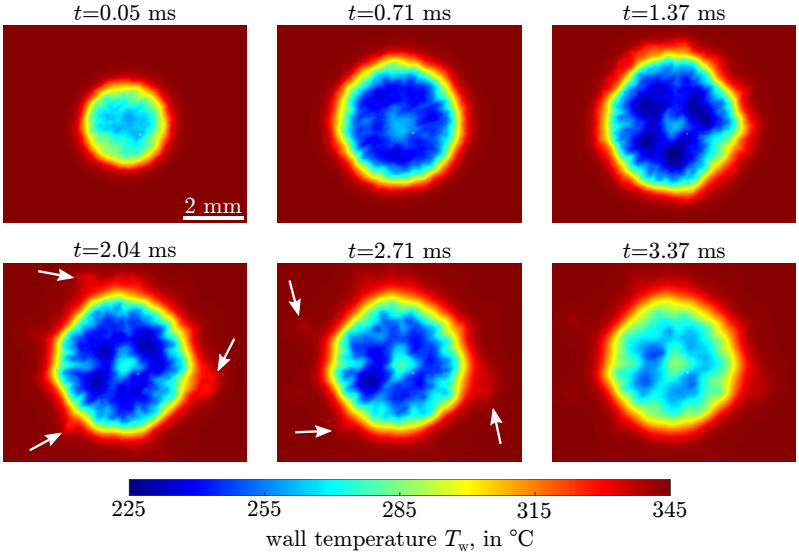

Figure 3.14: Surface temperature distribution at different times during a drop impact in the thermal atomization regime. The sapphire substrate has an initial surface temperature of 345 °C. The drop impacts with an impact velocity of $1.15\,m\,s^{-1}$. The white arrows show slightly cooled areas by the rim instabilities. The white bar in the upper left image represents 2 mm.

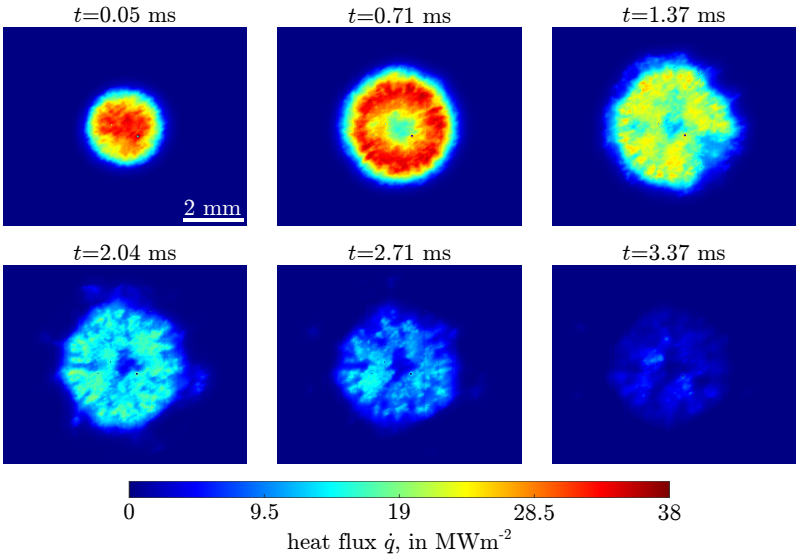

Figure 3.15: The heat flux distributions at different times after the impact of a drop in the thermal atomization regime are shown in this figure. The initial surface temperature of the substrate is 345 °C. The drop impacts with an impact velocity of $1.15\,\mathrm{m\,s^{-1}}$. The highest heat flux appears in the first two time instances. The intensively cooled area does not spread further after $t = 2.04\,\mathrm{ms}$. The white bar in the upper left image represents 2 mm. Reprint (adapted) from Schmidt et al. (2019), licensed under CC BY 4.0, ©2022 Schmidt et al..

interface and a steep temperature gradient close to the interface in the substrate. From $t = 1.37\,\mathrm{ms}$ on, the heat flux decreases due to the flattening temperature gradient close to the substrate. The cooled area does not further propagate at the same time, indicating the starting lamella's levitation at the rim. The vapor layer between the liquid and the substrate reduces the heat flux. After 2.04 ms, the high heat flux area decreases while the drop spreads, as shown in the side-view observations.

3.3.2 Evaluation of Wetting in the Thermal Atomization Regime

As a result of the droplet impact, a thin lamella is formed, with the thickness $h_{\mathrm{lamella}} \sim t^{-2}$, as shown in Yarin & Weiss (1995). Immediately after the impact, a viscous boundary layer grows in the substrate with $\delta_\nu \sim \sqrt{\nu_\mathrm{l} t}$, as described in Section 1.2. At the same time, a thermal boundary layer grows inside the liquid and the substrate since the initial wall temperature $T_{\mathrm{w},0}$ differs from the initial drop temperature $T_{\mathrm{d},0}$. The temperature at the liquid-solid interface is assumed to be the liquid saturation temperature T_{sat} since the liquid and solid are in direct contact while the substrate is wetted. The contact radius until the liquid and substrate are in contact is defined as r_s. The heat flux in the solid substrate can be described by the equation of heat in a

cylindrical coordinate system in the form of

$$\frac{\partial T}{\partial t} - \frac{1}{r}\frac{\partial}{\partial r}\left(\alpha_{\mathrm{w}} r \frac{\partial T}{\partial r}\right) - \frac{\partial^2 T}{\partial z^2} = 0. \tag{3.8}$$

The tangential heat conduction is neglected since the fluid flow is assumed to be symmetrical. The thermal boundary layer in the liquid and solid grows with $\delta_{\mathrm{t}} \sim \sqrt{\alpha t}$. The flow in the lamella suppresses the thermal boundary layer, which results in a heat flux compared to a non-moving liquid (Batzdorf et al., 2017). The problem and definition of the coordinate system are shown schematically in Fig. 3.16.

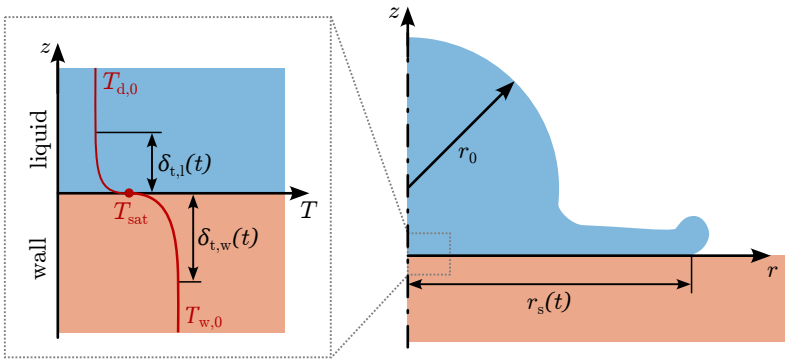

Figure 3.16: Sketch of the drop impact in the thermal atomization regime. The coordinate system, initial drop radius r_0, and wetting radius $r_{\mathrm{s}}(t)$ are shown on the right-hand side. The growing thermal boundary layer in the liquid $\delta_{\mathrm{t,l}}$ and wall material $\delta_{\mathrm{t,w}}$ are shown on the left side.

In Roisman (2009, 2010) a similarity solution is obtained for the fluid flow and heat transfer after the impact of a droplet on a dry solid wall. The solution describes the velocity and temperature distribution in the expanding lamella and the temperature distribution in the wall, including regions near the fluid-solid interface. The similarity solution is based on the mass balance, axial momentum balance, and energy balance equations. The heat flux in the substrate at the interface $z = 0$ is described in the form

$$\dot{q}(r,t) = \frac{e_{\mathrm{l}} e_{\mathrm{w}} (T_{\mathrm{w},0} - T_{\mathrm{d},0})}{(e_{\mathrm{l}} + e_{\mathrm{w}} \mathscr{I}(\mathrm{Pr}))\sqrt{\pi t}\sqrt{1-\bar{r}^2}}, \tag{3.9}$$

in which $\mathscr{I}(\mathrm{Pr})$ is a dimensionless function of the Prandtl number of the liquid $\mathrm{Pr} = \nu_{\mathrm{l}}\,\alpha_{\mathrm{l}}$, as described in Section 1.2. The variable $\bar{r}$ is the dimensionless radius

$$\bar{r} = r/r_{\mathrm{s}}(t), \quad r_{\mathrm{s}}(t) \approx \sqrt{d_0 u_0 t}. \tag{3.10}$$

The function $\mathscr{I}(\mathrm{Pr})$ is introduced in Section 1.2. The function is shown in Fig. 1.4. When the Prandtl number is very high, $Pr \gg 1$, the impact of the flow becomes insignificant. In such a scenario, expression (3.9) represents the heat conduction

between two infinite solid bodies. For very low Prandtl numbers, the numerical solution tends to approach an asymptotic solution provided by Roisman (2010), as described in Section 1.2.

In Fig. 3.17, the theoretical model of equation (3.9) is compared with the experimental data shown in Fig. 3.15 for $r = 0$. The model has a singularity at $t = 0$. The theoretical model exhibits good agreement with the experimental data. After 3.5 ms, the liquid lamella levitates, and the boundary condition and model are no longer valid.

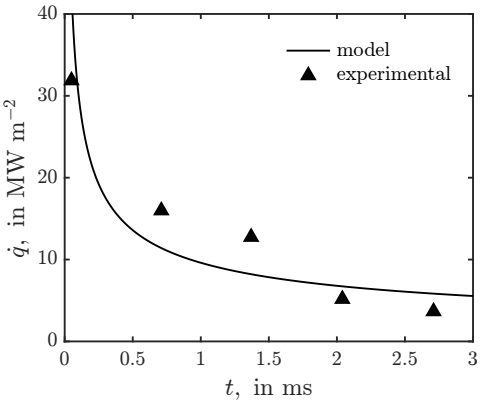

Figure 3.17: Heat flux of a drop impact in the thermal atomization regime. The drop impact velocity of the shown experiment is 1.15 m s^{-1}, and the surface temperature is 345 °C. The solid line represents the theoretical model of equation (3.9) in the center of the lamella ($r = 0$) as a function of time. The triangles represent the experimental data. Reprint (adapted) from Schmidt et al. (2019), licensed under CC BY 4.0, ©2022 Schmidt et al..

In Fig. 3.18, the theoretical solution and experimental heat flux data are shown as a function of the radius. The data are shown $t = 2.04$ ms in (a) and $t = 2.71$ ms in (b) after the impact. The experimentally determined heat flux is averaged over all cells with the same distance from the center of the lamella. The colored area represents the scatter by one standard deviation. Both graphs show at $r \to 0$ a lower experimental heat flux than predicted by expression (3.9). The lower heat flux is most likely caused by an air bubble in the center of the impact, which is typical for drop impacts (Thoroddsen et al., 2005). In Fig. 3.18 (a), the experimental heat flux is higher than the theoretical heat flux for $0.25\,\text{mm} < r < 1.75\,\text{mm}$. The experimental data's higher heat flux and large scatter are caused by the strong nucleate boiling in the area of the liquid lamella. The heat flux is locally higher than predicted by the heat flux by conduction, as assumed in equation (3.9), due to the evaporation at the three-phase contact line. At the same time, the appearance of bubbles results in a large scatter of the heat flux. At $r > 1.75$ mm, the experimentally determined heat flux decreases. The heat flux is lower since the lamella starts to levitate beginning from the rim. For $r = r_s$, the theoretical model has a singularity due to the newly wetted area, which is non-physical.

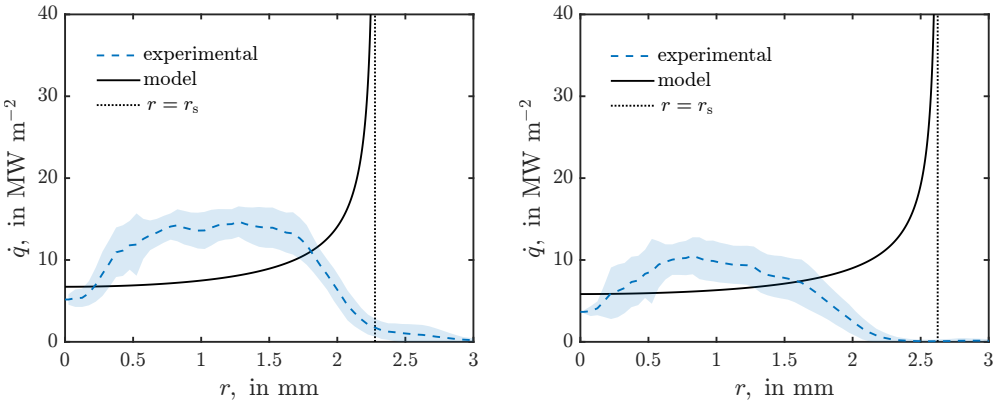

(a) $t = 2.04\,\mathrm{ms}$ (b) $t = 2.71\,\mathrm{ms}$

Figure 3.18: Heat flux of a drop impact in the thermal atomization regime. The impact velocity is $1.15\,\mathrm{m\,s^{-1}}$, and the initial surface temperature $345\,^{\circ}\mathrm{C}$. In (a), the heat flux is given $t = 2.04\,\mathrm{ms}$ after the impact. In (b), the heat flux is given $t = 2.04\,\mathrm{ms}$ after impact. In each graph, the solid line represents the theoretical model of equation (3.9) as a function of the radius. The dotted line represents the contact radius predicted by equation (3.10). The experimental data are averaged over the radius and shown by the dashed blue line. The blue area indicates the scatter of the experimental heat flux by one standard deviation.

The higher experimental flux than theoretically predicted heat flux by conduction confirms the assumption of a wetted substrate at $0.25\,\mathrm{mm} < r < 1.75\,\mathrm{mm}$. An isolating vapor layer would lead to a lower experimental heat flux, as given at $r > 1.75\,\mathrm{mm}$. The same trend can be observed in Fig. 3.18 (b). The experimental heat flux drops below the theoretically predicted heat flux in Fig. 3.18 (b) at a smaller radius than in Fig. 3.18 (a), while the theoretically predicted contact radius r_s further increases.

In Fig. 3.19, the time evolution of the wetting radius r_s is compared to the theoretical prediction of equation (3.10). The experimental wetting radius is determined from the heat flux measurements when the experimental heat flux is equal to the theoretically predicted heat flux of expression (3.9). The experimental data follow the trend of equation (3.10) until $t = 1.5\,\mathrm{ms}$. Later, the experimentally determined radius no longer follows the theoretical predictions, indicating that the lamella started levitating.

In most cases, the experimentally measured heat flux is higher than the predicted heat flux by conduction. This indicates that the liquid is in contact with the substrate, accompanied by an intense nucleate boiling. Initially, no isolating vapor layer is present, even if the surface temperature is very high.

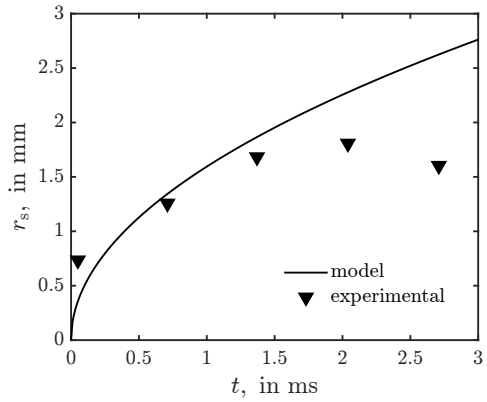

Figure 3.19: Contact radius during the spreading of the liquid lamella. The solid line represents the theoretical model of equation (3.10). The markers represent the radius at which the experimentally determined heat flux drops below the theoretically predicted heat flux for the given instance.

4 Multiple Drop Impacts and Interactions in the Drop Rebound Regime

The transient cooling of a substrate with a drop train is studied to improve understanding of drop interactions. A model of the removed heat by a drop train is introduced and validated by comparison with experiments. Parts of this section, including text and some figures, are published in Schmidt et al. (2021a, 2022, 2023a). Aspects of the experimental study are described in the thesis from Quell (2020).

When a transient cooling process approaches the thermosuperrepellency temperature, liquid patches appear at the surface. Since drop train cooling and spray cooling are often used as transient cooling processes, it is essential to understand the formation of liquid patches at hot substrates. An analytical approach to describe the appearance of fluid patches during multiple drop impacts is introduced in Section 4.2.

4.1 Drop Train Impact in the Drop Rebound Regime

The impact of multiple drops onto a hot surface may result in interactions at the surface. One possible interaction would be the direct drop-drop interactions before or during the impact at the substrate. A second possible interaction is the local temporal cooling by an impacting drop, which may affect a subsequent impacting drop.

The risk of direct drop-drop interactions is limited in the present study. The drops are impacting in the drop rebound regime, in which the drops' residence time is short. The low number flux $\dot{N}$ further decreases the risk of direct drop-drop interactions. Nevertheless, the temporal cooling of the substrate may lead to interactions. The drops of the drop train have a diameter of d_0 =2.2 mm and the impact velocity u_0 is varied between $0.45\,\mathrm{m\,s^{-1}}$ and $1.25\,\mathrm{m\,s^{-1}}$. The train number flux $\dot{N}$ is varied in the range from 0.9 Hz up to 5.7 Hz but kept constant within each experimental set. The impact target is made of stainless steel (type 1.4841) and equipped with 11 thermocouples type J. Further details are given in Chapter 2.

4.1.1 Characterization of the Drop Train Cooling

Single drops, multiple drops, and sprays rebound from hot substrates above the thermosuperrepellency temperature. Impacts of multiple drops with large time intervals $\Delta\tau$ between two impacts and drop trains with a low number flux $\dot{N} = 1/\Delta\tau$ behave comparable to single drop impacts. A drop impact of an impacting train of drops onto a hot substrate is shown in Fig. 4.1. The drop impacts at the surface, spreads, and

recedes on a large vapor cluster or a fully developed vapor layer, and finally rebounds from the substrate. The typical time scale is the natural drop oscillation time t_σ.

A drop train impacting onto a hot substrate leads to a continuous cooling of the substrate. An exemplary temperature evolution is shown in Fig. 4.2 (a). The temperature is measured 1 mm below the surface. Beginning at $T_\mathrm{w} = 550\,^\circ\mathrm{C}$, the heater is switched off, and a drop train is applied to the substrate. The drops impact with a frequency of $\dot{N} = 1\,\mathrm{Hz}$ and an impact velocity of $u_0 = 0.8\,\mathrm{m\,s^{-1}}$ onto the substrate. The surface temperature decreases over time due to drop impacts and to natural convection in the time between drop impacts. The heat loss due to natural convection becomes less with decreasing surface temperature.

Each impacting drop leads to a strong temperature drop at the surface. The typical temperature evolution of multiple drop impacts is shown in Fig. 4.2 (b). During the drop spreading and receding, the surface temperature is lowered to the vapor-solid or liquid-solid contact temperature. A thermal gradient is induced inside the substrate, as described by the heat conduction equation in the wall $\partial T_\mathrm{w}/\partial t - \alpha_\mathrm{w}\nabla^2 T_\mathrm{w} = 0$, as shown in equation (1.9). After the droplet rebounds, the substrate slowly reheats since the residence time of each droplet is short compared to the time between two impacting droplets. The residence time and the temperature decrease, measured inside the substrate, are uniform since the impact of consecutive droplets is in the same impact regime. Within the temperature-induced drop rebound regime, a vapor layer or vapor clusters insulate the drop from the substrate (Tran et al., 2012; Schmidt et al., 2021b). The isolating vapor layer of a dry drop rebound leads to reduced temperature drops compared to drop impact regimes associated with substrate wetting.

Although a temperature decrease following each drop impact can be measured for low drop train frequencies, the temperature values, as shown in Fig. 4.2 (b), should be understood qualitatively and averaged to analyze an overall temperature drop due to the impacting drop train. The temporal resolution of thermocouples is too low, and the spatial distance to the substrate surface is too large to quantify a single drop impact, as described in Section 2.2. Faster measurement techniques, like high-speed IR cameras, should be used for single drop impacts and more precise analysis of the contact temperature, as used in Section 3.3 and Castanet et al. (2020).

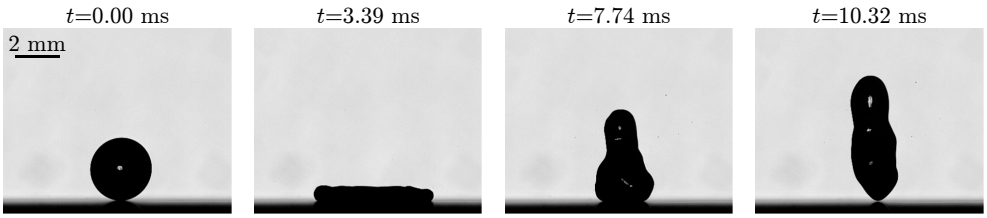

Figure 4.1: Typical rebound of a single drop impact from a train of drops in the drop rebound regime. The drop impacts onto the surface with a temperature of T_w is 555 °C. The drop spreads and recedes on a vapor layer before rebounding. Reprint (adapted) from Schmidt et al. (2023a), with permission of Elsevier Inc., © 2023 Elsevier Inc..

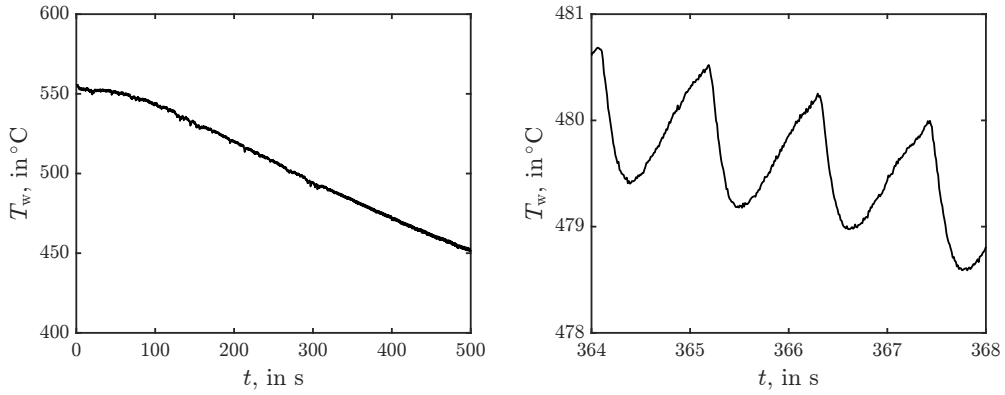

(a) overall temperature evolution

(b) detailed temperature evolution

Figure 4.2: Temperature evolution during a drop train impact onto a hot surface in the drop rebound regime. The drops impact with a number flux of $\dot{N} = 1\,\mathrm{Hz}$ onto the stainless steel target with an impact velocity of $u_0 = 0.8\,\mathrm{m\,s^{-1}}$. In (a), the overall temperature evolution during the entire experiment is shown. In (b), the temperature decrease caused by the individual impacting drops is shown. After the individual drops rebound, the substrate reheats. The temperatures are measured 1 mm below the substrate. Reprint (adapted) from Schmidt et al. (2023a), with permission of Elsevier Inc., © 2023 Elsevier Inc..

4.1.2 Model for the Heat Transfer for Drop Train Cooling

The heat transfer during the drop train impact onto a hot, thick substrate can be understood by modeling the temperature field $T_\mathrm{w}(r,t)$ inside the substrate in spherical coordinates. Consider the impact of a single liquid drop onto a solid substrate. The substrate is assumed to be semi-infinite since it is much thicker than the impacting droplet. At times much larger than the residence time of the drop, the impact can be approximated as an instantaneous event occurring at a single point on the wall surface. The perturbation of the temperature field in the wall caused by the drop impact has to satisfy the total energy balance

$$Q = 2\pi\rho_\mathrm{w} c_p \int_0^\infty r^2 \left[T_{\mathrm{w},0} - T_\mathrm{w}(r,t)\right] \mathrm{d}r, \tag{4.1}$$

where r is the radial distance in the spherical coordinate system beginning in the center of the drop impact, Q is the constant total heat transferred during the short collision event and $T_{\mathrm{w},0}$ is the initial wall temperature before the drop impact. At times $t > 0$ larger than the drop residence time, the temperature field satisfies the zero heat flux condition.

An analytical solution of the heat conduction equation equation (1.9) for the temperature increment $\Delta T(r,t) \equiv T_{\mathrm{w},0} - T_\mathrm{w}(r,t)$ is assumed in the form

$$\Delta T(r,t) = k t^w f(r/\sqrt{\alpha_\mathrm{w} t}), \quad \xi = \frac{r}{\sqrt{\alpha_\mathrm{w} t}}, \tag{4.2}$$

where k and w are unknown constants, r is the distance from the origin, $f(\cdot)$ is a yet unknown dimensionless function, and ξ is a similarity variable. This form gives a remote asymptotic solution for $\Delta T(r,t)$ valid for long times after impact $t \gg t_\sigma$ at distances higher than the drop diameter, $r \gg d_0$.

Substituting expression (4.2) for the temperature increment $\Delta T(r,t)$ in the energy balance equation (4.1) yields

$$Q = 2\pi\rho_\mathrm{w} c_p \alpha_\mathrm{w}^{3/2} t^{3/2+w} \int_0^\infty k\xi^2 f(\xi)\mathrm{d}\xi. \tag{4.3}$$

The solution, which satisfies the energy balance and the boundary conditions, can be obtained only if $w = -3/2$ since the heat is assumed to be removed in an instantaneous event, and thus Q is a constant. The corresponding solution of the heat conduction equation (1.9) then takes the form

$$\Delta T(r,t) = \frac{Q}{kt^{3/2}} \exp\left[-\frac{r^2}{4\alpha_\mathrm{w} t}\right], \quad \text{with} \tag{4.4}$$

$$k = 4\pi^{3/2}\alpha_\mathrm{w}^{3/2}\rho_\mathrm{w} c_p. \tag{4.5}$$

Consider the impact of a drop train with the time period of drop impacts denoted $\Delta\tau$. The number of impacting drops before instant t is $N = \mathrm{floor}(t/\Delta\tau) + 1$, noting that the first drop impacts at $t = 0$.

The corresponding temperature increment at time t is obtained by the superposition of the temperature perturbations by N drops, following Duhamel's theorem (Myers, 1987)

$$\Delta T = \frac{1}{k}\sum_{j=0}^{N-1} \frac{Q_j}{(t-\tau_j)^{3/2}} \exp\left[-\frac{r^2}{4\alpha_\mathrm{w}(t-\tau_j)}\right], \quad \text{with} \tag{4.6}$$

$$\tau_j = j\Delta\tau. \tag{4.7}$$

Here, τ_j is the instant of the j^{th} drop impact, and ΔT is the temperature increment due to drop impacts in relation to the initial wall temperature. In the case of significant convection, ΔT is the temperature increment in relation to the temperature evolution due to the heat convection without drop impact.

This expression can be approximated by an integral expression in the case of $N \gg 1$

$$\Delta T(r,t) \approx \frac{1}{k\Delta\tau} \int_0^{t-\Delta\tau} \frac{Q(\tau)}{(t-\tau)^{3/2}} \exp\left[-\frac{r^2}{4\alpha_\mathrm{w}(t-\tau)}\right] \mathrm{d}\tau. \tag{4.8}$$

The estimated wall temperature $T_i(t) \equiv T(0,t)$ just before an impact of a drop is therefore

$$\Delta T_i(t) \approx \frac{1}{k\Delta\tau} \int_0^{t-\Delta\tau} \frac{Q(\tau)}{(t-\tau)^{3/2}} \mathrm{d}\tau. \tag{4.9}$$

For a constant value of $Q(\tau) = Q$ we obtain for $t \gg \Delta\tau$

$$\Delta T = \frac{Q}{2r\pi\alpha_\mathrm{w}\rho_\mathrm{w}c_p\Delta\tau}\left(\mathrm{erf}\left[\frac{r}{2\sqrt{\alpha_\mathrm{w}\Delta\tau}}\right] - \mathrm{erf}\left[\frac{r}{2\sqrt{\alpha_\mathrm{w}t}}\right]\right), \tag{4.10}$$

$$\Delta T_i = \frac{Q}{2\pi^{3/2}\alpha_\mathrm{w}^{3/2}\rho_\mathrm{w}c_p\Delta\tau}\left(\frac{1}{\sqrt{\Delta\tau}} - \frac{1}{\sqrt{t}}\right). \tag{4.11}$$

The long-time approximation for the interface temperature of the wall cooled by a drop train is

$$\Delta T_{i\infty} = \frac{Q}{2\pi^{3/2}\alpha_\mathrm{w}^{3/2}\rho_\mathrm{w}c_p\Delta\tau^{3/2}}. \tag{4.12}$$

A computation of the temperature distribution within the solid substrate during a drop train impact with the number flux of 1 Hz is shown in Fig. 4.3. The temperature drop is calculated using equation (4.6) for the 5^{th}, 50^{th}, and 100^{th} drop impact of the drop train at certain time steps. The heat Q, removed by the drop impact at $t = 0\,\mathrm{ms}$ is estimated from the model for the film boiling of a single drop impact Q_fb, given in equation (1.21) from (Breitenbach et al., 2017b).

The dependence of Q on the substrate temperature is relatively weak and, in this study, for simplicity, assumed constant. The heat Q is estimated by the average of the predicted values in the temperature range considered in the experiments. The initial substrate temperature of each drop impact is a result of equation (4.6) after $t = 1000\,\mathrm{ms}$. Each image in Fig. 4.3 shows a cross-section of the impact target. The drops impact at the center of the target, which is in the upper left corner of each cross-section ($r = 0, z = 0$). The upper row shows the temperature drop ΔT of the fifth impacting droplet ($j = 5$) at different time steps after the drop impact. The first image shows a substantial temperature decrease 200 ms after the drop impact. In the following time steps, the impact substrate reheats in the center until the following drop impacts at $t = 1000\,\mathrm{ms}$. The temperature drop of the 50^{th} drop impact (middle row) and the 100^{th} drop impact (lower row) exhibit a similar evolution of the temperature field over time. The similar temperature evolution of each drop impact validates the assumption of superposition of single drop impacts.

The white dashed line represents an exemplary isotherm of $\Delta T = 2.5\,^\circ\mathrm{C}$. The position of the isotherm is nearly constant over the short time scale of a single drop impact. The propagation of the isotherm can be seen on the longer time scale between the different rows. The propagation of the isotherm shows that the thermal boundary layer reaches the bottom of the substrate after some time, violating the boundary condition of the analytical model, which is a half-infinite body.

4.1.3 Validation of the Model for the Heat Flux

After introducing the theoretical approach of the temperature evolution ΔT inside the wall, the theory is compared to the experimental temperature drop inside the hot

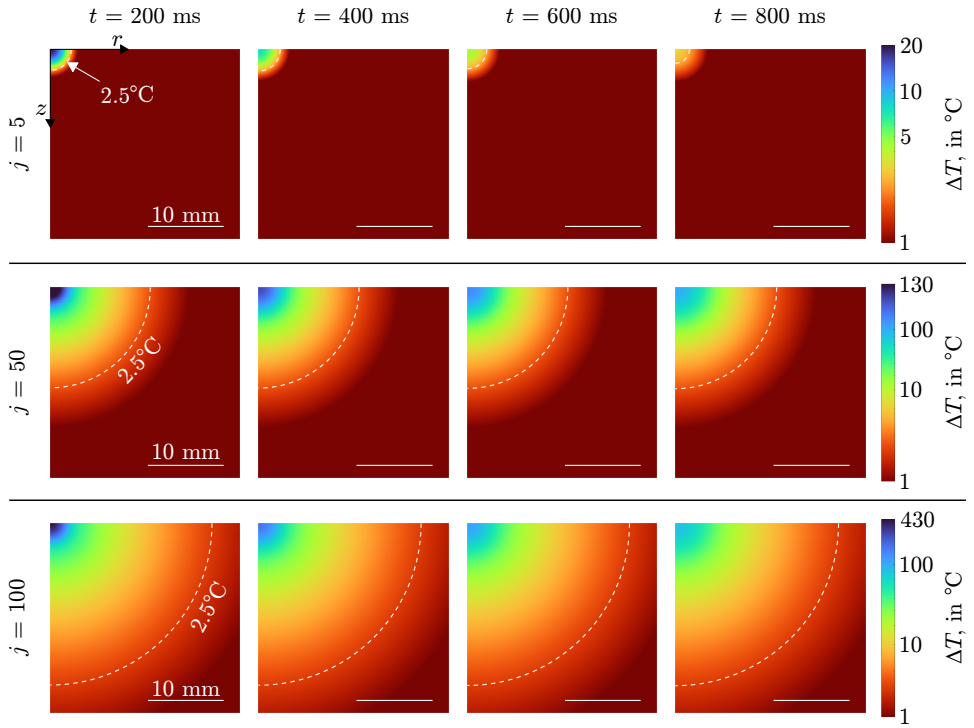

Figure 4.3: Modeled temperature drop ΔT inside the impact substrate, depending on the number of previous drop impacts and times after the respective drop impact. Half of the impact target is shown in each image for symmetrical reasons. The droplets impact at the center of the target ($r = 0$, $z = 0$) at $t = 0$ ms. The temperature is modeled 200 ms, 400 ms, 600 ms and 800 ms after the $j = 5^{\text{th}}$, 50^{th} and 100^{th} drop impact. The temperature is modeled by equation (4.6). The dashed lines represent the isothermal curve of a temperature drop of $\Delta T = 2.5\,^{\circ}\text{C}$. The figure shows the propagation of the isothermal curve after each drop impact and the propagation related to the number of previously impacted drops. The temperature drop ΔT is plotted on a logarithmic scale to better visualize the propagation of the thermal boundary layer. The bars in the left images show a scale of 10 mm. Reprint (adapted) from Schmidt et al. (2023a), with permission of Elsevier Inc., ©2023 Elsevier Inc..

substrate $\Delta T_{\mathrm{w,exp}}(t)$. An exemplary temperature evolution $\Delta T(t)$ inside the substrate is shown in Fig. 4.4 as a function of time. The temperature is measured in the substrate at the distance 1 mm from the surface. The graph shows the first 500 s after the cooling is started. The experimentally measured temperature $\Delta T_{\mathrm{w,exp}}(t) = T_{\mathrm{w,train}}(t) - T_{\mathrm{w,conv}}(t)$ is shown relative to the convection cooling as a black line. The temperature $\Delta T_{\mathrm{w,model}}(t)$ predicted by equation (4.10) is shown by the dashed line. Since the temperature dependence of Q is small, the heat Q is estimated based on the temperature measured 1 mm below the surface and averaged over the entire observed time.

The agreement between the theory and the measurements of ΔT is excellent during the first 270 s. At times $t >$270 s, the theory begins to deviate significantly from the experimental data. This deviation can be explained by the approach being developed for a semi-infinite target. The typical size of the cooled region can be estimated as $\delta_{\mathrm{t,w}} \sim \sqrt{\alpha_{\mathrm{w}} t}$. The model is valid only when $\delta_{\mathrm{t,w}}$ is smaller than the target thickness H, namely for the times smaller than H^2/α_{w}. In these experiments, $H^2/\alpha_{\mathrm{w}} \approx 200$ seconds, comparable with the time the theory deviates from the experimental data.

In Fig. 4.5 (a) the predicted temperature drop is compared to the measured ΔT for three different drop train number fluxes $\dot{N} = 1$ Hz, $\dot{N} = 2.8$ Hz, and $\dot{N} = 5.7$ Hz at $r = 1$ mm. Different colors in the figure indicate the different number fluxes. The experimental temperature increments $\Delta T_{\mathrm{w,exp}}$ (solid lines) exhibit good agreement with the predicted temperatures $\Delta T_{\mathrm{w,model}}$(dashed lines) for each number flux. The temperature increment increases with drop train number flux, as predicted by the influence of $\Delta\tau$ in equation (4.10).

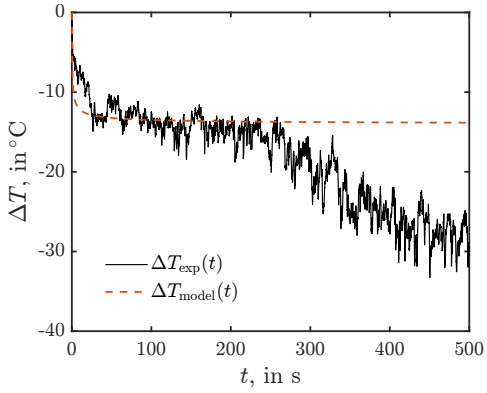

Figure 4.4: Comparison of the measured temperature increment $\Delta T_{\mathrm{w,exp}}(t)$ (solid line) with the theoretical predictions of equation (4.10) $\Delta T_{\mathrm{w,model}}(t)$ (dashed line) inside the heated target 1 mm below the surface. In the graph, an exemplary case of a drop train impact with a number flux $\dot{N} = 5.7$ Hz and impact velocity $u_0 = 0.8\,\mathrm{m\,s^{-1}}$ is shown for a time period of 500 s. After $t = 250$ s, the thermal boundary layer reaches the lower boundary of the heated target. For this reason, the measured temperature increases faster than predicted by the model. Reprint (adapted) from Schmidt et al. (2023a), with permission of Elsevier Inc., © 2023 Elsevier Inc..

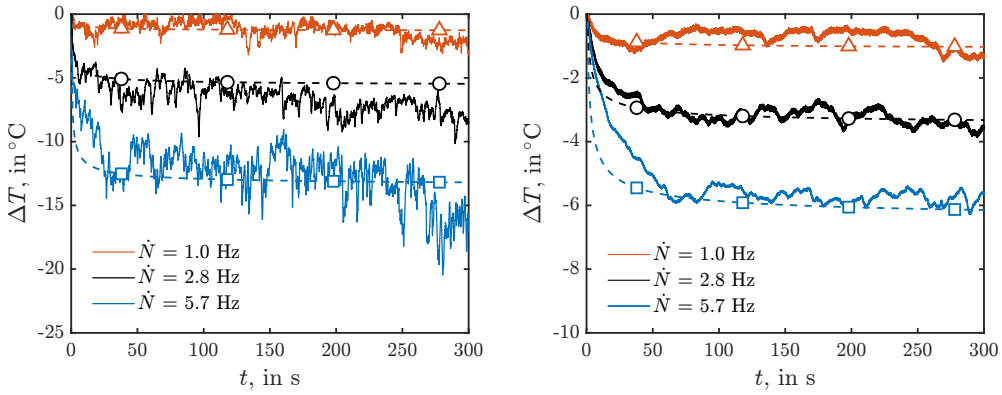

(a) $r = 1\,\text{mm}$ (b) $r = 4.5\,\text{mm}$

Figure 4.5: Comparison of the measured temperature increment $\Delta T_{\text{w,exp}}(t)$ (solid line) with the theoretical predictions of equation (4.10) $\Delta T_{\text{w,model}}(t)$ (dashed line) inside the heated target. In (a), the temperature increment is compared 1 mm below the surface, while in (b), the temperature increment is compared 4.5 mm below the surface. The temperature drop of three different drop number fluxes $\dot{N} = 1\,\text{Hz}$, $\dot{N} = 2.8\,\text{Hz}$, and $\dot{N} = 5.7\,\text{Hz}$ are shown, indicated by three different colors. The impact velocity u_0 is equal for all shown experiments. The heat Q is estimated as 0.46 J for 1 Hz, 0.44 J for 2.8 Hz and 0.38 J for 5.7 Hz from model (1.21) for a single drop impact in the film boiling regime Q_{fb} (Breitenbach et al., 2017b). The experimental temperature increments correlate well with the theoretical predictions. Reprint (adapted) from Schmidt et al. (2023a), with permission of Elsevier Inc., © 2023 Elsevier Inc..

The deviation of the temperature predictions from the experiments is associated with convection in the air. In particular, convection caused by the airflow of the moving drop train is not accounted for in the model and the calibration.

In Fig. 4.5 (b) the experimental temperature increment is compared to the theoretical prediction at a distance of $r = 4.5\,\text{mm}$, for the experiments corresponding to Fig. 4.5 (a). As expected, the temperature increment is smaller since the distance from the target surface is larger. Interestingly, the effect of the air convection and the corresponding effect on the heat flux at the surface becomes evident even at longer distances in the wall, especially for the higher drop impact frequency.

The experimental data scatter over time. This scatter increases for higher drop train frequencies due to the increasing possibility of drop interactions with subsequent impacting drops. Depending on the interactions, this can result in a larger impacting droplet or a missing impacting droplet. Drop interactions do not significantly influence the temperature drop on longer time scales since they appear infrequent and random.

Some scatter in the data can be explained by the effect of natural convection, which leads to a corresponding temperature drop. The measurements become less precise when the influence of the wall cooling by drop impacts, natural convection, and other heat losses are comparable. This is the case in Fig. 4.5 (a), for the smallest considered

number flux for which the scatter reaches values in the order of $|\Delta T|$.

The temperature decrease in a solid substrate by an impacting drop drain is measured in the present section. A simplified model is developed on the assumption that the heat, removed by the impacting drops, can be accumulated as long as the time between two impacting drops is significantly larger than the residence time of the drops. The experimental and predicted temperature decreases agree well, with some limitations at high number fluxes and at the beginning of the experiments. This model can be useful for modeling drop trains or spray cooling.

4.2 Mechanisms Leading to Substrate Wetting

While the drops do not stick to the substrate, when the temperature is above the thermosuperrepellency temperature, the wetting increases abruptly when the temperature falls below this threshold. Below the thermosuperrepellency temperature, the drop residence time at the substrate significantly increases, as considered in Section 3.1. At this temperature, the impacting drops of a train of drops and sprays start to form liquid patches at the hot substrate.

An exemplary observation of spray impact onto a hot, thick cylindrical stainless steel target is shown in Fig. 4.6. The target cooling leads to a radial temperature gradient inside the substrate. The temperature increases from the edge (left side in Fig. 4.6) towards the center of the cylinder (right side in Fig. 4.6). The drops on the right side of the figure rebound due to a high surface temperature above the thermosuperrepellency temperature. In the left regions of the figure, the surface temperature decreases, and liquid patches appear at the surface. The droplets are impacting within the transitional boiling regime. Some of the impacting drops result in liquid patches, while others rebound. The simultaneous appearance of rebounds and liquid patches can be explained by the different impact parameters of polydisperse sprays, such as drop diameter and drop velocity. Additionally, the impact of a single drop is significantly influenced by the history of the impact spot. A previous drop impact within a certain time and area cools the local area. The substrate slowly reheats after the drop rebounded or evaporated. The cooled area and reheating time of a spot increase as the substrate cools down and drops residence time increases. The locally cooled areas lead to local deviations of the boundary conditions of subsequent impacting drops. Liquid patches increase in size, with decreasing surface temperature, until they form a continuous liquid film, as shown in Fig. 4.6. The drops on the figure's left side impact the nucleate boiling regime. To describe the formation of liquid patches, it is necessary to understand the two-dimensional temperature field inside the substrate. In this section, a theoretical approach is introduced to describe the local area, cooled by a single drop impact event below the thermosuperrepellency temperature. A subsequent drop impact onto the locally cooled area results in a longer-lasting residence time than a drop impact at the overall surface temperature $T_{\mathrm{w},0}$. This theory can be further used to describe the appearance of liquid patches. The theory is based on the findings in Section 4.1.

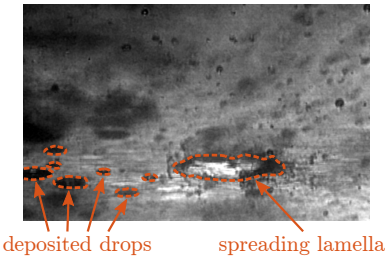

Figure 4.6: Drop impact phenomena during transient spray cooling of a hot stainless steel target. The spray drops impact in the drop rebound, transient boiling, and nucleate boiling regime, depending on the surface temperature. The thermosuperrepellency temperature in the shown case $T^* \approx 342.3\,°C$. Below the thermosuperrepellency temperature, drops start to wet the substrate, leading to liquid patches. The image is provided from Tenzer (2020).

4.2.1 Formation of Liquid Patches

Different drop impact regimes can be observed during a drop train's transient cooling of a hot substrate. The drops rebound at very high surface temperatures without wetting the substrate (as shown in Fig. 4.1). As soon as the surface temperature falls below the thermosuperrepellency temperature T^*, the impacting drops stick to the substrate before they rebound, as introduced in Section 3.2. The sticking time increases with decreasing surface temperature until they finally deposit at low surface temperatures, as described by Breitenbach et al. (2017a) for single drops. As observed for a single drop impact at different surface temperatures, the same regimes can be observed during transient cooling by a drop train, as shown in Fig. 4.7. The thermosuperrepellency temperature in the experiment shown is $T^* \approx 320\,°C$. In Fig. 4.7 (a), a wet rebound at $T_w \approx 445\,°C$ is shown. The short residence time and low number flux prevent liquid interactions between subsequent drops at the wall surface. In Fig. 4.7 (b), a drop impact is shown in the drop dancing regime, close to the thermosuperrepellency temperature. A small liquid patch remains at the wall surface after the drop rebounds. The liquid patch evaporates within a short time limit. As the temperature continues to decrease, the evaporation duration of the liquid residual increases. Consequently, the probability elevates that a subsequent drop impacts onto the liquid residual. An exemplary impact of the drop on the remaining liquid patch of the previous impact is shown in Fig. 4.7 (c). Below a threshold temperature, most drop impacts of a drop train will consecutively impact onto a remaining liquid patch. The chance of interactions depends strongly on the evaporation time of the drop and, thereby, on the surface temperature and the time between two impacts in the area of the liquid patch.

4.2.2 Theory of Liquid Patches Formation

Drop impacts close to the thermosuperrepellency temperature T^* lead to substrate wetting and ongoing nucleate boiling while the drop is at the surface. Nevertheless, the

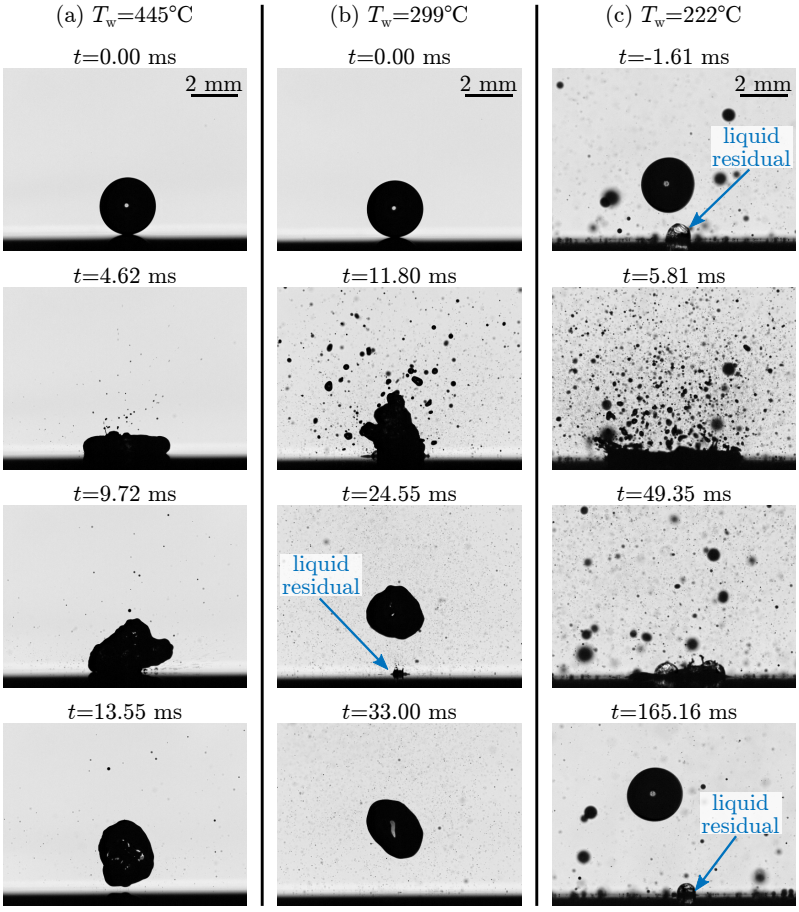

Figure 4.7: Drop impacts during a drop train cooling of a stainless steel target. The thermosuperrepellency temperature in the present experiment is at $T^* \approx 320\,^\circ$C. In (a), it is shown a drop impact in the wet drop rebound regime, while in (b), it is shown a drop impact in the drop dancing regime. The drop impact leads to a remaining liquid patch, which subsequently evaporates. In (c), a drop impact onto the remaining liquid residual is shown. At $t = 165.16$ s, the following drop of the drop train is shown, which again impacts onto the remaining liquid patch. The black bars in the upper images show the scale of 2 mm.

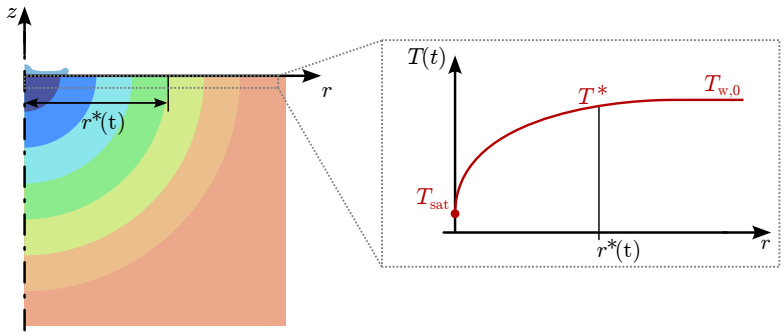

Figure 4.8: Schematic of the temperature distribution inside the solid substrate. On the left side is a substrate cross-section shown with an impacting drop. The temperature field inside the substrate develops radially, beginning from the center of the initial impacting drop. The radius * describes the radial position of the thermosuperrepellency temperature T^* and, thereby, the area at which a subsequent drop wets the substrate with a longer residence time.

residence time t_r of the drops in the wet rebound is in the same order of magnitude as a dry drop rebound. At times much larger than the residence time, the heat Q removed by a single drop impact is assumed to be removed in an instantaneous event. The heat removal causes a spherical temperature distribution inside the substrate, described by the heat conduction equation. A theoretical solution of the heat conduction equation for the temperature increment in spherical coordinates is given in equation (4.4). The theory is valid for distances $r \gg d_0$ and times $t \gg t_\mathrm{r}$. Equation (4.4) leads to the distance

$$r^{*2}(t) = -4\alpha_\mathrm{w} t \ln\left(\frac{\Delta T^*_\mathrm{iso} k t^{3/2}}{Q}\right). \tag{4.13}$$

from the drop impact center towards the position of the isotherm of the thermosuperrepellency temperature increment $\Delta T^*_\mathrm{iso} = T_{\mathrm{w},0} - T^*$, as a function of time t after the impact. The thermosuperrepellency temperature is described by equation (3.7) for surface tension dominated drop impacts and by equation (5.1) for viscous dominated drop impacts. A sketch with the coordinate system, local temperature distribution, and the radius r^* is given in Fig. 4.8.

The time t^*, until the surface is reheated above the thermosuperrepellency temperature, is determined by $r^* = 0$, which leads to

$$\ln\left(\frac{\Delta T^*_\mathrm{iso} k t^{3/2}}{Q}\right) = 0, \tag{4.14}$$

and consequently, the dimensionless time $\bar{t}$

$$\bar{t} = \left(\frac{\Delta T^*_\mathrm{iso} k}{Q}\right)^{2/3} t. \tag{4.15}$$

The position of the T^* isotherm in equation (4.13) can be rewritten in the form

$$r^{*2}(t) = -4\alpha_{\mathrm{w}}\bar{t}\left(\frac{Q}{\Delta T^*_{\mathrm{iso}}k}\right)^{3/2}\ln\left(\bar{t}^{3/2}\right), \tag{4.16}$$

depending on the dimensionless time, given in equation (4.15).

The temporal evolution of r^* is shown in Fig. 4.9 in the dimensionless form r^*/r^*_{max}. The temporal evolution shows how the radius and, thereby, the position of the T^* isotherm rapidly increases in the beginning due to the heat removed by the drop impact for $\bar{t} = 0$. After the isotherm reaches its furthest point r^*_{max}, the hot surrounding material reheats the cooled substrate. The reheating takes longer than the cooling since the driving temperature gradient is lower than the cooling.

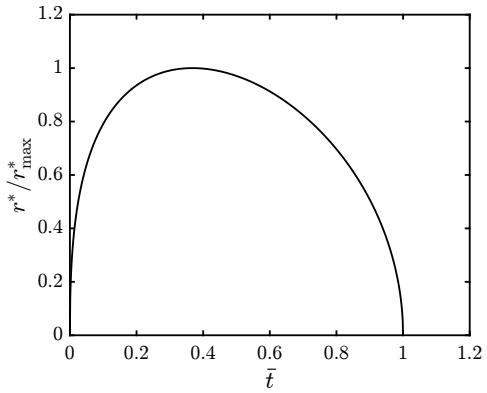

Figure 4.9: Time evolution of the radius r^*, given in equation (4.16), as a function of the dimensionless time $\bar{t}$, given in equation (4.15).

The corresponding surface area, at which the surface area cools below the thermosuperrepellency temperature T^* is described by

$$A_{T^*}(t) = \pi r^*(t)^2. \tag{4.17}$$

The time integral of equation (4.17)

$$A_{T^*,\mathrm{tot}} = \int_0^{t^*} \pi r^2(t)\mathrm{d}t, \tag{4.18}$$

describes the total duration and the area cooled below the thermosuperrepellency temperature due to a single drop impact. Inserting the radius from equation (4.16) and substitute the time t by the dimensionless time $\bar{t}$ simplifies the integral to

$$A_{T^*,\mathrm{tot}} = 4\alpha_{\mathrm{w}}\pi\left(\frac{Q}{\Delta T^*_{\mathrm{iso}}k}\right)^{4/3}\int_0^1 -\bar{t}\ln\left(\bar{t}^{3/2}\right)\mathrm{d}\bar{t}. \tag{4.19}$$

Finally, the solution of the integral gives

$$A_{T^*,\mathrm{tot}} = \frac{3}{2}\alpha_{\mathrm{w}}\pi\left(\frac{Q}{\Delta T^*_{\mathrm{iso}}k}\right)^{4/3}. \tag{4.20}$$

A subsequent drop, impacting onto $A_{T^*,\mathrm{tot}}$, impacts onto a spot below the thermosuperrepellency temperature. The lower surface temperature leads to a longer residence time and liquid residuals of the subsequent drop and eventually causes liquid patches. By the number flux density $\dot{n}$ of an impacting spray, the ratio of the wet surface is expressed by

$$\Psi = \dot{n} A_{T^*,\mathrm{tot}}. \tag{4.21}$$

Since all drops of a drop train impact onto the same spot, the ratio depends only on the time t^*. As soon as the ratio

$$\psi = \dot{N} t^* \tag{4.22}$$

is greater than one, liquid patches will accumulate.

In summary, in this section, a theoretical approach is introduced to describe the formation of liquid patches during the transient cooling with a liquid drop train and spray. The approach is based on the validated findings of Section 4.1. At this stage, the theory has not been validated by comparison with experiments. Therefore, it is not claimed that it is able to provide reliable scales for the threshold conditions for the formation of liquid patches. Nevertheless, the theory provides an explanation for the formation of liquid patches, even at surface temperatures slightly above the thermosuperrepellency temperature T^*. The local wetting and cooling of the substrate change the spatial and temporal boundary conditions for subsequent drops, enabling a longer-lasting drop residence time. The approach may be helpful to describe and predict the conditions when sprays start to cover surfaces during transient cooling and to describe the relatively wetted area.

5 Spray Cooling Related to Transitional Boiling

The threshold temperature between the transitional boiling regime and film boiling regime is modeled based on the theory of vapor percolation and thermosuperrepellency in Section 5.1. The results are compared to the experimental data from Hofmann (2019) and Tenzer (2020) and to experimental data from the literature. A predictive model of the heat flux in the transitional boiling regime is introduced in Section 5.2. The theoretical prediction is based on the findings of the drop dancing regime, as given in Section 3.1, and drop interactions, as shown in Section 4. The theory is compared to the experimental data from Hofmann (2019) and Tenzer (2020). The experimental setup and methods of the spray cooling experiments are described in Tenzer et al. (2019) and Tenzer (2020). Parts of the chapter, including text and some figures, are published in Schmidt et al. (2021b, 2023b).

5.1 Modeling of the Minimum Heat Flux Temperature

Spray cooling is often used as a transient cooling process, for example, in the forging industry (Pola et al., 2013). The heat flux removed from the target depends strongly on the present cooling regime, such as nucleate boiling, transitional boiling, and film boiling. The boundaries of these regimes are the temperature of the maximum heat flux, also called critical heat flux temperature T_{CHF}, and the temperature of minimum heat flux, the so-called Leidenfrost temperature. Knowing these regimes' boundaries is essential for using the correct model to predict the heat flux during the process. The correlations of the Leidenfrost temperature are highly empirical and partially contradicting, as shown in Section 1.2.3. In Section 5.1.1 are shown findings from the cooling experiments, which are used in the present study. The experiments have been conducted by Hofmann (2019) and Tenzer (2020). A theoretical prediction of the minimum heat flux threshold temperature is given in Section 5.1.2.

5.1.1 Minimum Heat Flux during Transient Cooling

The evolution of the heat flux $\dot{q}$ and the wall temperature at the interface T_{w} of a thick stainless steel target, continuously cooled by spray impact, are shown in Fig. 5.1. The target is initially heated uniformly up to $T_{\mathrm{w}} \approx 450\,^{\circ}\mathrm{C}$. The surface temperature (shown in blue) decreases slowly at the beginning of the experiment. The corresponding heat flux (shown in orange) is accordingly low. After about 75 s, the heat flux is at its minimum. The corresponding temperature T^* is denoted as the lowest wall temperature at which the drop does not stick to the substrate. The temperature T^* is

often denoted as Leidenfrost point T_L. Further cooling the substrate leads to a rapidly decreasing surface temperature and significantly increasing heat flux, as shown in Fig. 5.1. This regime is also known as the transitional boiling regime in spray cooling. The heat flux reaches its maximum at the critical heat flux temperature T_CHF. From this threshold temperature on, the temperature gradient and heat flux decrease.

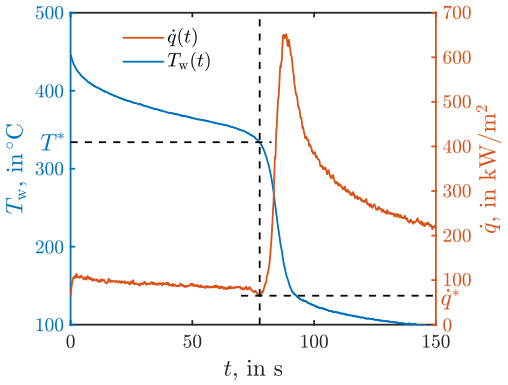

Figure 5.1: Exemplary results for the evolution of the heat flux $\dot{q}$ and surface temperature T_w as a function of time t for spray cooling with distilled water. The threshold temperature T^* at the instant t^* corresponds to the minimum heat flux. Reprint (adapted) from Schmidt et al. (2023b), with permission of Elsevier Ltd., © 2023 Elsevier Ltd..

High-speed observations of spray impact are shown in Fig. 5.2. On the right image are shown drop rebounds at a surface temperature of $T_\mathrm{w} \approx 350\,°\mathrm{C}$. On the left image are shown deposited drops and the beginning of liquid patches at $T_\mathrm{w} \approx 340\,°\mathrm{C}$. The images demonstrate that the threshold temperature T^* is associated with the minimum of the heat flux curve and, indeed, determines the deposition/rebound limit for the impacting drops.

The value of the threshold temperature T^* depends neither on the drop diameter in the spray nor on the impact velocity but on the target material, as is demonstrated in Figs. 5.3 (a) and (b). Moreover, no dependence of the temperature T^* on the mass flux of the impacting spray or other impact properties is identified. Further insights of the comprehensive study are given in Tenzer (2020).

5.1.2 Thermosuperrepellency Temperature

It can be assumed that the total heat $Q = \int_0^{t_\mathrm{r}} A(t)\dot{q}(t)\mathrm{d}t$ removed from the substrate by a single impacting drop is at its minimum when the drops start to rebound without sticking. Here, $A(t)$ is the covered area at the substrate by an impacting, single drop. The minimum heat is most likely explained by the single drop regimes at the temperatures above, respectively, below T^*. At $T_\mathrm{w} > T^*$, drops rebound. The residence time t_r and wetted area $A(t)$ of a single drop in this regime stay constant, while the heat flux $\dot{q}(t)$ increases ($\dot{q} \sim \Delta T_\mathrm{w}$), as shown in Section 1.2.2. This results in a slightly

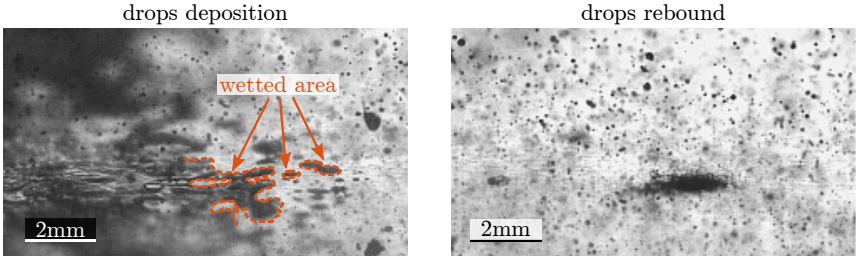

Figure 5.2: The left image shows liquid patterns at surface temperatures $T_w \approx 340\,^{\circ}\mathrm{C}$ close to the threshold temperature T^*. The impacting drops on the right image rebound or splash at a surface temperature of $T_w \approx 350\,^{\circ}\mathrm{C}$, above the threshold temperature T^*. Reprint (adapted) from Schmidt et al. (2021b), licensed under CC BY 4.0, ©2021 Schmidt et al..

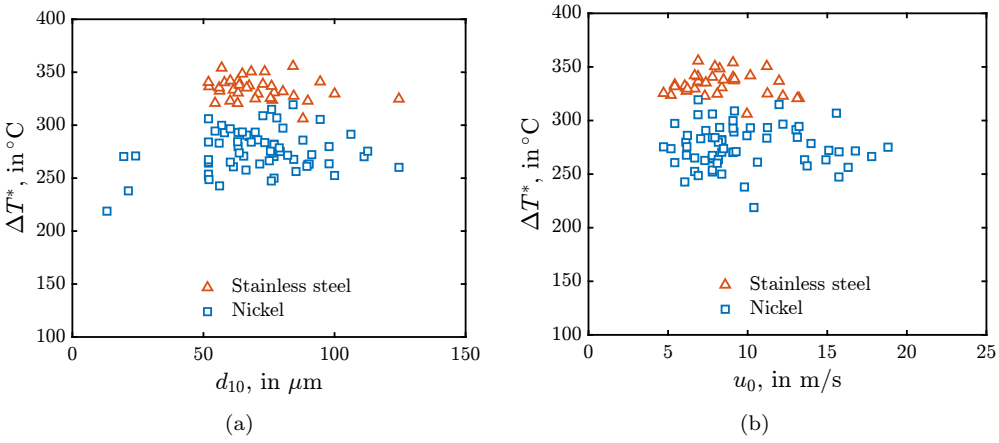

Figure 5.3: In (a) and (b) is shown the dependence of the threshold temperature T^* on the average drop diameter d_{10} spray and on the average impact velocity u_0, respectively. Each point represents a spray cooling experiment's threshold temperature T^*. Reprint (adapted) from Schmidt et al. (2021b), licensed under CC BY 4.0, ©2021 Schmidt et al..

increasing Q. With $T_\mathrm{w} < T^*$, drops stick to the surface before they rebound. The drops' residence time $t_\mathrm{r} \approx t_\epsilon$ increases ($t_\epsilon \sim \Delta T_\mathrm{w}^{-2}$), while the heat flux slightly decreases ($\dot{q} \sim \Delta T_\mathrm{w}$), as shown in Section 3.1. Again, this results in an increasing Q. This follows the assumption that the minimum heat flux temperature agrees with the boundary temperature between the drop dancing regime and the wet drop rebound regime.

The thermosuperrepellency temperature, which describes the threshold temperature between the drop dancing regime and wet drop rebound regime, is introduced in Section 3.2. The mechanism of vapor percolation leads to the non-sticking drop rebound as soon as $t_\epsilon < t_\sigma$ for drop impacts in the surface tension dominated regime. The resulting threshold temperature $\Delta T = b\Delta T_\sigma$ is given in equation (3.7). The criteria of the surface tension dominated regime is $\mathrm{We} \ll 2.5\,\mathrm{Re}^{2/5}$.

For very high Weber numbers, the duration of drop spreading is scaled by the viscous time scale $t_\nu = d_0\mathrm{Re}^{1/5}/u_0$, as given in equation (1.3). The percolation condition $\epsilon = \epsilon_\mathrm{c}$ at the instant $t = t_\nu$ yields another expression for the threshold wall overheat ΔT_ν in the viscous spreading regime

$$\Delta T = b\,\Delta T_\nu, \quad \Delta T_\nu = \frac{\rho_\mathrm{l}\sqrt{\nu}L^*}{e_\mathrm{w}}. \tag{5.1}$$

The expression for ΔT_ν does not depend on the drop diameter or impact velocity. This is not surprising since the time t_ν and the lamella thickness h_res correspond to the one-dimensional growth of the viscous boundary layer in the lamella.

In Fig. 5.4, the theoretically predicted scales for the threshold temperature ΔT_ν are compared with the experimental data ΔT^*. The slope for spray impact is, however, more significant than for a single drop since the thermodynamic processes in the spreading drop are influenced significantly by the flow, although the expressions for the viscous length scale and the time scale of capillary oscillations remain the same. The values for ΔT^* are determined from the condition of the minimum of the heat flux. The experimental data are provided by Tenzer (2020) and the literature. An overview of the data is given in Table 5.1. Note also that in the spray case, the surface temperature is not uniform and continuous since it is influenced by single drop impacts. Each drop impact leads to a significant local cooling of a substrate. The subsequent drop could impact onto this relatively cold spot and thus initiate a wetted boiling region, with some probability, depending on the spray flux. This is introduced in Chapter 4. This phenomenon is identified using the high-speed video observations of spray impact onto very hot substrates by Tenzer et al. (2019). The nucleate boiling in these wetted regions contributes significantly to the heat flux. The surface temperature is determined as a time and space averaged value due to the low temporal and spatial resolution in the spray cooling experiments.

Moreover, the threshold temperature during spray cooling can also be influenced by the thermal atomization phenomenon associated with the drop levitation when the thermal boundary layer reaches the free surface of the drop spreading lamella (Roisman et al., 2018). It can be shown with the help of $h_\mathrm{res} \approx 0.79\,d_0\,\mathrm{Re}^{-2/5}$, that the residence

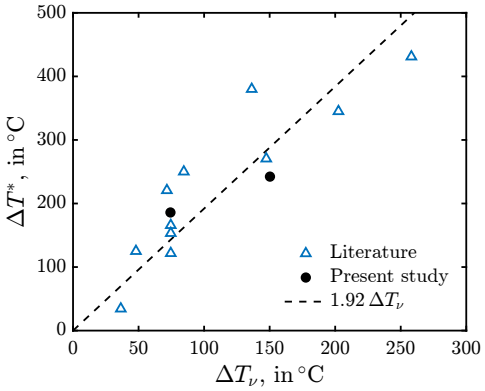

Figure 5.4: Comparison of the threshold overheat temperatures ΔT^*, with the theoretically predicted scales of the threshold overheat ΔT_ν, given in expression (5.1). The experimental threshold overheat is determined by the temperature of minimum heat flux. The data for different substrate materials from this study and the literature are listed in Table 5.1. The data from the present study are averaged for each substrate material since ΔT_ν is independent of spray parameters. Reprint (adapted) from Schmidt et al. (2021b), licensed under CC BY 4.0, ©2021 Schmidt et al..

time t_θ of the thermal atomization regime is

$$t_\theta = t_\nu \mathrm{Pr}, \tag{5.2}$$

where Pr is the Prandtl number characterizing the drop liquid. Some influence of the Prandtl number on the slope of the linear dependence of ΔT^* on ΔT_ν can thus be expected when the effect of thermal atomization is significant. Such an effect can only be identified in spray cooling experiments with different liquids.

Several hypotheses are put forward in the literature to explain the mechanism of film boiling. Some theoretical models are developed based on the hydrodynamic stability analysis of the vapor/liquid interface (Zuber, 1958; Kakac & Bon, 2008) or thermocapillary stability (Aursand et al., 2018). Other authors assume that the Leidenfrost temperature is determined by the foam limit (Spiegler et al., 1963; Wang et al., 2020b) or by the limiting minimum vapor thickness (Cai et al., 2020) comparable with the surface roughness. In this section, it is demonstrated that the transition to the so-called film boiling regime is initiated at the threshold point for vapor percolation. For the single drop impacts, it is known that the wet rebound and thermal atomization are associated with substrate wetting, as shown in Chapter 3. Both regimes appear above the thermosuperrepellency temperature. Further, drop evaporation is governed by the presence of the vapor rivulets and is characterized by the disappearance of the isolated wetted spots. The so-called film boiling regime is partially determined by drop impacts, wetting the substrate. A fully developed vapor film corresponds to completely vanishing the wetted spots.

Study	Type of Experiment	Substrate material	e_w $Ws^{1/2}m^{-2}K^{-1}$	ΔT^* °C
Present study	Spray	Inox (1.4841)	8.8501×10^3	242
Present study	Spray	Nickel (2.4068)	1.7892×10^4	186
Hoogendoorn & den Hond (1974)	Spray	Inox (1.4301)	9.0193×10^3	271
Shoji et al. (1984)	Spray	Nickel	1.8569×10^4	221
Ito et al. (1991)	Spray	Copper	3.6476×10^4	34
Yao & Choit (1987)	Spray	Cu & Cr plating	1.7831×10^4	122
Choi & Yao (1987)	Spray	Cu & Cr plating	1.7831×10^4	153
Yao & Cox (2002)	Spray	Cu & Cr plating	1.7831×10^4	166
Bernardin et al. (1997)	Chain	Cu & Au plating	2.7701×10^4	125
Tran et al. (2012)	Drop	Silicon wafer	9.7544×10^3	380
Wang et al. (2020b)	Drop	FeCrAl	6.5664×10^3	345
Wang et al. (2020b)	Drop	SiC	1.5733×10^4	250
Wang et al. (2020b)	Drop	Zr-4	5.1511×10^3	431

Table 5.1: Overview of the reference, type of experiment, substrate material, thermal effusivity of the substrate, and threshold temperature, as used in Fig. 5.4.

5.2 Modeling Heat Flux in Transitional Boiling Regime

As soon as the surface temperature drops below the thermosuperrepellency temperature, the boiling is determined by transitional boiling. The heat flux in this regime is weakly studied and described, as shown in Section 1.2.3. A predictive model of the heat flux in the transitional boiling regime during spray cooling is developed in this section. First, the drop interactions are taken into account. Later, the heat removed by a single impacting drop in the drop dancing regime is determined. In the end, the model for the heat flux is developed, compared to experimental results from Hofmann (2019) and Tenzer (2020), and finally discussed.

5.2.1 Drop Interactions in the Transitional Boiling Regime

The heat flux during spray cooling can be determined by the superposition of single drop events as long as the single drop events have few interactions. This assumption is valid for a low number flux $\dot{n}$ and short residence times, as shown in Chapter 4. Interacting drop impacts reduce the heat flux due to the smaller total wetted area. The losses due to drop interaction can be specified by an effective wetted area η_{wet} and the cumulative wetted area. In the case of a Poisson distribution of drop impact positions, the effective wetted area is given by $\eta_{wet} = (1 - e^{-\gamma})/\gamma$, as shown by Breitenbach et al. (2017b). The total cumulative wetted area is then determined as

$$\gamma = \dot{n} \int_0^\infty p_d \int_0^{t_\epsilon} \pi r_s(t)^2 \, dt \, dd_0, \tag{5.3}$$

with the probability density function of the drop diameter in a polydisperse spray p_d. The number flux can be estimated from the values of the measured mass flux density and the mean drop diameter $\dot{n} = 6\dot{m}/(\pi\rho_\mathrm{l}\, d_{10}^3)$, leading to the following expression

$$\gamma = \frac{6\dot{m}}{\rho_\mathrm{l} d_{10}^3} \int_0^{t_\epsilon} r_\mathrm{s}(t)^2 \,\mathrm{d}t, \tag{5.4}$$

obtained in Breitenbach et al. (2017b).

The evolution of the wetted area $\pi r_\mathrm{s}(t)^2$ can be divided into two stages. First, the droplet spreads after its impact, which can be estimated by the engineering approximation

$$r_\mathrm{s}(t) \approx r_\mathrm{max} \sqrt{1 - \left(1 - \frac{t}{t_\mathrm{max}}\right)^2}, \tag{5.5}$$

with the time instance t_max when the maximum spreading radius $r_\mathrm{max} = d_\mathrm{max}/2$ is reached, as described by Batzdorf et al. (2017). The wetted area and the lamella thickness remain constant as soon as the viscous boundary layer dampens further spreading, namely when $t = t_\nu$. The contact radius can be estimated as an engineering approximation by the section-wise defined function

$$r_\mathrm{s}(t) = \begin{cases} r_\mathrm{max} \sqrt{1 - \left(1 - \frac{t}{t_\mathrm{max}}\right)^2}, & \text{if } t < t_\nu \\ r_\mathrm{max} \sqrt{1 - \left(1 - \frac{t_\nu}{t_\mathrm{max}}\right)^2} = \text{const}, & \text{if } t \geq t_\nu. \end{cases} \tag{5.6}$$

The maximum spreading radius is taken from equation (1.4), and the time t_max is equal to half of the drop oscillation time $t_\mathrm{max} = t_\sigma/2$.

An example of the contact radius evolution is shown in Fig. 5.5. The drop spreads until the lamella flow is damped, marked by the dashed line. Later, the radius remains constant until t_ϵ is reached. The initial drop diameter and impact velocity are in the same order of magnitude as in the spray cooling experiments.

Equation (5.4) can be further simplified with the help of equation (5.6) to

$$\gamma = \frac{6\dot{m}}{\rho_\mathrm{l}\, d_0^3} \begin{cases} r_\mathrm{max}^2 t_\epsilon^2 \frac{3t_\mathrm{max} - t_\epsilon}{3t_\mathrm{max}^2}, & \text{if } t_\epsilon < t_\nu \\ r_\mathrm{max}^2 t_\nu \frac{(6t_\mathrm{max} - 3t_\nu)t_\epsilon + 2t_\nu^2 - 3t_\mathrm{max} t_\epsilon}{3t_\mathrm{max}^2}, & \text{if } t_\epsilon \geq t_\nu. \end{cases} \tag{5.7}$$

Based on equation (5.7) the effective wetted area η_wet can be computed. The results for the present experiments are shown for different mass fluxes in Fig. 5.6 depending on the wall superheat. The plotted temperature range corresponds to the temperature range of the transitional boiling regime, as shown in Fig. 5.1. The experimental spray cooling data sets are clustered by k-mean analysis, following Lloyd (1982). The effective wetted area is close to 1 for all three mass flux densities. As the wall temperature decreases, η_wet decreases due to the longer residence times of the droplets and thus an increase in the intersection probability. Nevertheless, η_wet remains close to 1 for the entire transitional boiling regime, which describes a low level of wetted area intersections.

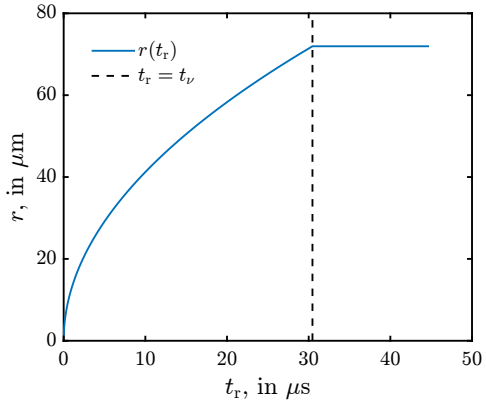

Figure 5.5: Time evolution of the contact radius during a single drop impact based on equation (5.6). The dashed line indicates when the flow in the lamella is damped, and the drop radius remains constant. Reprint (adapted) from Schmidt et al. (2023b), with permission of Elsevier Ltd., ©2023 Elsevier Ltd..

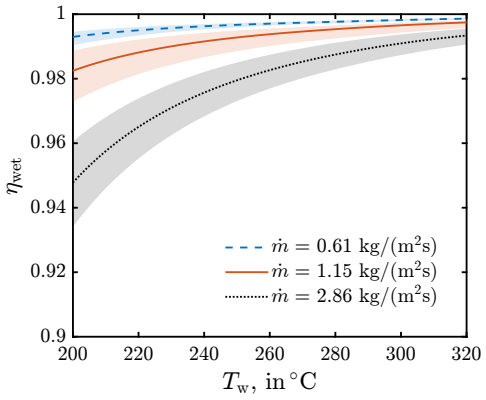

Figure 5.6: Effective wetted area η_wet, calculated using equation (1.31), as a function of wall temperature for different mass fluxes. The percolation time of the droplets increases with decreasing surface temperature, leading to more intersections and a lower effective wetted area. The data sets are clustered into three sets of mass fluxes. The colored area represents one standard deviation of the corresponding data cluster. Reprint (adapted) from Schmidt et al. (2023b), with permission of Elsevier Ltd., ©2023 Elsevier Ltd..

5.2.2 Heat Flux in the Transitional Boiling Regime

The heat flux during spray cooling depends on the single drop impact regime. The dependency is illustrated schematically in Fig. 5.7. The heat flux in the nucleate boiling regime is mainly caused by the deposition of drops, nucleate boiling, and liquid film formation, as shown by Tenzer et al. (2019). At high surface temperatures, the dry drop rebound without wetting the substrate is the prominent impact regime, leading to the film boiling regime in spray cooling. Both are determined by a fully developed vapor layer between the impacting drops and the hot surface. At temperatures below the thermosuperrepellency temperature, the transitional boiling is mainly determined by the drop dancing regime.

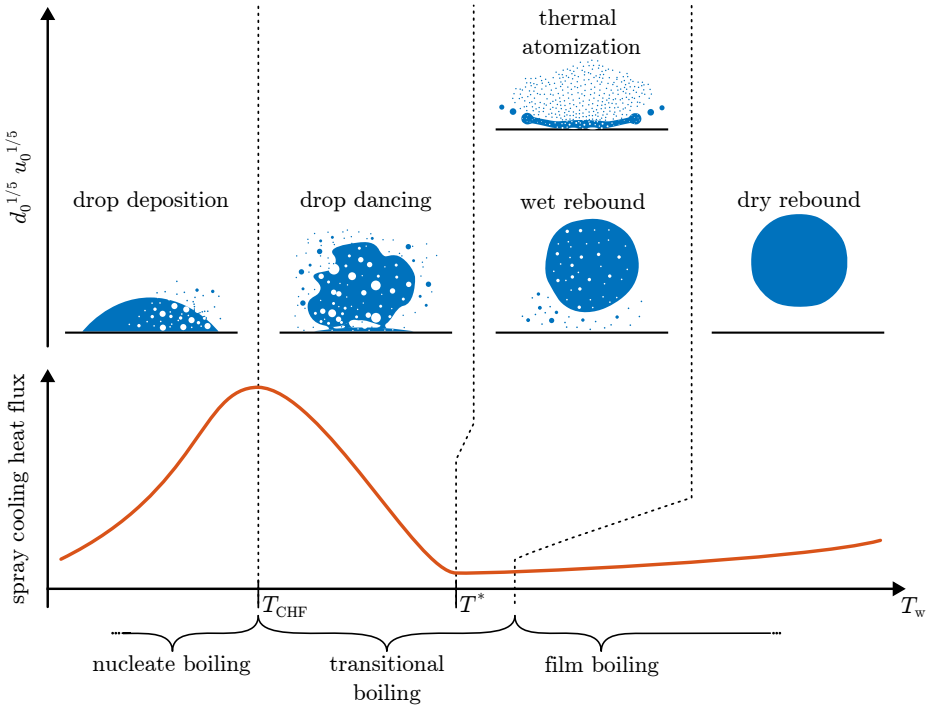

Figure 5.7: Illustration of the spray cooling regimes and corresponding heat flux in the lower part of the figure. Above are the determining single drop impact regimes illustrated. The transitional boiling regime between the thermosuperrepellency temperature and critical heat flux temperature is mainly determined by the drop dancing regime. Reprint (adapted) from Schmidt et al. (2023b), with permission of Elsevier Ltd., © 2023 Elsevier Ltd..

The low level of interactions in the present experiments allows the heat flux of spray cooling to be modeled by the superposition of individual drop events, corrected by the effective wetted area η_{wet}

$$\dot{q}_{\mathrm{theoretical}} = \eta_{\mathrm{wet}} \dot{n} Q, \tag{5.8}$$

with Q being the heat removed by a single drop. The heat flux can be expressed with the heat removed by a single drop in the drop dancing regime, as given in equation (3.6), in the form

$$\dot{q}_{\text{theoretical}} = \frac{6\,\dot{m}\,\eta_{\text{wet}}}{\rho_{\text{l}}\,d_{10}^3} \int_0^{t_\epsilon} \frac{e_{\text{w}}\Delta T_{\text{w}}}{\sqrt{\pi t}}\, r_{\text{s}}(t)^2 \mathrm{d}t. \tag{5.9}$$

For percolation times t_ϵ smaller than t_ν, equation (5.9) yields

$$\dot{q}_{\text{theoretical}} = \frac{6\,\dot{m}\,\eta_{\text{wet}}}{\rho_{\text{l}}\,d_{10}^3}\, e_{\text{w}}\Delta T_{\text{w}} \int_0^{t_\epsilon} \frac{r_{\text{max}}^2}{\sqrt{\pi t}} \left[1 - \left(1 - \frac{t}{t_{\text{max}}}\right)^2\right] \mathrm{d}t. \tag{5.10}$$

The integration of the expression in the right-hand side of (5.10) leads to

$$\dot{q}_{\text{theoretical}} = \frac{2\,\dot{m}\,\eta_{\text{wet}}\, e_{\text{w}}\Delta T_{\text{w}}\, r_{\text{max}}^2 \sqrt{t_\epsilon}\left(6t_\epsilon^2 - 20 t_{\text{max}} t_\epsilon\right)}{5\,\rho_{\text{l}}\,d_{10}^3\,\sqrt{\pi}\,t_{\text{max}}^2}. \tag{5.11}$$

For percolation times t_ϵ greater than t_ν, the integral of equation (5.9) must be split into two parts to correspond to the piece-wise estimation of the contact radius from equation (5.6):

$$\begin{aligned}\dot{q}_{\text{theoretical}} = \frac{6\,\dot{m}\,\eta_{\text{wet}}}{\rho_{\text{l}}\,d_{10}^3}\, e_{\text{w}}\Delta T_{\text{w}} \Bigg(& r_{\text{max}}^2 \int_0^{t_\nu} \frac{1}{\sqrt{\pi t}} \left[1 - \left(1 - \frac{t}{t_{\text{max}}}\right)^2\right] \mathrm{d}t \\ & + r_{\text{max}}^2 \left[1 - \left(1 - \frac{t_\nu}{t_{\text{max}}}\right)^2\right] \int_{t_\nu}^{t_\epsilon} \frac{1}{\sqrt{\pi t}} \mathrm{d}t \Bigg).\end{aligned} \tag{5.12}$$

Integrating the equation gives

$$\begin{aligned}\dot{q}_{\text{theoretical}} = \frac{6\,\dot{m}\,\eta_{\text{wet}}\, e_{\text{w}}\Delta T_{\text{w}}\, r_{\text{max}}^2}{\rho_{\text{l}}\,d_{10}^3\,\sqrt{\pi}} \Bigg(& \frac{\sqrt{t_\nu}\left(6t_\nu^2 - 20 t_{\text{max}} t_\nu\right)}{15 t_{\text{max}}^2} \\ & + \left(2\sqrt{t_\epsilon} - 2\sqrt{t_\nu}\right) \left[1 - \left(1 - \frac{t_\nu}{t_{\text{max}}}\right)^2\right] \Bigg).\end{aligned} \tag{5.13}$$

In Fig. 5.8, the experimentally determined heat flux divided by the theoretical prediction in the temperature range of the transitional boiling regime is shown for different spray parameters. The ratio of the measured and theoretically predicted heat flux is shown for the mass flux densities $\dot{m} = 0.61\,\mathrm{kg\,m^{-2}\,s^{-1}}$, $\dot{m} = 1.15\,\mathrm{kg\,m^{-2}\,s^{-1}}$, and $\dot{m} = 2.86\,\mathrm{kg\,m^{-2}\,s^{-1}}$. The heat flux is calculated using equation (5.11) for temperatures higher than the dotted-dashed black line corresponding to the point at which $t_\epsilon = t_\nu$, and using equation (5.13) for lower temperatures at which $t_\epsilon > t_\nu$.

For all the spray impact parameters considered, the theoretical predictions and the experimental data for the heat flux are in the same order of magnitude despite the fact that no adjustable parameters are used to model the heat flux. The modeling is based exclusively on the results obtained by analyzing the single drop impact

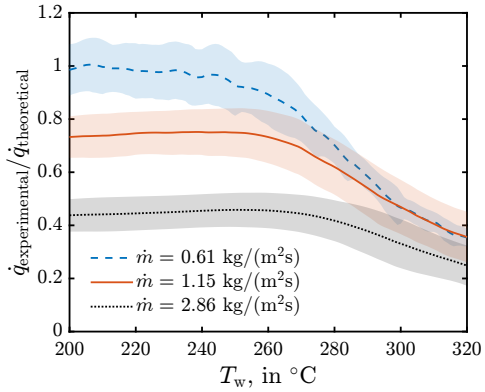

Figure 5.8: The measured heat flux during spray cooling compared to the theoretical predictions of the heat flux by equation (5.13).The heat flux is predicted by equation (5.11) for temperatures above $T(t_\epsilon = t_\nu)$. and by equation (5.13) for temperatures below $T(t_\epsilon = t_\nu)$. The data sets are clustered into three sets of mass flux densities. The colored area represents one standard deviation of the corresponding data cluster. Reprint (adapted) from Schmidt et al. (2023b), with permission of Elsevier Ltd., © 2023 Elsevier Ltd..

in the drop dancing regime. Moreover, it is interesting that for a relatively low mass flux, $\dot{m} = 0.61\,\mathrm{kg\,m^{-2}\,s^{-1}}$ and wall temperatures below the point, at which $t_\epsilon = t_\nu$, the agreement between the model and the theory is very good, since the ratio $\dot{q}_{\text{experimental}}/\dot{q}_{\text{theoretical}}$ approaches unity.

At higher wall temperatures and spray mass fluxes, the theory overpredicts the values of the spray impact generated heat flux. There are several possible reasons for this overprediction. One reason may be related to the spray produced by thermal atomization, as described in Section 1.2.2 and Section 3.3.

Another possible reason for the deviation between predictions and experiments is hydrodynamic induced splashing. In the present experiments, the increase of the spray mass flux $\dot{m}$ is accompanied by a significant increase of the impact velocity, thus, leading to a gain in secondary droplet mass flux and a corresponding decrease in heat flux.

The splash of a single drop impact onto a wetted substrate or of spray impact under isothermal conditions is often characterized by the K-number $\mathrm{K} = \mathrm{We}^{4/5}\mathrm{Re}^{2/5}$, as given in equation (1.5), used mainly for the modeling of the splashing threshold. Breitenbach et al. (2018b) describes that the splashed mass ratio of an impacting spray is a function of the K-number $\dot{m}_\mathrm{a}/\dot{m}_\mathrm{b} = 0.5 - 0.616\exp(-\mathrm{K}/750.9)$, where $\dot{m}_\mathrm{b}$ is the mass flux of the impacting spray and $\dot{m}_\mathrm{a}$ is the corresponding mass flux of secondary drops, as described in equation (1.6).

The deposited mass ratio $1-\dot{m}_\mathrm{a}/\dot{m}_\mathrm{b}$ is probably one of the most important parameters influencing the value of the heat flux ratio $\dot{q}_{\text{experimental}}/\dot{q}_{\text{theoretical}}$ since no influence by the impact velocity or Reynolds number is identified. In Fig. 5.9, the measured critical heat flux (CHF), scaled by the theoretically predicted value, is shown as a

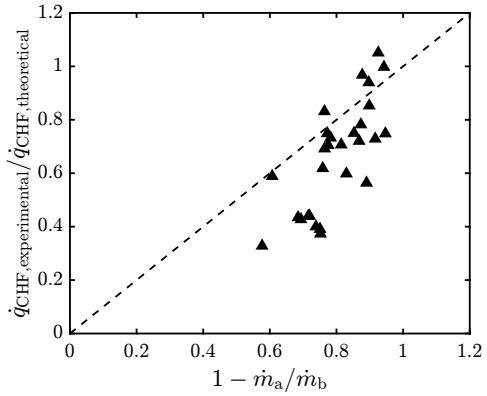

Figure 5.9: Experimentally determined critical heat flux $\dot{q}_{\mathrm{CHF}}$, divided by its theoretical prediction, as a function of the deposited mass ratio, calculated using an empirical relation (1.6) valid for isothermal conditions. The dashed line represents an ideal agreement. Reprint (adapted) from Schmidt et al. (2023b), with permission of Elsevier Ltd., ©2023 Elsevier Ltd..

function of the deposited mass ratio $1 - \dot{m}_\mathrm{a}/\dot{m}_\mathrm{b}$, calculated using (1.6). The dashed line corresponds to a perfect agreement $\dot{q}_{\mathrm{experimental}}/\dot{q}_{\mathrm{theoretical}} = 1 - \dot{m}_\mathrm{a}/\dot{m}_\mathrm{b}$. It is interesting to note that the theory for the heat flux agrees best with the experimental data when the deposited mass ratio approaches unity. Furthermore, the data for $1 - \dot{m}_\mathrm{a}/\dot{m}_\mathrm{b}$ indicate that the splashed mass of the spray droplets is indeed a significant factor influencing the heat flux of spray cooling at higher impact velocities, significantly exceeding the splashing threshold.

The experimental data might be affected by multiple error sources, such as the spray characterization with phase Doppler measurements, temperature measurements with thermocouples, and the inverse heat flux calculation. Nevertheless, the measured data are in the same order of magnitude as the theoretical predictions and agree well for low number fluxes.

Some systematic deviation from the perfect agreement can be explained by the lack of a reliable model for the deposited mass ratio at higher temperatures, where microscale thermodynamic effects such as boiling or thermal Marangoni effects can also influence the splash. Future development of such a splash model at high wall temperatures may further improve the heat flux model in the transitional boiling regime.

6 Conclusions and Outlook

The present study aims to establish reliable and predictive theoretical models for spray cooling regimes related to transitional boiling and their regime limits. Models to describe substantial quantities of single drop impacts and spray cooling related to the transitional boiling regimes are proposed within this study. First, the single drop impact regimes drop dancing, wet drop rebound, and thermal atomization, related to transitional boiling effects and defined in Fig. 3.1, are investigated in detail.

In the drop dancing regime, the impacting drop starts to hover and "dance" after some characteristic time. This characteristic time is measured and modeled considering the effect of vapor bubble percolation. The effect of vapor bubble percolation describes the intersection of vapor bubbles in the liquid lamella of an impacting drop. The intersecting vapor bubbles lead to infinite vapor clusters and a thermally induced repellency effect. The termed thermosuperrepellency effect is similar to Cassie-Baxter wetting. The time until the liquid detaches and hovers is modeled by the percolation time t_ϵ. The theoretical prediction of t_ϵ agrees well with the experimental results for different impact velocities. The experimental data agree excellently with the theoretical predictions, which indicate that all essential factors are considered in the model. The heat removed by a single drop is then estimated by the integral of the heat flux in the substrate over the area wetted by the drop and the percolation time since most of the drop liquid detaches after t_ϵ.

The threshold temperature between the drop dancing and wet drop rebound regime is determined from the observations of drop impact. The theory of vapor percolation and thermosuperrepellency is applied to determine this threshold temperature. As soon as the percolation time drops below the typical rebound time of drops, the residence time of the drops at the substrate stay constant. This criterion allows to describe the thermosuperrrepellency temperature. The theory agrees well with experimental studies for different substrate materials, liquids, and impact velocities.

Furthermore, the physics determining the wet drop rebound regime are studied using the infrared measurement technique. It is shown that even at temperatures above the thermosuperrrepellency temperature drops initially wet the substrate. Drops in the wet rebound regime initially wet the substrate, leading to a strong nucleate boiling. This explains the observation of secondary drops and vapor bubbles inside the rebounding drop. During the spreading, percolating vapor bubbles lead to infinite vapor clusters and rivulets at the solid/liquid interface. Due to the formation of vapor clusters, the drop can rebound with less disturbances. The quickly appearing vapor clusters dominate the flow in the lamella and determine the wet rebound regime.

In the thermal atomization regime, a two-dimensional heat flux model is developed.

The theory is compared to high-speed infrared measurements. The theory underpredicts the heat flux due to an intense nucleate boiling in the wetted areas. Nevertheless, comparing the experimental data with the theory shows a good agreement of the radial propagation of the lamella's three-phase contact line during the milliseconds after the impact. The theory and experimental data approve the assumption of substrate wetting and wetting propagation from Roisman et al. (2018).

The interactions of drops are studied in the framework of a drop train impacting onto a hot substrate within the drop rebound regime. The impacting drop train leads to a temperature decrease in the substrate and transient cooling. An approximate theoretical model is developed to predict the evolution of the wall temperature caused by drop train cooling. The model is based on an instantaneous source point of a finite amount of heat transferred from the substrate during drop impact and its superposition. The theoretical predictions for the temperature evolution in the substrate agree well with the experimental data obtained for different low drop train frequencies. Some deviation at the initial stage of the drop train impact is caused by the natural and forced air convection associated with the gas flow induced by impacting drops. The findings help apply single drop models to sparse sprays.

In Tenzer (2020), liquid patches are observed during spray cooling when the surface temperature is close to the thermosuperrepellency temperature. In the present study, a theoretical approach is developed to explain the formation of liquid patches by the interaction of multiple impacting drops at the substrate. The theory is developed based on the findings of the drop interactions, which describe the spatial and temporal propagation of the temperature inside the substrate caused by an impacting drop. The cooling leads to local changes in boundary conditions for subsequent drops, enabling drop depositions and, thus, the formation of liquid patches.

The single drop impact findings are transferred to spray cooling with the aim of modeling the threshold points and heat flux of the regimes related to transitional boiling. In the present study, it is demonstrated that the temperature of minimum heat flux temperature scales well with the thermosuperrepellency temperature. This indicates that drops above the minimum heat flux temperature rebound in the wet rebound regime. The impacting drops initially wet the substrate and rebound due to percolating vapor bubbles but not necessarily due to a fully developed vapor layer between the drops and substrate, as often assumed in the literature. The model is validated with experimental data from Tenzer (2020) and data from the literature.

Finally, a theoretical model of the heat flux in the transitional boiling regime during spray cooling is developed, using the results from the single impact study as shown in the illustration in Fig. 5.7. The model is valid for temperatures below the thermosuperrepellency temperature and is based on the findings of the theoretical percolation time in the drop dancing regime. The heat flux is modeled by the superposition of single drop impacts in the drop dancing regime and their heat removed before the percolation time. The simplified theoretical model for the heat flux in the transitional boiling regime of sprays agrees very well with the experimental data for sparse sprays.

The theory overpredicts the heat flux at high wall temperatures close to the thermosuperrepellency temperature and high drop velocities. This can be explained by thermal effects (at high temperatures) and hydrodynamic splash phenomena (at higher impact velocities), reducing the deposited mass flux relative to the impacted mass flux. The predictive model of the heat flux allows to operate and control spray cooling better in the transitional boiling regime since the influencing factors are revealed. The theories complement the findings regarding spray cooling with fluids such as water.

Nevertheless, many questions remain open. The heat flux model in the spray cooling regime needs to be further improved to accurately predict the heat flux at higher impact velocities and close to the thermosuperrepellency temperature. This could be related to the influence of drop impacts in the thermal atomization regime, which is so far not considered. Further studies could focus on improving the heat flux model in the transitional boiling regime against disturbances by polydisperse sprays and consider the influence of liquid patches on the substrate. Also, the influence of air convection, forced by the spray has yet to be clarified. The results of the current drop train experiments are most likely influenced by some air convective cooling accompanying the impacting drops. This may affect the heat flux during spray cooling, especially for dense sprays. Further, the appearance of liquid patches is not fully revealed. A theoretical approach is given but not experimentally validated. This could be the subject of further spray cooling experiments. Such studies may make it possible to transfer the present findings to very dense sprays and further application scenarios. In some technical applications, the cooling liquids are mixed with lubricants or salts (e.g., hot dye forging). A study of the influence of additives is necessary to apply the present theories to mixtures.

Since the minimum heat flux temperature is not the so-called Leidenfrost temperature, further studies are needed to identify the temperature from which impacting drops rebound due to a fully developed vapor layer. The limit between the single drop regime wet drop rebound and dry rebound without secondary droplets may describe this threshold temperature during spray cooling.

Nomenclature

Small Greek Characters

α_i	m^2/s	thermal diffusivity of phase $i \in$ [w, l]
δ_ν	m	viscous boundary layer
$\delta_{\mathrm{t},i}$	m	thermal boundary layer in phase $i \in$ [w, l]
ϵ	–	relative wetted area
ϵ_c	–	critical relative wetted area
η_wet	–	effective wetted substrate ratio
γ	m^2	cumulative wetted area
λ	–	filling factor
λ_c	–	critical filling factor
λ_ray	m	light wavelength
λ_i	$\mathrm{W}/(\mathrm{m\,K})$	thermal conductivity of phase $i \in$ [v, w, l]
ν_0	m/s^2	kinematic viscosity at initial liquid temperature
ν_l	m/s^2	kinematic viscosity
π	–	Archimedes constant
ψ	–	spot wetting ratio (drop train)
ρ_i	kg/m^3	density of phase $i \in$ [v, w, l]
σ_B	$\mathrm{W}/(\mathrm{m}^2\,\mathrm{K}^4)$	Stefan Boltzman constant
σ_l	N/m	surface tension
τ_j	s	instant of j^{th} drop
ξ	–	similarity variable

Capital Greek Characters

χ	–	adjustable coefficient

$\Delta\tau$	s	time period of drop impacts
ΔH_0	J/kg	enthalpy difference
ΔT	°C	temperature increment
ΔT^*	°C	threshold superheat
$\Delta T^*_{\mathrm{iso}}$	°C	threshold temperature increment
ΔT_{L}	°C	Leidenfrost superheat
ΔT_{w}	°C	wall superheat
ΔT_ν	°C	Thermosuperrepellency superheat (ν dominated)
ΔT_σ	°C	Thermosuperrepellency superheat (σ dominated)
ΔT_i	°C	temperature increment
Δx_{min}	m	resolving capacity
Ψ	–	area wetting ratio (spray)

Small Roman Characters

b	–	adjustable coefficient
$c_{\mathrm{p},i}$	J/(kg K)	specific heat capacity of phase $i \in$ [v, w, l]
d_0	m	initial drop diameter
d_{10}	m	mean diameter (spray)
d_{32}	m	Sauter mean diameter (spray)
d_{ap}	m	aperture diameter
d_{max}	m	maximum spreading diameter
e_i	J/(K m^2 $\sqrt{\mathrm{s}}$)	thermal effusivity of phase $i \in$ [v, w, l]
f	m	focal length
h_{lamella}	m	lamella thickness
h_{res}	m	residual lamella thickness
h_{v}	m	vapor layer thickness
k_ϵ	–	adjustable coefficient
k_{tb}	–	adjustable coefficient

k_{w}	$-$	adjustable coefficient
$\dot{m}$	$\mathrm{kg}/(\mathrm{m}^2\,\mathrm{s})$	local mass flux
$\dot{m}_{\mathrm{a}}$	$\mathrm{kg}/(\mathrm{m}^2\,\mathrm{s})$	rejected mass flux
$\dot{m}_{\mathrm{b}}$	$\mathrm{kg}/(\mathrm{m}^2\,\mathrm{s})$	impacting mass flux
$\dot{n}$	$1/(\mathrm{m}^2\,\mathrm{s})$	number flux density
p_d	$-$	probability density function
$\dot{q}$	W/m^2	heat flux
$\dot{q}_{\mathrm{CHF}}$	W/m^2	critical heat flux
r	m	r-coordinate
$\bar{r}$	m	dimensionless radius
r_{max}	m	maximum spreading radius
r_{s}	m	spreading radius
r^*	m	radius below Thermosuperrepellency temperature
t	s	time
t_0	s	instance of drop impact time
$\bar{t}$	s	dimensionless time
t_ϵ	s	typical percolation time
t_{ex}	s	exposure time
t_{max}	s	time at maximum spreading
t_{nb}	s	evaporation time (nucleate boiling regime)
t_ν	s	typical time of viscous boundary layer
t_{r}	s	residence time
$\bar{t}_{\mathrm{r}}$	$-$	dimensionless residence time
t_{res}	s	temporal resolution
t_σ	s	typical capillary oscillation time
t^*	s	time below Thermosuperrepellency temperature
t_θ	s	residence time (thermal atomization regime)

t_{th}	s	thermal time scale
u_0	m/s	initial drop impact velocity
u_{10}	m/s	mean drop velocity (spray)
x_{px}	m	pixel size
x_{res}	m	spatial resolution
z	m	z-coordinate

Capital Roman Characters

$\mathrm{A_N}$	–	working aperture
$A_{T^*,\mathrm{tot}}$	$\mathrm{m^2\,s}$	area time below Thermosuperrepellency temperature
A_{T^*}	$\mathrm{m^2}$	area below Thermosuperrepellency temperature
B	–	dimensionless coefficient
G	–	dimensionless coefficient
$\mathscr{J}(\mathrm{Pr}_l)$	–	dimensionless function
K	–	K-number
K_{fb}	–	dimensionless coefficient
L	J/kg	latent heat of evaporation
L^*	J/kg	latent and sensible heat
M	$\mathrm{W/m^2}$	excitance
N	–	number of drops
$\dot{N}$	1/s	number flux
Pe	–	Peclet number
Pr_l	–	Prandtl number
P	–	capillary dominated impact threshold
Q	J	single drop heat removal
Q_{dd}	J	single drop heat removal (drop dancing regime)
Q_{fb}	J	single drop heat removal (film boiling regime)
$\bar{R}_{\mathrm{wet}}$	–	dimensionless wetting radius

Re	–	Reynolds number
$\mathrm{Re}_{\mathrm{s},10}$	–	spray Reynolds number (mean diameter)
$\mathrm{Re}_{\mathrm{s},32}$	–	spray Reynolds number (Sauter mean diameter)
S	$1/\sqrt{\mathrm{s}}$	parameter
S_a	m	surface roughness
T_CHF	°C	critical heat flux temperature
$T_{\mathrm{d},0}$	°C	initial drop temperature
T_hn	°C	homogeneous nucleation temperature
T_L	°C	Leidenfrost temperature
T_ν	°C	Thermosuperrepellency temperature (ν dominated)
$T_{\dot{q},\mathrm{min}}$	°C	minimum heat flux temperature
T_sat	°C	saturation temperature
T_σ	°C	Thermosuperrepellency temperature (σ dominated)
T_spin	°C	spinodal temperature
T^*	°C	threshold temperature
T_w	°C	wall temperature
$T_{\mathrm{w},0}$	°C	initial wall temperature
$\dot{V}$	m^3/s	volume flux
We	–	Weber number
$\mathrm{We}_{\mathrm{s},10}$	–	spray Weber number (mean diameter)
$\mathrm{We}_{\mathrm{s},32}$	–	spray Weber number (Sauter mean diameter)

Shortcuts

conv	convection
DOF	depth of field
exp	experimental
IR	infrared radiation
l	liquid phase

rec	receding
spr	spreading
TIR	total internal reflection
v	vapor phase
w	solid phase

Bibliography

Abu-Zaid, M. (2004). An experimental study of the evaporation characteristics of emulsified liquid droplets. *Heat and Mass Transfer*, 40(9):737–741.

Al-Ahmadi, H. M. & Yao, S. C. (2008). Spray cooling of high temperature metals using high mass flux industrial nozzles. *Experimental Heat Transfer*, 21(1):38–54.

Apostol, M., Skubisz, P., & Adrian, H. (2022). Determination of heat transfer coefficient for air-atomized water spray cooling and its application in modeling of thermomechanical controlled processing of die forgings. *Materials*, 15(7).

Aursand, E., Davis, S. H., & Ytrehus, T. (2018). Thermocapillary instability as a mechanism for film boiling collapse. *Journal of Fluid Mechanics*, 852:283–312.

Baehr, H. D. & Stephan, K. (2013). *Wärme- und Stoffübertragung*. Springer-Verlag, Berlin Heidelberg, 8th edition.

Batzdorf, S., Breitenbach, J., Schlawitschek, C., Roisman, I. V., Tropea, C., Stephan, P., & Gambaryan-Roisman, T. (2017). Heat transfer during simultaneous impact of two drops onto a hot solid substrate. *International Journal of Heat and Mass Transfer*, 113:898–907.

Behrens, B.-A., Lueken, I., & Odening, D. (2010). Cooling and lubrication of automated forging processes with high-pressure systems. *International Journal of Material Forming*, 3(1):331–334.

Benther, J. D., Pelaez-Restrepo, J. D., Stanley, C., & Rosengarten, G. (2021). Heat transfer during multiple droplet impingement and spray cooling: Review and prospects for enhanced surfaces. *International Journal of Heat and Mass Transfer*, 178:121587.

Bernardin, J. D., Stebbins, C. J., & Mudawar, I. (1997). Mapping of impact and heat transfer regimes of water drops impinging on a polished surface. *International Journal of Heat and Mass Transfer*, 40(2):247–267.

Bertola, V. (2015). An impact regime map for water drops impacting on heated surfaces. *International Journal of Heat and Mass Transfer*, 85:430–437.

Biance, A.-L., Chevy, F., Clanet, C., Lagubeau, G., & Quéré, D. (2006). On the elasticity of an inertial liquid shock. *Journal of Fluid Mechanics*, 554:47–66.

Blander, M. & Katz, J. L. (1975). Bubble nucleation in liquids. *AIChE Journal*, 21(5):833–848.

Bolle, L. & Moureau, J. C. (1982). Spray cooling of hot surfaces. *Multiphase Science and Technology*, 1(1-4):1–97.

Breitenbach, J. (2018). *Drop and spray impact onto a hot substrate: Dynamics and heat transfer*. PhD thesis, Technische Universität Darmstadt, Institut für Strömungslehre und Aerodynamik, Darmstadt.

Breitenbach, J., Kissing, J., Roisman, I. V., & Tropea, C. (2018a). Characterization of secondary droplets during thermal atomization regime. *Experimental Thermal and Fluid Science*, 98:516–522.

Breitenbach, J., Roisman, I. V., & Tropea, C. (2017a). Drop collision with a hot, dry solid substrate: Heat transfer during nucleate boiling. *Physical Review Fluids*, 2(7).

Breitenbach, J., Roisman, I. V., & Tropea, C. (2017b). Heat transfer in the film boiling regime: Single drop impact and spray cooling. *International Journal of Heat and Mass Transfer*, 110:34–42.

Breitenbach, J., Roisman, I. V., & Tropea, C. (2018b). From drop impact physics to spray cooling models: a critical review. *Experiments in Fluids*, 59(3):418.

Buchmüller, I. (2014). *Influence of pressure on Leidenfrost effect*. Dissertation, Technische Universität Darmstadt, Institut für Strömungslehre und Aerodynamik, Darmstadt.

Cai, C., Mudawar, I., Liu, H., & Si, C. (2020). Theoretical leidenfrost point (lfp) model for sessile droplet. *International Journal of Heat and Mass Transfer*, 146:118802.

Carey, V. P. (1992). *Liquid-Vapor Phase-Change Phenomena: An Introduction to the Thermophysics of Vaporization and Condensation Processes in Heat Transfer Equipment*. Series in Chemical and Mechanical Engineering. Taylor & Francis, Bristol.

Castanet, G., Caballina, O., Chaze, W., Collignon, R., & Lemoine, F. (2020). The leidenfrost transition of water droplets impinging onto a superheated surface. *International Journal of Heat and Mass Transfer*, 160:120126.

Castanet, G., Caballina, O., & Lemoine, F. (2015). Drop spreading at the impact in the leidenfrost boiling. *Physics of Fluids*, 27(6):063302.

Cebo-Rudnicka, A., Malinowski, Z., & Buczek, A. (2016). The influence of selected parameters of spray cooling and thermal conductivity on heat transfer coefficient. *International Journal of Thermal Sciences*, 110:52–64.

Chandra, S. & Avedisian, C. T. (1991). On the collision of a droplet with a solid surface. *Proceedings of the Royal Society of London. Series A: Mathematical and Physical Sciences*, 432(1884):13–41.

Chaze, W., Caballina, O., Castanet, G., & Lemoine, F. (2017). Spatially and temporally resolved measurements of the temperature inside droplets impinging on a hot solid surface. *Experiments in Fluids*, 58(8):2579.

Chen, R.-H., Chiu, S.-L., & Lin, T.-H. (2007). On the collision behaviors of a diesel drop impinging on a hot surface. *Experimental Thermal and Fluid Science*, 32(2):587–595.

Chen, R.-H., Chow, L. C., & Navedo, J. E. (2002). Effects of spray characteristics on critical heat flux in subcooled water spray cooling. *International Journal of Heat and Mass Transfer*, 45(19):4033–4043.

Cheng, W.-L., Liu, Q.-N., Zhao, R., & Fan, H.-L. (2010). Experimental investigation of parameters effect on heat transfer of spray cooling. *Heat and Mass Transfer*, 46(8):911–921.

Cheng, W.-L., Zhang, W.-W., Chen, H., & Hu, L. (2016). Spray cooling and flash evaporation cooling: The current development and application. *Renewable and Sustainable Energy Reviews*, 55:614–628.

Cheng, X., Sun, T.-P., & Gordillo, L. (2022). Drop impact dynamics: Impact force and stress distributions. *Annual Review of Fluid Mechanics*, 54(1):57–81.

Choi, K. J. & Yao, S. C. (1987). Mechanisms of film boiling heat transfer of normally impacting spray. *International Journal of Heat and Mass Transfer*, 30(2):311–318.

Ciofalo, M., Caronia, A., Di Liberto, M., & Puleo, S. (2007). The nukiyama curve in water spray cooling: Its derivation from temperature-time histories and its dependence on the quantities that characterize drop impact. *International Journal of Heat and Mass Transfer*, 50(25):4948–4966.

Clanet, C., Béguin, C., Richard, D., & Quéré, D. (2004). Maximal deformation of an impacting drop. *Journal of Fluid Mechanics*, 517:199–208.

Cossali, G. E., Coghe, A., & Marengo, M. (1997). The impact of a single drop on a wetted solid surface. *Experiments in Fluids*, 22(6):463–472.

Cossali, G. E., Marengo, M., & Santini, M. (2005). Secondary atomisation produced by single drop vertical impacts onto heated surfaces. *Experimental Thermal and Fluid Science*, 29(8):937–946.

Cossali, G. E., Marengo, M., & Santini, M. (2008). Thermally induced secondary drop atomisation by single drop impact onto heated surfaces. *International Journal of Heat and Fluid Flow*, 29(1):167–177.

Cox, T. L. & Yao, S. C. (1999). Heat transfer of sprays of large water drops impacting on high temperature surfaces. *Journal of Heat Transfer*, 121(2):446–450.

Deiters, T. A. & Mudawar, I. (1989). Optimization of spray quenching for aluminum extrusion, forging, or continuous casting. *Journal of Heat Treating*, 7(1):9–18.

Dobrovinskaya, E. R., Lytvynov, L. A., & Pishchik, V. (2009). *Sapphire: Material, Manufacturing, Applications*. Springer US, Boston, MA, 1st edition.

Dou, R., Wen, Z., & Zhou, G. (2015). Heat transfer characteristics of water spray impinging on high temperature stainless steel plate with finite thickness. *International Journal of Heat and Mass Transfer*, 90:376–387.

Estes, K. A. & Mudawar, I. (1995). Correlation of sauter mean diameter and critical heat flux for spray cooling of small surfaces. *International Journal of Heat and Mass Transfer*, 38(16):2985–2996.

Feller, W. (1971). *An Introduction to Probability Theory and its Applications*, volume 2. John Wiley & Sons, New York, 2nd edition.

Fischer, S. (2015). *Experimental Investigation of Heat Transfer during Evaporation in the Vicinity of Moving Three-Phase Contact Lines*. PhD thesis, Technische Universität, Institut für Technische Thermodynamik, Darmstadt.

Fischer, S., Gambaryan-Roisman, T., & Stephan, P. (2015). On the development of a thin evaporating liquid film at a receding liquid/vapour-interface. *International Journal of Heat and Mass Transfer*, 88:346–356.

Fujimoto, H., Oku, Y., Ogihara, T., & Takuda, H. (2010). Hydrodynamics and boiling phenomena of water droplets impinging on hot solid. *International Journal of Multiphase Flow*, 36(8):620–642.

Gajevic Joksimovic, M., Schmidt, J. B., Roisman, I. V., Tropea, C., & Hussong, J. (2023). Impact of a suspension drop onto a hot substrate: diminution of splash and prevention of film boiling. *Soft Matter*, 19:1440–1453.

Gholijani, A., Gambaryan-Roisman, T., & Stephan, P. (2022). Experimental investigation of hydrodynamics and heat transport during horizontal coalescence of two drops impinging a hot wall. *Experimental Thermal and Fluid Science*, 131:110520.

Gottfried, B. S., Lee, C. J., & Bell, K. J. (1966). The leidenfrost phenomenon: film boiling of liquid droplets on a flat plate. *International Journal of Heat and Mass Transfer*, 9(11):1167–1188.

Grant, G., Brenton, J., & Drysdale, D. (2000). Fire suppression by water sprays. *Progress in Energy and Combustion Science*, 26(2):79–130.

Grissom, W. M. & Wierum, F. A. (1981). Liquid spray cooling of a heated surface. *International Journal of Heat and Mass Transfer*, 24(2):261–271.

Hofmann, J. (2019). *Experimental investigation of the Leidenfrost point during spray- and single drop impact.* Master thesis, Technische Universität Darmstadt.

Hoogendoorn, C. J. & den Hond, R. (1974). Leidenfrost temperature and heat-transfer coefficients for water sprays impinging on a hot surface. In *International Heat Transfer Conference 5*, pages 135–138.

Horacek, B., Kiger, K. T., & Kim, J. (2005). Single nozzle spray cooling heat transfer mechanisms. *International Journal of Heat and Mass Transfer*, 48(8):1425–1438.

Hsieh, C.-C. & Yao, S.-C. (2006). Evaporative heat transfer characteristics of a water spray on micro-structured silicon surfaces. *International Journal of Heat and Mass Transfer*, 49(5):962–974.

Itaru, M. & Kunihide, M. (1978). Heat transfer characteristics of evaporation of a liquid droplet on heated surfaces. *International Journal of Heat and Mass Transfer*, 21(5):605–613.

Ito, T., Takata, Y., Mousa, M. M. M., & Yoshikai, H. (1991). Studies on the water cooling of hot surfaces (experiment of spray cooling). *Memoirs of the Faculty of Engineering, Kyushu University*, 51(2):119–144.

Ji, R.-J., Zhu, D.-Q., Lin, X.-W., Zhou, Z.-F., & Chen, B. (2023). Parametric investigation on the close-loop r410a flash spray system for high power electronics cooling under low temperature. *Case Studies in Thermal Engineering*, 41.

Josserand, C. & Thoroddsen, S. T. (2016). Drop impact on a solid surface. *Annual Review of Fluid Mechanics*, 48(1):365–391.

Kakac, S. & Bon, B. (2008). A Review of two-phase flow dynamic instabilities in tube boiling systems. *International Journal of Heat and Mass Transfer*, 51:399–433.

Kao, B., Kelly, K. M., Aguilar, G., Hosaka, Y., Barr, R. J., & Nelson, J. S. (2004). Evaluation of cryogen spray cooling exposure on in vitro model human skin. *Lasers in Surgery and Medicine*, 34(2):146–154.

Karwa, N., Kale, S. R., & Subbarao, P. M. V. (2007). Experimental study of non-boiling heat transfer from a horizontal surface by water sprays. *Experimental Thermal and Fluid Science*, 32(2):571–579.

Kim, J. (2007). Spray cooling heat transfer: The state of the art. *International Journal of Heat and Fluid Flow*, 28(4):753–767.

Labergue, A., Pena-Carillo, J.-D., Gradeck, M., & Lemoine, F. (2017). Combined three-color lif-pda measurements and infrared thermography applied to the study of the spray impingement on a heated surface above the leidenfrost regime. *International Journal of Heat and Mass Transfer*, 104:1008–1021.

Laseinde, O. T. & Ramere, M. D. (2021). Efficiency improvement in polycrystalline solar panel using thermal control water spraying cooling. *Procedia Computer Science*, 180:239–248.

Lee, S.-H., Rump, M., Harth, K., Kim, M., Lohse, D., Fezzaa, K., & Je, J. H. (2020). Downward jetting of a dynamic leidenfrost drop. *Physical Review Fluids*, 5(7).

Leidenfrost, J. G. (1756). *De aquae communis nonnullis qualitatibus tractatus*. Ovenius.

Leidenfrost, J. G. (1966). On the fixation of water in diverse fire. *International Journal of Heat and Mass Transfer*, 9(11):1153–1166.

Liang, G. & Mudawar, I. (2017a). Review of spray cooling - part 1: Single-phase and nucleate boiling regimes, and critical heat flux. *International Journal of Heat and Mass Transfer*, 115:1174–1205.

Liang, G. & Mudawar, I. (2017b). Review of spray cooling - part 2: High temperature boiling regimes and quenching applications. *International Journal of Heat and Mass Transfer*, 115:1206–1222.

Lloyd, S. (1982). Least squares quantization in pcm. *IEEE Transactions on Information Theory*, 28(2):129–137.

Manzello, S. L. & Yang, J. C. (2002). On the collision dynamics of a water droplet containing an additive on a heated solid surface. *Proceedings of the Royal Society of London. Series A: Mathematical, Physical and Engineering Sciences*, 458(2026):2417–2444.

Marengo, M., Antonini, C., Roisman, I. V., & Tropea, C. (2011). Drop collisions with simple and complex surfaces. *Current Opinion in Colloid & Interface Science*, 16(4):292–302.

Martínez-Galván, E., Antón, R., Ramos, J. C., & Khodabandeh, R. (2013). Influence of surface roughness on a spray cooling system with r134a. part I: Heat transfer measurements. *Experimental Thermal and Fluid Science*, 46:183–190.

Mertens, S. & Moore, C. (2012). Continuum percolation thresholds in two dimensions. *Physical Review E*, 86(6):061109.

Moreira, A. L. N., Moita, A. S., & Panão, M. R. (2010). Advances and challenges in explaining fuel spray impingement: How much of single droplet impact research is useful? *Progress in Energy and Combustion Science*, 36(5):554–580.

Mudawar, I. (2013). Recent advances in high-flux, two-phase thermal management. *Journal of Thermal Science and Engineering Applications*, 5(2):021012.

Mudawar, I. & Valentine, W. S. (1989). Determination of the local quench curve for spray-cooled metallic surfaces. *Journal of Heat Treating*, 7(2):107–121.

Mundo, C. H. R., Sommerfeld, M., & Tropea, C. (1998). On the modeling of liquid sprays impinging on surfaces. *Atomization and Sprays*, 8(6).

Mundo, C. H. R., Tropea, C., & Sommerfeld, M. (1997). Numerical and experimental investigation of spray characteristics in the vicinity of a rigid wall. *Experimental Thermal and Fluid Science*, 15(3):228–237.

Myers, G. E. (1987). *Analytical methods in conduction heat transfer*. Genium Publishing Corporation, Schenectady, New York.

Nelson, J. S., Majaron, B., & Kelly, K. M. (2000). Active skin cooling in conjunction with laser dermatologic surgery. *Seminars in Cutaneous Medicine and Surgery*, 19(4):253–266.

Nukiyama, S. (1966). The maximum and minimum values of the heat q transmitted from metal to boiling water under atmospheric pressure. *International Journal of Heat and Mass Transfer*, 9(12):1419–1433.

Otsu, N. (1979). A Threshold Selection Method from Gray-Level Histograms. *IEEE Transactions on Systems, Man, and Cybernetics*, 9(1):62–66.

Pasandideh-Fard, M., Aziz, S. D., Chandra, S., & Mostaghimi, J. (2001). Cooling effectiveness of a water drop impinging on a hot surface. *International Journal of Heat and Fluid Flow*, 22(2):201–210.

Pedrotti, F. L., Pedrotti, L. S., Bausch, W., & Schmidt, H. (2005). *Optik für Ingenieure: Grundlagen*. Springer, Berlin and Heidelberg and New York, 3rd edition.

Pola, A., Gelfi, M., & La Vecchia, G. M. (2013). Simulation and validation of spray quenching applied to heavy forgings. *Journal of Materials Processing Technology*, 213(12):2247–2253.

Quell, J. K. O. (2020). *Experimental study of the Leidenfrost Temperature during the droplet chain. impact onto a heated surface*. Master thesis, Technische Universität Darmstadt.

Quéré, D. (2005). Non-sticking drops. *Reports on Progress in Physics*, 68(11):2495–2532.

Quéré, D. (2013). Leidenfrost Dynamics. *Annual Review of Fluid Mechanics*, 45(1):197–215.

Ravikumar, K. P., Mohapatra, S. S., Sahoo, A., & Mohapatra, S. S. (2023). High mass flux spray evaporative quenching on hot moving plate: A novel methodology for achieving high heat flux and continuous production criteria. *Thermal Science and Engineering Progress*, 42:101880.

Rayleigh, L. (1879). Vi. on the capillary phenomena of jets. *Proceedings of the Royal Society of London*, 29(196-199):71–97.

Rein, M. (2002). *Drop-Surface Interactions*, volume 456 of *CISM Courses and Lectures*. Springer-Verlag Wien.

Richard, D., Clanet, C., & Quéré, D. (2002). Contact time of a bouncing drop. *Nature*, 417(6891):811.

Rioboo, R., Tropea, C., & Marengo, M. (2001). Outcomes from a drop impact on solid surfaces. *Atomization and Sprays*, 11(2):12.

Rodman, D., Krause, C., Nürnberger, F., Bach, F.-W., Haskamp, K., Kästner, M., & Reithmeier, E. (2011). Induction hardening of spur gearwheels made from 42crmo4 hardening and tempering steel by employing spray cooling. *steel research international*, 82(4):329–336.

Roisman, I. V. (2009). Inertia dominated drop collisions. ii. an analytical solution of the navier–stokes equations for a spreading viscous film. *Physics of Fluids*, 21(5):052104.

Roisman, I. V. (2010). Fast forced liquid film spreading on a substrate: flow, heat transfer and phase transition. *Journal of Fluid Mechanics*, 656:189–204.

Roisman, I. V., Berberović, E., & Tropea, C. (2009). Inertia dominated drop collisions. i. on the universal flow in the lamella. *Physics of Fluids*, 21(5):052103.

Roisman, I. V., Breitenbach, J., & Tropea, C. (2018). Thermal atomisation of a liquid drop after impact onto a hot substrate. *Journal of Fluid Mechanics*, 842:87–101.

Roisman, I. V., Lembach, A., & Tropea, C. (2015). Drop splashing induced by target roughness and porosity: The size plays no role. *Advances in Colloid and Interface Science*, 222:615–621.

Roisman, I. V., Rioboo, R., & Tropea, C. (2002). Normal impact of a liquid drop on a dry surface: model for spreading and receding. *Proceedings of the Royal Society of London. Series A: Mathematical, Physical and Engineering Sciences*, 458(2022):1411–1430.

Salman, A. S., Abdulrazzaq, N. M., Oudah, S. K., Tikadar, A., Anumbe, N., Paul, T. C., & Khan, J. A. (2019). Experimental investigation of the impact of geometrical surface modification on spray cooling heat transfer performance in the non-boiling regime. *International Journal of Heat and Mass Transfer*, 133:330–340.

Schiro, F., Benato, A., Stoppato, A., & Destro, N. (2017). Improving photovoltaics efficiency by water cooling: Modelling and experimental approach. *Energy*, 137:798–810.

Schmidt, J. B., Breitenbach, J., Roisman, I. V., & Tropea, C. (2018). Heat flux during a drop impact onto a hot, dry solid surface. In *14th Triennial International Conference on Liquid Atomization and Spray Systems, Chicago, IL, USA*.

Schmidt, J. B., Breitenbach, J., Roisman, I. V., & Tropea, C. (2019). Measurement of the heat flux during a drop impact onto a hot dry solid surface using infrared thermal imaging. In *Notes on Numerical Fluid Mechanics and Multidisciplinary Design*, pages 553–562. Springer International Publishing.

Schmidt, J. B., Breitenbach, J., Roisman, I. V., & Tropea, C. (2022). Interaction of drops and sprays with a heated wall. In Schulte, K., Tropea, C., & Weigand, B., editors, *Droplet Dynamics Under Extreme Ambient Conditions*, pages 333–353. Springer International Publishing, Cham.

Schmidt, J. B., Breitenbach, J., Roisman, I. V., Tropea, C., & Hussong, J. (2021a). Transition from drop deposition to drop rebound during drop chain impact onto a hot target. In *15th Triennial International Conference on Liquid Atomization and Spray Systems, Edinburgh, SC, UK*.

Schmidt, J. B., Hofmann, J., Tenzer, F. M., Breitenbach, J., Tropea, C., & Roisman, I. V. (2021b). Thermosuperrepellency of a hot substrate caused by vapour percolation. *Communications Physics*, 4(1).

Schmidt, J. B., Roisman, I. V., Tropea, C., & Hussong, J. (2023a). Heat flux during a drop train impact in the drop rebound regime. *Experimental Thermal and Fluid Science*, 145:110897.

Schmidt, J. B., Tenzer, F., Tropea, C., Hussong, J., & Roisman, I. V. (2023b). Modelling of drop and spray impact in the transitional boiling regime. *International Journal of Heat and Mass Transfer*, 217:124586.

Sehmbey, M. S., Chow, L. C., Hahn, O. J., & Pais, M. R. (1995). Spray cooling of power electronics at cryogenic temperatures. *Journal of Thermophysics and Heat Transfer*, 9(1):123–128.

Senda, J., Yamada, K., Fujimoto, H., & Miki, H. (1988). The heat-transfer characteristics of a small droplet impinging upon a hot surface. *JSME international journal. Ser. 2, Fluids engineering, heat transfer, power, combustion, thermophysical properties*, 31(1):105–111.

Shirota, M., van Limbeek, M. A. J., Sun, C., Prosperetti, A., & Lohse, D. (2016). Dynamic leidenfrost effect: Relevant time and length scales. *Physical Review Letters*, 116(6):064501.

Shoji, M., Wakunaga, T., & Kodama, K. (1984). Heat transfer from a heated surface to impinging subcooled droplets: Heat transfer characteristics in non-wetting region. *Transactions of the Japan Society of Mechanical Engineers Series B - Japanese Research*, 50(451):716–723.

Sienski, K., Eden, R., & Schaefer, D. (1996). 3-d electronic interconnect packaging. In *1996 IEEE Aerospace Applications Conference. Proceedings*, volume 1, pages 363–373.

Silk, E. A., Golliher, E. L., & Selvam, R. P. (2008). Spray cooling heat transfer: Technology overview and assessment of future challenges for micro-gravity application. *Energy Conversion and Management*, 49(3):453–468.

Sodtke, C. & Stephan, P. (2007). Spray cooling on micro structured surfaces. *International Journal of Heat and Mass Transfer*, 50(19):4089–4097.

Sozbir, N., Chang, Y. W., & Yao, S. C. (2003). Heat Transfer of Impacting Water Mist on High Temperature Metal Surfaces. *Journal of Heat Transfer*, 125(1):70–74.

Spiegler, P., Hopenfeld, J., Silberberg, M., Bumpus, C. F., & Norman, A. (1963). Onset of stable film boiling and the foam limit. *International Journal of Heat and Mass Transfer*, 6(11):987–989.

Staszel, C. & Yarin, A. L. (2018). Exponential vaporization fronts and critical heat flux in pool boiling. *The International Communications in Heat and Mass Transfer*, 98:171–176.

Stow, C. D. & Hadfield, M. G. (1981). An experimental investigation of fluid flow resulting from the impact of a water drop with an unyielding dry surface. *Proceedings of the Royal Society of London. Series A, Mathematical and Physical Sciences*, 373(1755):419–441.

Tartarini, P., Lorenzini, G., & Randi, M. R. (1999). Experimental study of water droplet boiling on hot, non-porous surfaces. *Heat and Mass Transfer*, 34(6):437–447.

Taylor, G. I. (1959). The dynamics of thin sheets of fluid. iii. disintegration of fluid sheets. *Proceedings of the Royal Society of London. Series A. Mathematical and Physical Sciences*, 253(1274):313–321.

Tenzer, F. M. (2020). *Heat transfer during transient spray cooling: An experimental and analytical study.* PhD thesis, Technische Universität Darmstadt, Institut für Strömungslehre und Aerodynamik.

Tenzer, F. M., Roisman, I. V., & Tropea, C. (2019). Fast transient spray cooling of a hot thick target. *Journal of Fluid Mechanics*, 881:84–103.

Thoroddsen, S. T., Etoh, T. G., Takehara, K., Ootsuka, N., & Hatsuki, Y. (2005). The air bubble entrapped under a drop impacting on a solid surface. *Journal of Fluid Mechanics*, 545:203–212.

Tilton, D. E., Ambrose, J. H., & Chow, L. C. (1989). Closed-system, high-flux evaporative spray cooling. *SAE Transactions*, 98:1692–1700.

Tran, T., Staat, H. J. J., Prosperetti, A., Sun, C., & Lohse, D. (2012). Drop impact on superheated surfaces. *Physical Review Letter*, 108(3):036101.

Tran, T., Staat, H. J. J., Susarrey-Arce, A., Foertsch, T. C., van Houselt, A., Gardeniers, H. J. G. E., Prosperetti, A., Lohse, D., & Sun, C. (2013). Droplet impact on superheated micro-structured surfaces. *Soft Matter*, 9(12):3272.

VDI e.V. (2013). *VDI-Wärmeatlas*. Springer Berlin Heidelberg, Berlin, Heidelberg, 11th edition.

Wachters, L. H. J. & Westerling, N. A. J. (1966). The heat transfer from a hot wall to impinging water drops in the spheroidal state. *Chemical Engineering Science*, 21(11):1047–1056.

Wang, J.-X., Guo, W., Xiong, K., & Wang, S.-N. (2020a). Review of aerospace-oriented spray cooling technology. *Progress in Aerospace Sciences*, 116:100635.

Wang, Z., Qu, W., Xiong, J., Zhong, M., & Yang, Y. (2020b). Investigation on effect of surface properties on droplet impact cooling of cladding surfaces. *Nuclear Engineering and Technology*, 52:508–519.

Worthington, A. M. (1877). XXVIII. on the forms assumed by drops of liquids falling vertically on a horizontal plate. *Proceedings of the Royal Society of London*, 25(171-178):261–272.

Worthington, A. M. & Cole, R. S. (1897). V. impact with a liquid surface, studied by the aid of instantaneous photography. *Philosophical Transactions of the Royal Society of London. Series A, Containing Papers of a Mathematical or Physical Character*, 189:137–148.

Yao, S. C. & Choit, K. J. (1987). Heat transfer experiments of mono-dispersed vertically impacting sprays. *International Journal of Multiphase Flow*, 13(5):639–648.

Yao, S. C. & Cox, T. L. (2002). A general heat transfer correlation for impacting water sprays on high-temperature surfaces. *Experimental Heat Transfer*, 15(4):207–219.

Yarin, A. L. (2006). Drop impact dynamics: Splashing, spreading, receding, bouncing. . .. *Annual Review of Fluid Mechanics*, 38(1):159–192.

Yarin, A. L., Roisman, I. V., & Tropea, C. (2017). *Collision Phenomena in Liquids and Solids*. Cambridge University Press, Cambridge.

Yarin, A. L. & Weiss, D. A. (1995). Impact of drops on solid surfaces: self-similar capillary waves, and splashing as a new type of kinematic discontinuity. *Journal of Fluid Mechanics*, 283:141–173.

Yesildal, F., Ozakin, A. N., & Yakut, K. (2022). Optimization of operational parameters for a photovoltaic panel cooled by spray cooling. *Engineering Science and Technology, an International Journal*, 25:100983.

Zuber, N. (1958). On the stability of boiling heat transfer. *Transactions of the American Society of Mechanical Engineers*, 80(Univ. of California, Los Angeles).

List of Figures

List of Tables